ABSTRACT

Title of Document: PRINCIPLES FOR NEW OPTICAL TECHNIQUES IN MEDICAL DIAGNOSTICS FOR mHEALTH APPLICATIONS

Joshua Michael Balsam, Ph.D., 2014

Directed By: Hugh A. Bruck, Professor, Department of Mechanical Engineering

Medical diagnostics is a critical element of effective medical treatment. However, many modern and emerging diagnostic technologies are not affordable or compatible with the needs and conditions found in low-income and middle-income countries and regions. Resource-poor areas require low-cost, robust, easy-to-use, and portable diagnostics devices compatible with telemedicine (i.e. mHealth) that can be adapted to meet diverse medical needs. Many suitable devices will need to be based on optical technologies, which are used for many types of biological analyses. This dissertation describes the fabrication and detection principles for several low-cost optical technologies for mHealth applications including: (1) a webcam based multi-wavelength fluorescence plate reader, (2) a lens-free optical detector used for the detection of Botulinum A neurotoxin activity, (3) a low cost micro-array reader that allows the performance of typical fluorescence based assays demonstrated for the detection of the toxin staphylococcal enterotoxin (SEB), and (4) a wide-field flow cytometer for high throughput detection of fluorescently labeled rare cells. This dissertation discusses how these technologies can be harnessed using readily available consumer electronics components such as webcams, cell phones, CCD cameras, LEDs, and laser diodes. There are challenges in developing devices with sufficient sensitivity and specificity, and approaches are presented to overcoming these challenges to create optical

detectors that can serve as low cost medical diagnostics in resource-poor settings for mHealth.

PRINCIPLES FOR NEW OPTICAL TECHNIQUES IN MEDICAL DIAGNOSTICS FOR mHEALTH APPLICATIONS

By
Joshua Michael Balsam

Dissertation submitted to the Faculty of the Graduate School of the
University of Maryland, College Park, in partial fulfillment
of the requirements for the degree of
Doctor of Philosophy
2014

Advisory Committee:

Professor Hugh A. Bruck, Chair
Professor Don DeVoe
Associate Professor Miao Yu
Associate Professor David Bigio
Professor Benjamin Shapiro, Dean’s Representative

Dedication

To my parents, Fred and Elaine, my brother Christopher and my sister Julia.

Thank you for your love.

Acknowledgements

During the course of my career as a doctoral student I have been contributed to by a great number of people. First among those whom I would like to thank is my advisor Dr. Hugh Bruck. His reliable patience and guidance have made what is often described as an arduous journey really rather enjoyable. In addition, Dr. Avraham Rasooly has been an indispensable source of new ideas and original viewpoints without which this work would not have been possible. I would like to thank my dissertation committee of Drs. Don DeVoe, Miao Yu, David Bigio, and Ben Shapiro for their support over the past year. Of my many colleagues at the FDA, I would like to especially thank Drs. Kim Sapsford-Medintz and Samantha Spindel for patiently explaining the finer points of bio-chemistry to a mechanical engineer, and for their friendship. Finally, I wish to thank Dr. Marilyn Lightfoote and the FDA office of science and engineering laboratories division of biology, as well as Dr. Elizabeth Katz in the office of device evaluation, for their financial support.

Table of Contents

Dedication ii
Acknowledgements iii
Table of Contents iv
Index of Figures v
1. Introduction 1
    1.1 Background and motivation 1
    1.2 Dissertation goals and scope 4
2. Literature review 6
    2.1 Lensless fluorescence detection 6
    2.2 Fluorescence detection for mHealth 11
    2.3 Capillary-based fluorescence detection 12
    2.4 Fluorescence based flow cytometry for rare cell detection 17
3. Compact lens-free optical collimation 21
    3.1 Device development 21
        3.1.1 Materials and methods 22
        3.1.2 Results and discussion 26
    3.2 Collimator design principles and modeling 38
4. Image stacking approach to increase sensitivity of fluorescence detection 47
    4.1 Materials and methods 47
    4.2 Results and discussion 50
5. Capillary array waveguide amplified fluorescence detector 58
    5.1 Materials and methods 58
    5.2 Results and discussion 61
    5.3 Orthographic projection capillary array fluorescence sensor 71
6. Micro-array reading with non-uniform excitation 79
    6.1 Materials and methods 80
    6.2 Results and discussion 89
7. High throughput flow cytometry for rare cell detection 92
    7.1 Conventional imaging-mode rare cell detection 94
        7.1.1 Materials and methods 94
        7.1.2 Results and discussion 98
    7.2 Streak-mode imaging rare cell detection 113
        7.2.1 Materials and methods 113
        7.2.2 Results and discussion 116
8. Scientific and technical contributions 150
9. References 153

Index of Figures

Figure 1 - Schematic of lensfree fluorescence microscopy based on optical holography...9
Figure 2 - Capillary optical configurations........15
Figure 3 - Basic elements and configuration of lensless detector........27
Figure 4 - Light characteristics of lensless detector illumination........31
Figure 5 - Functional elements of the microfluidic system........33
Figure 6 - Lensless CCD-based fluorometry results........34
Figure 7 - Lensless in vitro activity detection of BoNT-A light chain (LcA) using the SNAP-25 cleavage assay........37
Figure 8 - Comparison of ideal and actual collimators........39
Figure 9 - Schematic of optical Söller collimator array........41
Figure 10 - Model Validation for simplified collimator test case........44
Figure 11 - Agreement between modeled and measured data........45
Figure 12 - Fluorescent LOD prior to image stacking........51
Figure 13 - Image stacking of webcam video captured images........52
Figure 14 - Probability of photon arrivals........54
Figure 15 - Relationship between sensor noise cutoff, pixel SNR and number of averaged video frames........57
Figure 16 - mHealth capillary array fluorescence detectors........59
Figure 17 - Capillary array fluorescence amplification........62
Figure 18 - CCD camera detection of waveguide capillary array fluorescence........64
Figure 19 - Waveguide fluorescence capillary array amplification........66
Figure 20 - Waveguide capillary array fluorescence amplification combined with computational image stacking........69
Figure 21 - Waveguide capillary array fluorescence amplification images captured with mobile phone........70
Figure 22 – Orthographic projection optics........73
Figure 23 - Orthograpic projection optics........74
Figure 24 - Light distribution with orthographic projection optics........76
Figure 25 – Adenovirus detection by gel electrophoresis and fluorimetry........78
Figure 26 - Schematic of cross flow microfluidics........81
Figure 27 - Microarray reader schematic........82
Figure 28 – Slide background fluorescence profile........83
Figure 29 – SEB protein assay result........84
Figure 30 - Evanescent field amplification factor and operating location........86
Figure 31 - Extended linear response range........87
Figure 32 - Raw slide data........88
Figure 33 - Background subtracted slide data........88
Figure 34 – Detection of SEB *via* fluorescent sandwich assay........89
Figure 35 - Comparison of micro-array reader and plate reader performance........90
Figure 36 - Dye diffusion modeling........99
Figure 37 - Hydrodynamic focusing flow cell design........101
Figure 38 - Schematic of webcam-based wide-field flow cytometer........104
Figure 39 - Emission spectrum of Syto-9 dye compared to sensitivity of CMOS sensor........106

Figure 40 - A comparison between webcam-based wide-field flow cytometer and webcam-based flow focusing cytometry 107
Figure 41 - Analysis of a single cell using webcam-based wide-field flow cytometry ... 109
Figure 42 - Webcam-based wide-field flow cytometer counting efficiency 110
Figure 43 – Approximate stage of dye diffusion during cell counting 112
Figure 44 - Optimized wide field flow cell 114
Figure 45 - Relationship between exposure time and maximum pixel brightness 118
Figure 46 - Streak-mode imaging principles 121
Figure 47 – Relationship between streak averaging length and noise standard deviation 123
Figure 48 - Effect of averaging on peak pixel value 124
Figure 49 – Effect of averaging length on SNR 124
Figure 50 - 3D visualization of raw pixel data from a cell streak 126
Figure 51 - 3D visualization of increasing SNR with increasing streak averaging length 127
Figure 52 - Streak imaging background subtraction 128
Figure 53 - Flowcell autofluorescence drift 129
Figure 54 - Autofluorescent drift compensation 130
Figure 55 – Cell velocity measurement 132
Figure 56 - Cell Streak Brightness Modeling 133
Figure 57 - Relationship between streak brightness and exposure time 134
Figure 58 - Relationship between spatial pixel standard deviation and exposure time ... 135
Figure 59 - Effect of flow cell autofluorescent intensity on streak SNR 136
Figure 60 - Cell streak SNR modeling 137
Figure 61 - Visualizing cell populations using pixel values 140
Figure 62 – Visualizing cell populations with photon emission rate 141
Figure 63 – Measured photon transfer functions for Point Grey Research CMLN 13S2M-CS CCD camera 144
Figure 64 - Published quantum efficiency curve for PGR CMLN camera 145
Figure 65 - Webcam-based wide-field flow cytometer counting efficiency 147
Figure 66 - Rare Cell Detection Modeling 148

1. Introduction

1.1 Background and motivation

Many medical diagnostic technologies have been developed for high-income countries and are not affordable or compatible with the needs and conditions in low-income and middle-income countries. The challenges and the need to develop simple, low-cost, mobile medical diagnostics for resource-poor settings with minimal medical infrastructure are well recognized under the emerging area of mobile health (mHealth)[1-3]. Overcoming these challenges by developing new principles for diagnostic techniques utilizing appropriate low-cost components, reagents and manufacturing processes will have clear benefits for the detection and analysis of many diseases in low-resource settings.

The main elements of a biodetection platform for global health include appropriate biomarkers and appropriate technologies for performing diagnostic assays with limited access to laboratory facilities. Such technologies must be: (a) simple to operate and maintain by minimally trained local staff, (b) suitable for manufacturing at low cost with low cost disposables, (c) operable in locations with limited or no medical infrastructure and without network electricity, land line communication, refrigeration or municipal water supply, (d) capable of multiplexing (multiple parallel analytes or samples) when needed, (e) internet capable for remote collaboration, (f) capable of rapid results, (g) modular in design, (h) capable of self-diagnostics and calibration, and (i) portable. A device with these characteristics would be easily adaptable to the various applications and diagnostics needs.

Recent developments in consumer electronics devices, microfabrication technologies, wireless communication, portable computing, microfluidics, and lab-on-a-chip (LOC) technologies have enabled the development of highly sensitive, low cost detection technologies for low-resource settings. In particular, LOC technologies[4] have enabled the performance of various chemical and biological assays outside of laboratory environments. LOC provides a potential approach for developing point of care (POC) analytical tools for resource-poor settings[5, 6].

Another component that is critical to developing low cost technologies for diagnostics in low-resource settings is the detection approach. Optical detection is one of the most common detection approaches used in research, clinical and industrial laboratory analysis, and is based on one of several optical modalities including light absorbance, fluorescence, polarization, colorimetry, spectrometry, or luminescence. Several optical detection methods developed for biodetection employ photodiodes[7-10] and photomultipliers[11-16], which are inherently spot detectors for analysis of limited areas with high sensitivity (e.g., one part of an LOC). Alternatively, charge-coupled device (CCD) or complementary metal oxide semiconductor (CMOS) cameras are suitable for optical detection over large areas, and have already been employed in several array assays[17-20]. The main advantage of such area detectors is that they can be used for analyzing light from a large enough region of interest that it can cover the entire surface of a LOC or array assay[21-23]. This has made area sensor based detectors an ideal choice for LOC multichannel detection, since many sample channels can be analyzed simultaneously.

Several CCD-based detection systems for LOCs have been developed[5, 18, 20, 22, 24-27]. Although such detectors have sensitivity similar to the sensitivity of current laboratory ELISA readers, these systems have utilized sensitive research-grade[17, 18, 20] or cooled CCD cameras[5, 22, 24-27], which significantly increases the cost of such systems and thus limits their use as low cost technologies for low-resource settings associated with global health. To reduce potential costs while not sacrificing the use of such sensitive devices, new principles for imaging have been developed. One such principle, lens-free imaging, has been used to develop several low cost optical detection platforms[28-36]. Cell phones have been adapted for biodetection applications where their integrated imaging capability and communications play a major role in the emerging realm known as mHealth[37-41]. An inherent feature in mHealth technologies is wireless connectivity. This has the potential to enable seamless telemedicine in which collected assay data can be analyzed globally, allowing clinical expertise to be brought to remote areas and to resource-poor environments where such clinical expertise does not exist.

Sustainability is a critical principle which must inform the development of new technologies for resource-poor environments. Sustainable technologies are those which are based on low cost components which are readily available in the regions where they are deployed (e.g. consumer electronic components, plastics, *etc.*). They must be simple to operate and maintain to ensure successful use over time by minimally trained local technicians. This fundamental principle is one which has informed the design and development of higher level principles discussed throughout this document. It will be seen that each newly developed technique, methodology, or principle has arisen to allow a sustainable technology to replace a potentially unsustainable one.

Moving away from conventional detection platforms (*i.e.* purpose-built optical detectors) and adopting low cost off-the-shelf components while not sacrificing assay performance necessitates overcoming several key challenges. Challenges include increased noise, decreased resolution, and decreased dynamic range. Together these factors result in higher (i.e. worse) limits of detection values for biological assays, which translates to a detection platform with reduced utility for early detection of diseases. If this method for improving the quality of health care in underserved regions is to be successful it will be necessary to overcome these challenges. Addressing these challenges is the basis for the development of the principles presented here.

1.2 Dissertation goals and scope

The goal of this research is to develop techniques and principles to guide the application of low cost optical technologies to clinically relevant biodetection problems. In each case the newly established principles have been used to develop proof of concept devices in order to demonstrate their utility. These devices have been benchmarked against current industry standard methods and equipment using clinically relevant assays or simulations of such assays.

Applications which have been investigated include pathogen detection *via* liquid phase fluorescent assays, surface patterned micro-array reading, and high throughput rare cell detection via flow cytometry. The optical transduction mechanism in each case is fluorescence. Several low cost, portable proof-of-concept devices have been developed based on these applications and have been demonstrated to have limits of detection and utility similar to their laboratory equivalents. Initial equipment costs for these demonstrated devices have been estimated to be between 100 and 1,000 times less than their conventional counterparts.

2. Literature review

2.1 Lensless fluorescence detection

Optical detection is probably the most common detection approach used in research, clinical and industrial laboratory analysis. It is based on one of several optical modalities including light absorbance, fluorescence, polarization or luminescence. Lab on a chip (LOC) analysis utilizing optical detectors has been first carried out (albeit off-chip), by microscopes, optoelectronics[42,43] or charge-coupled device (CCD) based systems. In addition, several portable CCD based detection systems for lab on a chip have been developed.[44–51] Such CCD based detectors have sensitivity similar to laboratory ELISA readers[50,52] utilizing sensitive cooled CCD developed for research[44,45,53] or more affordable cooled CCD developed for astronomy.[46-51]

Lensless optical detectors may enable development of low cost and very compact optical devices. Without a lens, the shorter focal distance from the measured area makes the device more compact, and may enable the development of low cost, high resolution imaging devices without the need for conventional optical components. Several lensless contact imaging microscopes have been reported.[54-64] These lensless approaches requires that the microdevices to be imaged and the sensor have similar sizes, with the image resolution governed by the sensor's pixel size, typically 3 μm or larger. Lensless contact imaging can be used to image particles or cells through light absorbance, fluorescence or luminescence.

Lensless contact imaging optofluidic microscopy (OFM)[60-63] consists of an opaque metal film with an etched array of micron or submicron apertures and a PDMS microfluidic chip that is bonded onto the metal film, time-varying the light transmission through each hole to form a transmission image line trace across the object directly on the CCD. OFM enables high resolution images of cells, spores, and nematodes in microchannels using raster scanning combined with computational reconstruction of the images.[60,62]

More recently, several new approaches for lensfree microscopy were described including holographic microscopy which allows for 0.6 μm spatial resolution corresponding to a numerical aperture of 0.5 over a large field-of-view of 24 mm.[43,65] Such a system was used to analyze antibody microarrays for high throughput detection of leukocyte numbers and function.[66] Lensfree holographic microscopy was also used for color and monochrome on-chip imaging of caenorhabditis elegans[67] and for a multi-angle lensfree holographic imaging platform that can accurately characterize both the axial and lateral positions of cells located within multi-layered micro-channels[68] including nanostructured surfaces which utilize an incoherent on-chip imaging modality.[69] In this design, the object of interest is directly positioned onto a nanostructured thin metallic film where the emitted light from the object plane, after being modulated by the nanostructures, diffracts over a short distance to be detected by a detector-array without the use of a lens. The far-field diffraction pattern then permits rapid reconstruction of the object distribution on the chip at the sub-pixel level using a compressive sampling algorithm. Some of these features were incorporated into portable devices suitable for use for global health including lensfree microscopy on a cellphone[70] with incoherent LED light scattered from each micro-object to coherently interfere with the background light, creating the lensfree hologram of each object on the detector array of the cellphone. The holographic signatures captured by the cellphone permit reconstruction of microscopic images of the objects through digital processing.

A compact lensless microscope based on lensless incoherent holography was developed for telemedicine.[71] This microscope utilizes a simple light-emitting-diode (LED) and a compact opto-electronic sensor-array to record lensless holograms of the objects, which then permits rapid digital reconstruction of regular transmission or differential interference contrast (DIC) images of the objects. Such a system was used for automated semen analysis.[72]

One common feature of such lensless devices is they require direct contact and coupling of the CCD/CMOS to the area to be imaged. This coupled design is not useful for fluorescent detectors which require excitation filters placed between the emitted light and the detector. Such filters prevent the direct coupling of the CCD/CMOS to the area to be imaged and significantly blur the captured image due to their thickness.

It is well recognized that lens free fluorescent imaging is challenging to achieve. To overcome the limitations of contact imaging for fluorescence detection, the area to be imaged has to be uncoupled from the detector so filters can be used. This issue was addressed in two recent publications demonstrating wide field fluorescent imaging on a chip using new optics combined with compressive decoding of sparse objects.

In these papers, to overcome the limitations of contact imaging for fluorescence detection, the area to be imaged has to be uncoupled from the detector so filters can be used. Wide-field fluorescent imaging on a chip using compressive decoding of sparse objects was described.[32] In this system, an LED or xenon lamp (tuned to an appropriate spectrum by a monochromator) excites fluorescently labeled cells or particles through the side facet of a prism (shown in Figure 1). The excitation light is reflected away from the sensor through total internal reflection (TIR) occurring at the bottom facet of the sample device, thereby eliminating the need for a high optical density interference filter. Excited fluorophores emit light through a 0.1 mm absorption emission filter into a coverless CCD or CMOS sensor enabling ultrawide field-of-view (FOV) of 2.5 x 3.5 cm. The resolution of the device was improved through digital deconvolution of the measured incoherent point-spread function of the lens-free system.

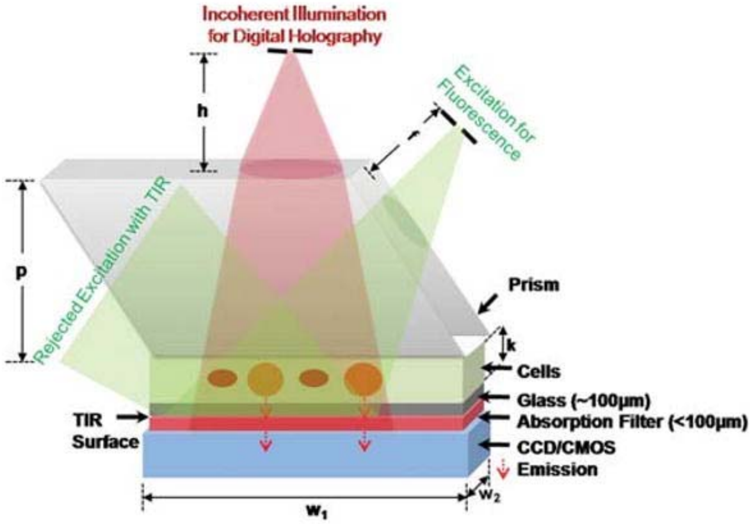

Figure 1 - Schematic of lensfree fluorescence microscopy based on optical holography [73]

Another approach for high spatial resolution fluorescent imaging for high-throughput imaging (e.g. cytometry, rare cell analysis or micro-array reading) was described by the same group.[74] In this lensfree imaging technique the fluorescent samples placed on a chip are again excited through a prism interface. The emitted fluorescent light from the specimen is collected through an on-chip dense fiber-optic faceplate and is delivered to a wide field-of-view opto-electronic sensor array enabling high spatial resolution imaging with field-of-view of >8 cm^2. One of the key elements in this approach is a thick (1 cm) fiber-optic faceplate which is used to collect the fluorescent emission from the specimen and to guide it to the detector array. This optical component therefore serves as replacement for a conventional lens, as both serve the purpose of collecting and re-directing light rays.

Söller collimators[75-77] are used in neutron and X-ray machines to produce parallel rays of particles or radiation. Without such a collimator, rays from many directions would be recorded and, the case of x-ray imaging, produce a blurred image. The Söller collimator utilizes a sandwich structure with layers alternating between transmitting material and absorbing material (e.g. lead, gadolinium). In this work, we adapt a Söller collimator concept to develop an optical Söller collimator based on a stack of pinholes (a stack of black acrylic plates with a micro-machined array of pinholes). This optical Söller collimator enables collimation of light from a plate assay through an emission filter directly onto a CCD in order to measure fluorescent signals.

In this study, the principle of low cost optical collimation using a Söller collimator was used to detect botulinum neurotoxin A (BoNT-A), one of seven serotypes (A–G) of deadly botulinum neurotoxin (BoNT) produced and secreted by clostridium botulinum. The gold standard laboratory test for botulinum toxin activity is the mouse bioassay.[78-80]

Alternatively, BoNT activity can be detected by assaying the enzymatic cleavage function of the toxin using specific peptide target substrates.[81-89]

Such cleavage activity has been detected by fluorescent reactions based on FRET-labeled peptide substrates that detect the cleavage of the peptide target substrates by the toxins though changes in fluorescence that can be measured via a variety of fluorescent sensors.[46,50,89-93] Lensless detectors may enable simplification of BoNTs detection. Moreover, such simplified detectors may address the need for low cost biodetection for use in resource-poor settings.

2.2 Fluorescence detection for mHealth

Many optical detection methods developed for biodetection employ photodiodes[94-97] and photomultipliers[98-103], which are highly sensitive spot detectors for analysis of limited areas. As an alternative, charge-coupled devices (CCDs)[103-111] have been used for spatial detection to monitor larger surface areas which has made them an ideal choice for high throughput multichannel detection. Several portable CCD based detection systems have been developed[112-119] based on single image capturing and analysis. Such detectors have sensitivity similar to that of current laboratory ELISA readers utilizing sensitive research grade cameras[112,113,120] or astronomical cooled CCD cameras[114-119]. While photomultipliers are far more sensitive than cooled CCD cameras, the longer integration times employed with CCD cameras can be used to compensate for their lower sensitivity[114-119]. However, such CCD devices are costly and not readily replaceable in the event of a failure, which limits their use in resource poor settings around the world.

There have been some notable recent developments in technologies that are suitable for low resource healthcare systems. Low cost microscopy was developed to address global health needs utilizing lens free approaches[121-129] and mobile phones have been adapted for biodetection[130-134]. These devices are based on low cost complementary metal-oxide-semiconductor (CMOS) sensors which are also used in webcam video cameras.

The fundamental issue that needs to be addressed in order for webcams to be used for biodetection is the low sensitivity and high noise of the CMOS sensors typically employed in these devices. One approach, described here, is to use multiple video captured images combined with time domain signal averaging (image stacking) for the detection of faint signals. While video mode is widely used for dynamic scene imaging, it has not been reported for applications in fluorescent biosensing.

2.3 Capillary-based fluorescence detection

mHealth is defined as "mobile computing, medical sensor, and communications technologies for healthcare."[138] This emerging field may enable the practice of medicine and improvement of public health in low resource settings by leveraging the recently observed penetration of mobile devices into these areas. With its enhanced mobility, mHealth has the potential to provide access to medical diagnostics for underserved populations and those in remote locations. Currently, most of the research in mHealth has been focused on exploiting the connectivity capabilities of mobile phones[139-143] and not on enhancing the analytical capabilities of mobile devices. At the same time, most analytical diagnostic technologies used today have been developed for laboratory settings in high-income countries, and in many cases are not affordable or compatible with the needs and conditions found in low and middle-income countries. The challenges and the need to develop simple, low-cost diagnostics for resource-poor settings with minimal medical infrastructure are well recognized.[144-146] mHealth analytical technologies can potentially be used to overcome the limitations of current medical diagnostics by providing simple and affordable analytical diagnostic technologies that are compatible with now-ubiquitous mobile phones technologies.

Several detection technologies based on mobile phones have been developed for biodetection, including an integrated rapid-diagnostic-test reader platform for lateral flow immunochromatographic assays[147], capillary array based immunodetection for escherichia coli[148], wide-field fluorescent microscopy[149], fluorescent imaging cytometry[150], lensfree microscopy[151], detection systems for melanoma or skin lesion[152-154], loop-mediated isothermal amplification (LAMP) genetic testing[155], microchip ELISA-based detection of ovarian cancer HE4 biomarker in urine[156], surface acoustic wave enhanced immunoassay[157], a pocket-sized colorimetric reader[158], phone-assisted microarray decoding platform for signal-enhanced mutation detection[159], and mobile phone cameras for DNA detection[160]. However, all these technologies rely on the inherent sensitivity of the CMOS camera native to the mobile phone, which is less sensitive than detectors used for biodetection. The camera sensitivity, which is a limiting factor for detection, may be improved through additional hardware or image processing algorithms to improve the performance of these devices.

To improve sensitivity of low cost but high noise detectors (e.g., $10 webcams) for mHealth applications, a computational approach was developed based on an image stacking algorithm to remove the noise and enhance weak signals for fluorescent detection to improve sensitivity[161]. While the computational approach increases the sensitivity of fluorescent detection, our unpublished data suggests that this approach may not be suitable for many portable phones because the native camera hardware in some phones filters out weak signals in an effort to reduce image noise, which renders computational approaches for weak signal enhancement useless. Since the computational improvement of low signals to increase detection sensitivity was not practical, optical amplification of the signals is needed to increase the level of light intensity from a fluorescent sample to one that is high enough that the phone camera hardware will not reject it as noise.

Improved limit of detection can be achieved using capillaries, which enable both assay fluid handling and waveguide excitation[162]. While a capillary array has been used previously to performing immunoassay for detection with a mobile phone[148], the capillary array was not used for optical signal amplification of the assay. Instead, a low limit of detection sensitivity (5–10 cfu mL^{-1} for E. coli) was obtained using fluorescent markers with improved quantum yield (quantum dots).

Capillaries have been used in several types of optical biosensors utilizing various excitation and emission modalities, optical path geometries and configurations shown in Figure 2 (adapted from Ref. [163]) including: (1) excitation and detection of emitted light perpendicular to capillary axis[164], (2) perpendicular excitation with guided-mode detection at one end[163,165], (3) guided-mode excitation with surface machined gratings to decouple the light out of the waveguide to the detector[166] (configuration is also used by fiber optic biosensors[167]), (4) guided mode excitation and emission at the same end of a capillary, and (5) guided mode excitation from one end and guided mode emission measured at the other end. Guided mode excitation generating evanescent wave illumination with perpendicular detection is used mainly for planar (not capillary) detection[168-171] as discussed in chapter 6.

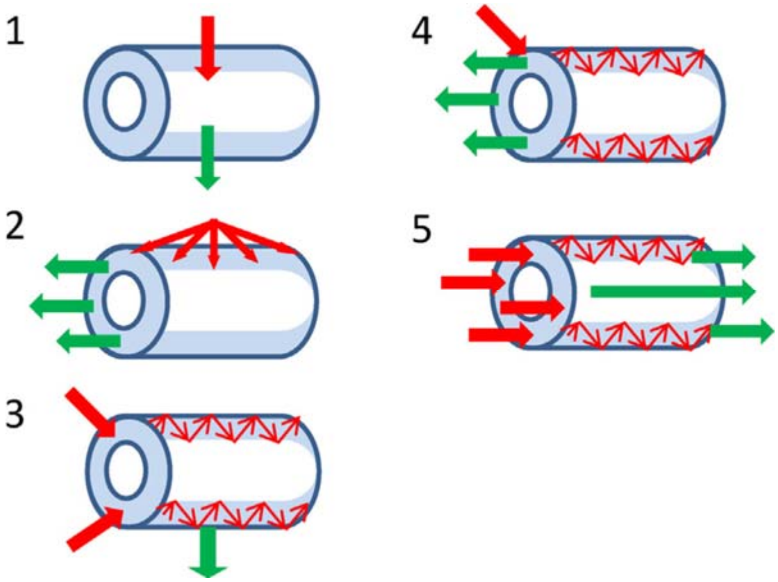

Figure 2 - Capillary optical configurations - Excitation light can illuminate the capillaries from several angles: a 90◦ angle (1 and 2) or angular/horizontal illumination utilizing waveguiding and evanescent illumination (3–5). The fluorescent signal emission can be detected at a 90º angle from the capillary (1 and 3) or horizontally after coupling into the waveguide and detected from the end of the capillary (2, 4 and 5).

However, most published capillary configurations are not suitable for mHealth applications because they require costly components such as photomultiplier tubes (PMTs) or cooled CCD detectors. These devices utilize complex optical configurations, have limited portability or are high cost, whereas effective mHealth devices should be simple, low cost and portable.

To enable the use of portable phones in mHealth applications involving highly sensitive fluorescent detection, we present an alternative optical enhancement approach which uses a standard portable phone with a CMOS imaging sensor combined with LED excitation in a very simple optical configuration: in-line horizontal excitation and horizontal detection (Figure 2-5). This optical configuration has been used effectively in previous work[161,172-179], however such configuration was used in planar (e.g., microtiter plate) mode and did not take advantage of the waveguide properties of capillaries for signal amplification.

In this work, we developed a new capillary waveguide optical configuration for fluorescence detection. While the conventional utilization of evanescent waves for fluoresce detection requires coherent light in the form of lasers[163,180-189] and a grating to decouple emitted light out of the waveguide and into a detector[166], in the simple configuration described here the capillaries were illuminated by the multi-wave length LED light emitted parallel to the capillary axis. The light-wave energy propagating through the capillary walls can interact directly with and excite fluorescent molecules near the capillary walls via evanescent waves, and light energy passing directly through the capillary core can directly excite fluorophores in solution. The fluorophores emit light that is detected at the end of the capillary to provide higher detection sensitivity when compared to the same volume of sample being detected in a standard microtiter plate format.

This is the basis for using the term amplification in this work: the measured fluorescent signal is increased substantially through the use of evanescent wave excitation compared to when it is measured by the same detector in a plate assay with the same illumination approach (e.g. direct LED illumination). The approach described here has the potential to form the basis for high sensitivity, low cost medical diagnostics in resource-poor settings.

2.4 Fluorescence based flow cytometry for rare cell detection

The driving motivation for this research is the problem of circulating tumor cell detection and enumeration. The primary mechanism of cancer metastasis is the dissemination of tumor cells into the circulatory system where they can be deposited in tissues around the body. These circulating tumor cells (CTCs) can be released into the blood stream by a tumor well before it is large enough for modern imaging techniques to detect it[196]. It is for this reason that CTCs have engendered significant interest in recent years as a possible early indicator of cancer. Because cancer survival rates improve dramatically at earlier stages of detection, it is believed that the accurate measurement of CTCs counts could serve as a valuable tool for reducing the worldwide burden of cancer[214].

It has been well established that the burden of cancer in low and middle income countries is substantial. Recent estimates indicate that approximately 56% of all cancer diagnoses and 64% of all cancer deaths occur in developing countries, demonstrating a significantly higher mortality rate than in developed countries[197]. This high mortality rate is attributed to what are typically late stage diagnoses of cancers. Out of all cancer deaths, the most common cause of death is tumor metastasis[198,199].

The most common method for measuring the concentrations of different cell populations is by use of a flow cytometer. Initially developed by IBM in 1965, the fundamental principles behind these devices has not changed significantly[200,201]. The devices are typically based on principles of light scattering (from Mie theory), absorbance or fluorescence. Conventional flow cytometers rely on PMTs (which are inherently single-point detectors) for sensitive measurement and must therefore image cells in a serial fashion (i.e. one at a time), which greatly limits sample throughput rates. Cytometers designed specifically for fluorescence or absorbance measurements can use imaging sensors such as CCDs to image large areas with hundreds or thousands of cells measured in parallel[202]. Alternatively, scanning optics can be used to image large areas one point at a time to enable the use of PMTs for area imaging[203].

With price points that start around $25k, this class of flow cytometer is typically designed for use in well-funded research and laboratory environments. These devices have been equated to the original IBM mainframe computers, which were large, expensive, and only in the hands of a limited number of organizations[9]. Developing a personal computer analog of the flow cytometer with a price-point similar to that of the original personal computers (<$5,000) has the potential to enable widespread adoption of this technology in developed countries[204,206]. This could allow for significant improvements in diagnosis time in clinical healthcare settings, as well as allowing a broader base of researchers access to a tool that is uniquely capable of accurate cellular analysis.

A price-point of \$5,000 is, however, still too high for wide spread adoption in low and middle income countries. There has been some research recently into developing low cost cytometers which utilize cell phones and inexpensive ancillary components in order to address this need[208,209]. The devices which have been developed are primarily useful for conducting classic cytological tests (blood content analysis, screening for parasites, $CD_{4/8}$ tracking for HIV patients, etc.) where sample volumes of 1 mL or less are required and cells of interest are available in concentrations of 10^3-10^9 per mL, and they therefore utilize flow rates on the order of 1-10 µL/min (similar to conventional flow cytometer flow rates). Currently available research indicates that diagnostically relevant numbers of CTCs in peripheral blood are on the order of 1-10 cells per mL, and typical analysis volumes are 7.5 mL. Analysis of this sample volume at a flow rate of 1-10 µL/min would require between ~1.6 and 16 hours to complete. In settings where dozens of tests may be required per day and only one analysis device is available, these analysis times are far too slow.

To address these issues, we have developed a technique for wide-field cytometry that has allowed for extremely high throughput detection and accurate counting of rare cells. This technique relies on the principles of cell streak imaging with spatial/temporal signal averaging. This operational mode has not been reported previously for applications in cytometry. The nearest analog is particle streak velocimetry: a now outdated[211] technique for estimating local fluid velocities (replaced by particle *image* velocimetry). Developed in the first half of the 20th century, the technique relied on fluids being seeded with particles, illuminated, and then photographed while in motion. Existing camera technology limited exposure times, meaning that for fast moving flows particle images were resolved as streaks instead of points. The direction and relative length of these streaks was used to measure localized fluid motion (i.e. velocity, vorticity, etc). We have adopted the fundamentals of this technique for the purpose of improving the sensitivity and throughput for fluorescent flow cytometry using a low cost image sensor.

Every example of flow cytometry found in literature relies on capturing cell signals at frequencies high enough that signals are not distorted in time or space. When using PMTs, which are inherently a point measurement tool, this translates to using an integration time which is short enough to prevent cell signals being overwhelmed by background noise, as well as allowing cells with narrow spatial/temporal separation in the flow to be distinguished. In cytometry platforms targeted for low price points, where PMTs are exchanged for imaging approaches such as CCDs, typical approaches are to use low flow rates or static cytometry (i.e. imaging large numbers of cells spatially fixed on a microscope slide or similar substrate)[204-207]. As with conventional flow cytometry, these approaches limit the total rate of sample throughput and are not suitable for rare cell detection.

There have been several promising low-cost LOC solutions for CTC screening put forward recently[212,213]. These devices work on whole blood with little sample preparation required, which could potentially improve net sample throughput compared to a fluorescent labeling approach. However, the devices must be operated at very low flow rates (1-2 µL/min) in order for their high capture efficiencies to be realized. At these flow rates a single 7.5 mL sample would require over sixty hours to fully analyze.

It is evident that there is an outstanding need for a low cost, high throughput solution for cytometric analysis. While a complete solution to this problem is beyond the scope of this dissertation, the beginnings of a solution are presented in chapter 8. Here the problem of low-cost, high-throughput counting of rare cells is addressed using fundamental methods adopted from the areas of machine vision and astronomical imaging.

3. Compact lens-free optical collimation

A technique for designing a compact, robust and simple to manufacture collimation device for fluorescent LOC assay reading was developed. The fundamental principle was adopted from the field of x-ray and neutron physics where devices known as Söller collimators perform a similar task. Presented first is the development of the proof of principle device along with results from a bio-detection application. This is followed by a parametric analysis of device performance along with formulae which allow for device optimization.

3.1 Device development

We developed a simple CCD based lensless fluorometer with sensitivity in the range of current ELISA plate readers. In our lens free fluorometer, a multi-wavelength LED light source was used for fluorophore excitation. To collimate the light, we developed a simple optical Söller collimator based on a stack of pinholes (a stack of black acrylic plates with an array of pinholes machined through their thickness) enabling the light to be directed from the LED through the filters and the assay's microfluidics directly onto the CCD without a lens. The elimination of the lens that is used in almost all other current CCD based detection systems has two major advantages: (1) it simplifies the device design and fabrication while reducing cost and (2) it reduces the distance between the sample and the measuring device (without a lens the distance needed to focus the image on the CCD is reduced and the fluorometer can be more compact). Two advantages of the Söller collimator over other published examples of lens free biodetection platforms are: (1) it allows the use of filters for fluorescence detection and (2) it uncouples the CCD and the microfluidics to enable the use of interchangeable fluidics while protecting the delicate CCD. In the demonstrated configuration, the lensless CCD-based fluorometer is capable of detecting 16 samples simultaneously. It was used for *in vitro* detection of botulinum neurotoxin serotype A (BoNT-A) activity with a Förster resonance energy transfer (FRET) assay that measures cleavage of a fluorophore-tagged peptide substrate specific for BoNT-A (SNAP-25) by the toxin light chain (LcA). For this assay the LOD of our lensless fluorometer is 1.25 nM, which was identical to the LOD of a modern plate reader analyzing the same assay products. Combined with microfluidics, this simple low cost point-of-care medical diagnostic system may be useful for the performance of many other complex medical diagnostic assays without a laboratory and thus potentially enhancing the accessibility and the quality of health care delivery in underserved populations.

3.1.1 Materials and methods

Materials and reagents

The recombinant light chain of BoNT A (LcA) and SNAP-25 peptide substrate, internally labeled with the FRET pair fluorescein-thiocarbamoyl (FITC) and 4-(dimethylaminoazo)-benzene-4-carboxylic acid (DABCYL) used for measuring BoNT-A activity, were purchased from List Biological Laboratories (Campbell, CA). Also obtained from List

Biological Laboratories was the FITC-labeled SNAP-25 (Unquenched SNAP-25; not labeled with acceptor DABCYL) used for measuring the sensitivity of the device. The 16-well chips used for analysis were fabricated using 1/8 inch black poly(methyl methacrylate) (PMMA), also known as acrylic, and polycarbonate (PC) (Piedmont Plastic Inc, Beltsville, MD) bonded with 3M D786BL black adhesive transfer double sided tape.

Lensless fluorescence detector

The lensless fluorimeter consists of a multi-spectra LED light source[90], blue excitation D486/10X and green emission HQ535/50M filters (Chroma Technology Corp, Rockingham, VT), and a Mead Deep Sky Imager PRO III CCD camera (Adirondack Video Astronomy, Hudson Falls, NY). All system components were enclosed in a black plastic box. The detector employed a Sony ICX285AL 1360x1024 pixel CCD and was connected to a Windows XP PC via a USB port and controlled using Mead AutoStar Suite software. The CCD image intensities were analyzed using ImageJ software, developed and distributed freely by NIH (http://rsb.info.nih.gov/ij/download.html), and the data generated was then imported into Microsoft Excel (Microsoft, Redmond, WA) for analysis. SPA-RP Reflectance Probe spectrometer was used for spectral analysis (Photon Control, Inc).

Fabrication of the 16-well sample fluidics

The 16-well sample chips used in this study were designed in CorelDraw X4 (Corel Corp. Ontario, Canada) and then micromachined in 1/8 inch black acrylic using a computer controlled Epilog Legend CO2 65 W laser cutter (Epilog, Golden, CO). Before cutting, one side of the acrylic sheets were coated with 3M D786BL black adhesive transfer double sided tape to allow for a polycarbonate backing to be attached to define the back side of the fluidic device.

High resolution CO_2 laser micromachining

The Epilog Legend CO2 65 W laser cutter used for micromachining of microfluidic sample chips is capable of a mechanical resolution of 1200 dpi. The melting of plastic materials during laser cutting may reduce this to a much lower effective resolution depending on the material being used. To overcome this problem, the cutting of elements was carried out in multiple steps using lower levels of laser power with enough time between steps to permit local cooling that limited the volume of material that would be melted.

FRET Assay for LC-A and BoTN A activity detection

The SNAP-25 FRET-based assay was used in this study for the detection of BoTN-A LcA following the manufacturer's instructions. 40 nM LcA was prepared in 200 µl 20 mM HEPES + 0.2 mM ZnCl + 1.25 mM DTT (assay buffer) and a 50% serial dilution series prepared in 1 ml Eppendorf reaction tubes using assay buffer. A buffer blank (a control) was included in each assay. The quenched SNAP-25 peptide was then prepared at 10 mM in assay buffer and 100 µl was added to each tube, giving a final quenched SNAP-25 concentration of 5 µM per tube and an LcA range of 0–20 nM. These samples were then incubated, at 37 ºC for 2 hr. After incubation the samples were transferred to an ELISA plate and analyzed in a fluorescent plate reader (Tecan Infinite m1000), followed by transferring 3.2 µl per well to the 16 well chip for lensless measurements.

Data collection and analysis

Fluidic chips were loaded via micropipette with 3.2 µl per well of the sample in question. After loading, chips were installed in the described lensless fluorescence detector. Four sequential fifteen second exposures were taken of each sample chip with the excitation light source turned on (light frames), followed by four fifteen-second exposures with the source turned off (dark frames). Each set of images was combined and averaged using ImageJ software. The averaged set of dark frames was then subtracted from the set of light frames in order to remove background noise present in the CCD. Images were captured using 2x2 on-chip pixel binning. The resulting image of resolution 680x512 was further binned in ImageJ in order to facilitate the identification and selection of areas of signal. Square bins of 64 pixels (8x8) were averaged in order to produce a final image resolution of 85x64. This step was carried out for convenience and does not affect actual signal-to-noise ratio. Samples which were measured included SNAP-25 FRET based assay prepared as described previously, a 50% serial dilution of unquenched peptide used in the assay with buffer, and a 50% serial dilution of fluorescein in water. In order to quantify any innate well-to-well variance, chips loaded with water only were measured. Standard deviation of average signal in chips loaded with water ranged from 7.8–10.2% with an average of 8.7%. Detection for the SNAP-25 assay was limited to a concentration of 1.25 nM: identical to the result achieved by a fluorescent plate reader (Tecan Infinite m1000). This result is based on the statistical analysis of measurements taken from six separate sample chips using two replicated assay dilutions, and the measurements taken of the same samples using a conventional fluorescent plate reader. A limiting t-statistic of 0.05 was used to determine statistical difference between samples.

3.1.2 Results and discussion

The lensfree CCD-based fluorometer described in this study was designed with the aim of simplifying fluorescence detection by eliminating the lens, and thus produce a low-cost, compact, portable, and simple fluorescence detection system capable of measuring multiple samples simultaneously. A simple modular design increases the versatility of the system by allowing the user simple switching of excitation wavelengths and filter sets when using different fluorescent detection systems. We chose the BoTN-A FRET-based activity assay to demonstrate the design and utility of the prototype lensless detection platform.

Lensfree CCD-based fluorometer

The basic configuration of the lensless CCD-based fluorometer is shown schematically in Figure 3 along with an actual photograph of the detector (Figure 3C) and photos of key elements (Figure 3 A). A photo of the actual device is shown in Figure 3-C-II. The system consists of four modules (described in detail in following sections): (1) the illumination module, which consists of a multi-wavelength LED illuminator and the excitation filter, (2) the light collimation module consisting of two collimators and the emission filter, (3) 16-well microfluidics system for the assay and (4) CCD camera. The light path of the lensless CCD-based fluorometer is shown in Figure 3B: LED light is filtered through the excitation filter used to excite fluorescence in the fluidic chip. The light is then partially collimated by collimator 1, filtered by the emission filter, further collimated by collimator 2 and measured by the CCD.

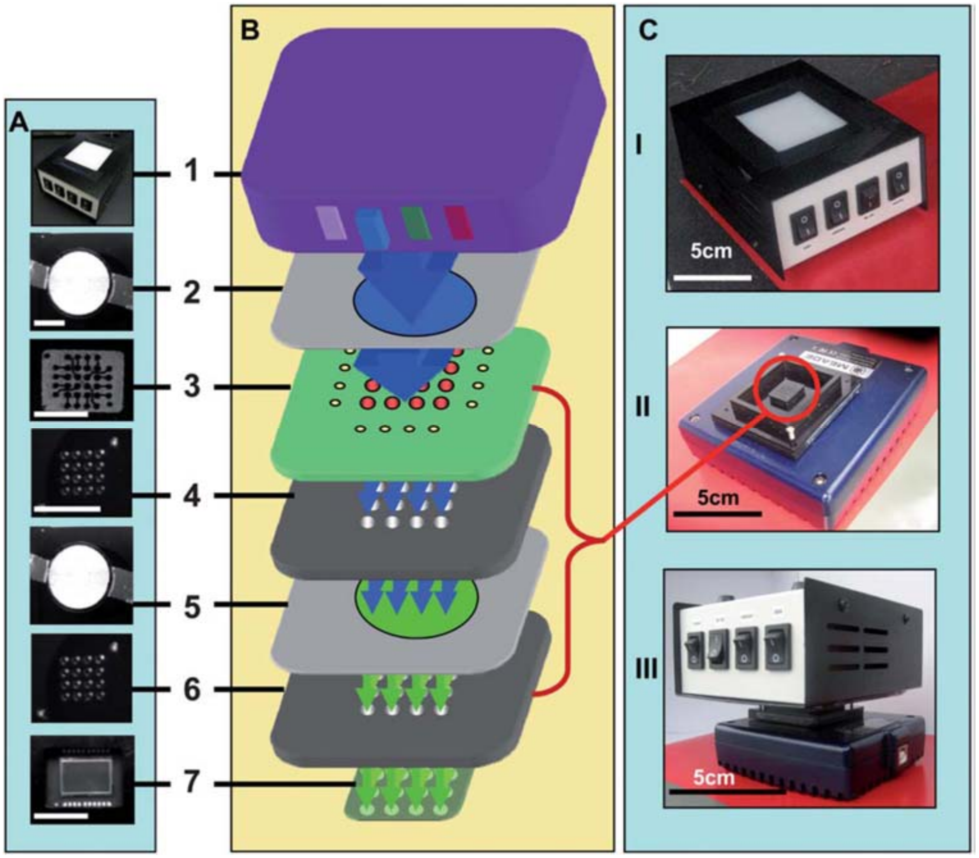

Figure 3 - Basic elements and configuration of lensless detector - (A) a photograph of the basic elements of the lensless detector (the size bars are 1cm), (B). a schematic configuration of the detector and (C) a photograph of the assembled lensfree detector (the size bars are 5 cm). For panels A and B the main elements are 1. multi-wavelength LED illuminator, 2. narrow band blue emission filter, 3. detector assay microfluidics, 4. light collimator #1, 5.green pass excitation filter, 6. light collimator #2 and 7. the CCD camera. Panel C shows photos of the system I. multi- wavelength LED illuminator, II. the assembled light collimation module placed on the CCD and III. the assembled lensfree detector.

LED illumination module

The LED illumination module[90] is comprised of a custom built multi-wavelength LED illumination box (Figure 3-A-1) and the excitation filter (Figure 3-A-2). The multiwavelength LED illumination box can illuminate with red, green, blue or white spectra capable of exciting multiple fluorophores, however only illumination in the blue range is needed for the FITC excitation used in this study. Each LED color is controlled individually with a switch in the front panel and the top of the illuminator consists of a diffusion panel which assures uniformity of the LED light.

Light collimation module

While current lensless imaging relies on direct contact imaging, for fluorescence detection the area to be imaged has to be uncoupled from the detector so filters can be used. Our approach to uncouple the plate assay from the CCD is based on an optical Söller collimator. The collimator consists of two black PMMA plates each with an array of holes micromachined with a CO_2 laser, which produces 16 approximately parallel beams of light aligned in a specific direction and focused onto the CCD. This micromachined optical Söller collimator is the key element of our approach. Söller collimators, typically used in neutron and x-ray machines, collimate radiation by using a sheet of material opaque to the incoming radiation with high aspect ratio holes or slits for the radiation to pass through. For the optical Söller collimators we used sheets of black acrylic opaque to the incoming light with arrays of high aspect ratio holes bored through their thickness. Each of the two collimators used is a black 3.2 mm acrylic plate with a 4x4 grid of holes (radius 0.65 mm). Collimator 1 (Figure 3-B-4) is placed under the assay plate (Figure 3-B-3) and focuses the light emitted from the assay into the emission filter HQ535/50M (Figure 3-B-5). Collimator 2 (Figure 3-B-6) is placed on the CCD (Figure 3-B-7) and further focuses the light after it passes through the filter. The spacing and aspect ratio of the holes in the collimators (determined experimentally) is critical to minimizing optical cross talk between channels and the diffusion of the image. A photo of the assembled light collimation module on the top of the CCD is shown in Figure 3-C-II (the assembly in the circle).

Optical design strategy

In the Söller collimator, the principle for collimation is to use high aspect ratio transmitting features (such as holes or slits) to filter out rays of radiation that are not already aligned to the optical axis of the feature. For our application, the distance between the collimator and object plane is small in order to gather as much light as possible from each point in the source. In addition, a hole aspect ratio of approximately 4 : 1 is used to keep a balance between minimizing the angle of divergence (which is the angle of beam spread calculated as $\tan^{-1}(w/h)$ where w is hole diameter and h is hole height) and maximizing the transmission of the source.

The divergence angle is governed by the packing of reaction wells on the fluidic chip and the distance between the reaction wells and the image plane. To begin with, an array of reaction wells was designed to fit in the area of the given CCD sensor with maximum density. The density of the well packing was determined by empirical tests concerning the maximum feature density producible by the laser cutter on the plastic in question. The results of these tests produced a 4x4 grid of wells with dimensions 6x6 mm.

As previously stated, the best reading from the detector was achieved when the maximum divergence angle was used that still prevented cross-talk of light between wells. This is because a maximum divergence angle is achieved by using a minimum collimator height. By minimizing the height, losses in light intensity are also minimized.

CCD detector

We used a Mead Deep Sky Imager PRO III CCD camera, which is a relatively low cost consumer CCD camera. The camera is equipped with a low noise monochrome Sony ICX285AL 1360x1024 pixel CCD chip with a 16 bit analog-to-digital converter. The camera is powered by its USB port and can be controlled with Labview software, allowing field use and simple system automation. The camera is capable of long exposure times that are needed for low light detection.

Light characteristics of the lensless detector illumination

The multi-wavelength LED illumination box provides illumination in the blue, green, red, and white ranges, covering a spectrum of 450–650 nm. The BoNT-A FRET-based activity assay used here is based on FITC measurement with peak excitation wavelength of 494 nm (Figure 4-I-A) and emission maximum of 521 nm (Figure 4-I-B). The blue LED emits in the range 420–550 nm (Figure 4-II-C) with a peak at 470 nm. The broad emission spectrum of the blue LED overlaps with the FITC emission so to minimize interfering optical signals a bandpass filter with center wavelength and FWHM of 486 nm and 10 nm (Figure 4-II-D) was used for FITC excitation. For emission a bandpass filter with center wavelength and FWHM of 535 nm and 50 nm (Figure 4-II-E) was used. In our optical configuration the excitation source is directly in line with the CCD, so the excitation and emission filters are crucial for blocking any excitation light reaching the detector, while still allowing the fluorescence emission to be transmitted. For the exposure times used, there is no detectable overlap between the spectra of the blue and the green filters which are well separated (the double head arrow in Figure 4-II).

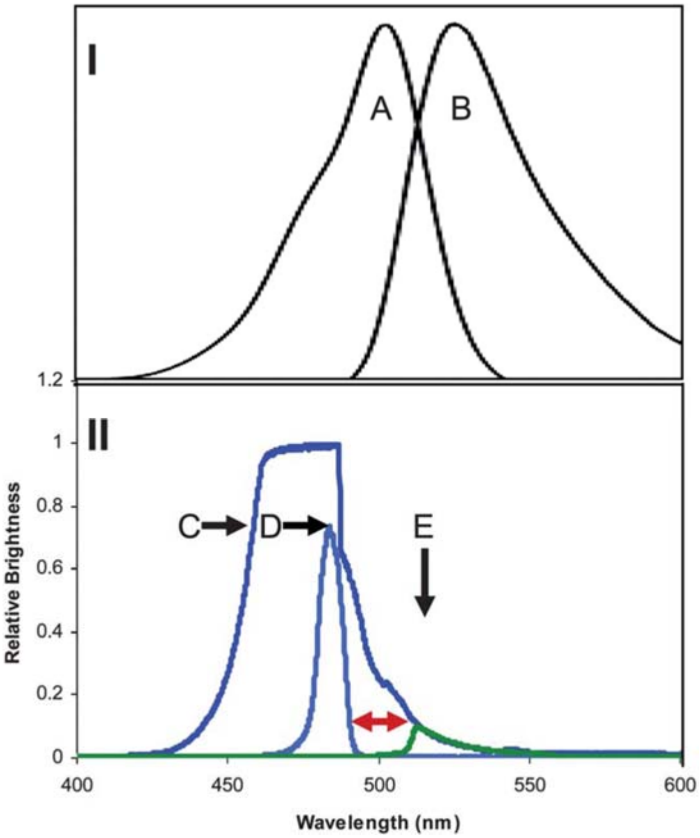

Figure 4 - Light characteristics of lensless detector illumination - I. Spectra of FITC; (A) excitation and (B) emission spectra. II. Spectra of the LED illumination module: (C) blue LED emission spectra, (D) spectra of blue emission filter, (E) spectra of green emission filter, and the double head arrow shows the gap between the filters spectra.

Design and fabrication of the detector assay microfluidics

One challenge for conducting biological measurements with the 16-well lensless detector is the small dimension of the detector assay module, which is determined by the size of the

CCD (10.2x8.3 mm). The assay chip is loaded with the sample, and then placed above the collimator module prior to measurement. The interchangeable assay module enables analysis of small volumes (3.2 µl) in a practical manner. The assay module is a two layer microfluidic structure constructed with a rigid polymer core (3.2 mm PMMA) and laminated with layers of thin polymer (polycarbonate film) bonded with adhesive. The relatively thick core provides rigidity to the assembly and forms fluidic reservoirs for detection wells. The thin polymer laminating layers seal the chip. Figure 5 B shows the functional elements of the microfluidics system, including wells cut through the PMMA used to load and detect the samples. Outlets were used as vents by cutting through the PMMA, and channels were engraved in the PMMA to connect them. The fluid flow is shown in Figure 5 A. Samples are loaded directly into the well (arrows pointing down). The assay sample and the air displaced by the samples vents through the outlets (arrows pointing up). An actual fluidic chip is shown in Figure 5 C. The assay microfluidics is aligned to the collimation module using the alignment holes in a two pin device alignment system.

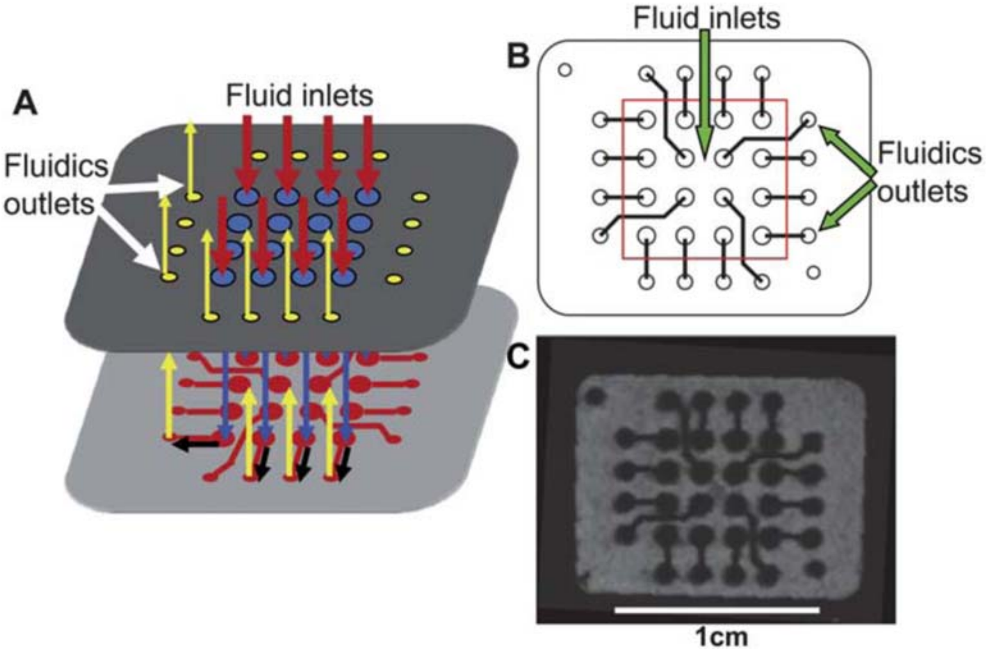

Figure 5 - Functional elements of the microfluidic system - (A) a diagram of the fluid flow from the loading wells (down arrow) into the detection wells and the microfluidic outlets (up arrows) through the channels engraved in the acrylic. (B) Schematic of the microfluidic system and (C) a photo of the microfluidic chip.

Lenless CCD-based fluorometry

To study the capabilities of the lensless CCD-based fluorometer, solutions from the serial dilution of the FITC-SNAP-25 (unquenched peptide) were loaded into the 16-well sample chip and the resulting LED excited CCD image recorded. The unquenched FITC-SNAP-25 contain the cleavage sequence for BoNT-A, but because it is not quenched by DABCYL it emits light continuously when excited. Therefore, measuring this peptide enabled us to analyze the sensitivity of the lensless CCD-based fluorometer for BoNTA activity.

Images were captured on the detector using a 15 s exposure (Figure 6-I). In this experiment, only 12 wells (row B, C and D) were used for the unquenched SNAP-25. In row A are the wells with no peptide (control). The light intensity in the wells with the unquenched SNAP-25 varies with the peptide concentration. At the highest concentration (20 nM) in well B4, the signal is very bright and it decreases with decreasing concentration of the peptide (from right to left in Figure 6-I).

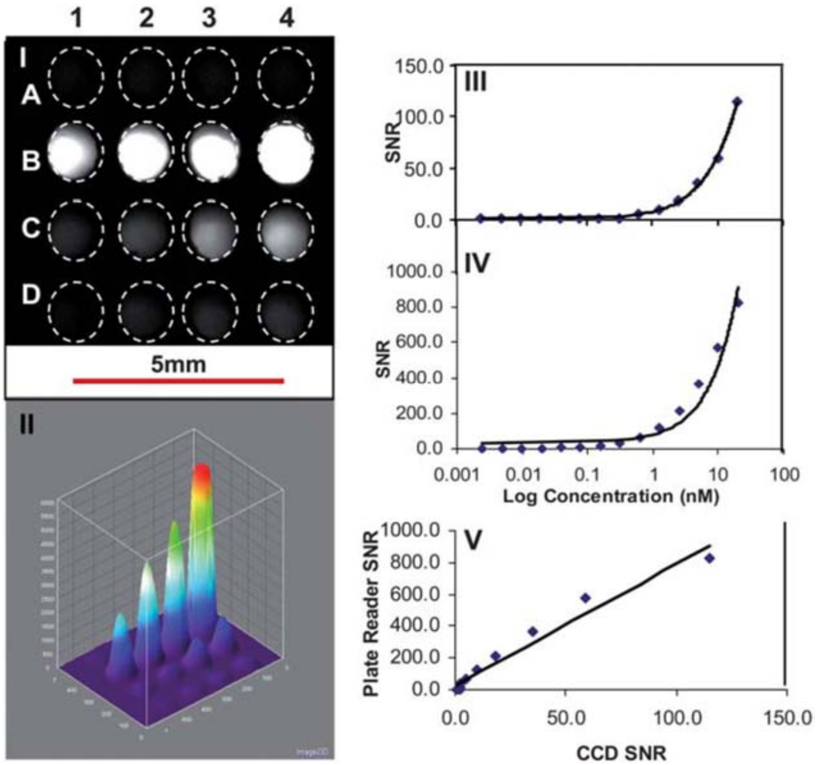

Figure 6 - Lensless CCD-based fluorometry results - A serial dilution of the FITCSNAP-25 (unquenched peptide) was loaded into the 16-well sample chip and the resulting LED excited CCD image after 15 s exposure was recorded. I. An image of the serial dilution emission, the wells are marked with white dashed circles. Row A wells with no peptide, the samples were loaded in the order of decreasing concentrations of the peptide (from right to left). II. A 3D representation of I showing the intensity signal of each well. III. Plot of ImageJ quantization of I. IV. Plot of the value from the same serial dilution of the FITC-SNAP-25 measured by plate reader. V. The correlation analysis of the measurements between identical samples measured by the plate reader and the lens free detector.

The collected CCD images were analyzed in ImageJ. A plot of the data from Figure 6-I is shown in Figure 6-III, which indicates that there is a strong linear correlation ($R^2 = 0.9986$) between the concentration of the peptide and the signal to noise ratio (SNR).

The same samples of varying concentrations for FITC-SNAP-25 were analyzed with a commercial fluorescent plate reader (Tecan Infinite m1000), as shown in Figure 6-IV, a similar response was measured with the commercial device showing that there is a strong linear correlation ($R^2 = 0.9483$) between the concentration of the peptide and the SNR.

A t-test analysis was performed (in Excel) to determine the LOD, which represents a measured concentration that generates a signal that is significantly different from the control sample measurement from data from 6 chips (two replicas of the serial dilution each measured with 6 chips). LOD for the plate reader was found to be 4X lower than that of the lensless CCD-based fluorometer. The SNR at the limit of detection for the plate reader was 1.26, and the SNR limit for the CCD-based fluorometer was 1.20. These results suggest that the performance of our lensless CCD-based fluorometer is similar (within the same order of magnitude) to the performance of conventional fluorescent plate readers.

Lensless detection of botulinum toxin activity

To demonstrate the utility of the lensless CCD-based fluorometer for measuring fluorescent-based solution assays, we chose a FRET-based peptide assay for measuring the activity of BoTNA. In this assay, a short chain peptide sequence of the BoTN A cleavage target protein of the neuromuscular junction (SNAP- 25) is labeled with the FRET pair

(FITC/DABCYL). The very close proximity of the DABCYL causes significant quenching of the FITC fluorescence. Binding of BoTN A or its light chain derivative LcA results in cleavage of the peptide sequence measured an increase in FITC fluorescence. In this assay, the FITC/DABCYL-SNAP-25 peptide was prepared at a fixed 10 mM concentration and exposed to LcA at concentrations in a 50% serial dilution series varying from 0.0195 to 20 nM. A negative control with peptide but no LcA was also included. Following the two hour incubation at 37 ºC, the samples were transferred to an ELISA plate and analyzed in a modern commercial fluorescent plate reader followed by transferring (3.2 μl) samples to the 16-well sample chip for lensless measurements at 15 s of exposure time. In these experiments the active subunit of the toxin, which is the light chain, was used because although the LcA unit cleaves the peptide, it is not toxic without the heavy chain which is important for targeting the toxin.

Plots of the ImageJ analysis are shown in Figure 7-I. There is a strong linear correlation ($R^2 = 0.9815$) between the concentration of the LcA and SNR for the lensless fluorescence device. Data taken from measurements of the same samples *via* plate reader is shown in Figure 7-II. A similar response was measured with the commercial device indicating a strong linear correlation ($R^2 = 0.9922$) between the concentration of the peptide and SNR. The results from the lensless CCD-based fluorometer were compared to the results from the plate reader, as shown in Figure 7-III. There is a strong linear correlation ($R^2 = 0.978$) between the measurements of both detectors.

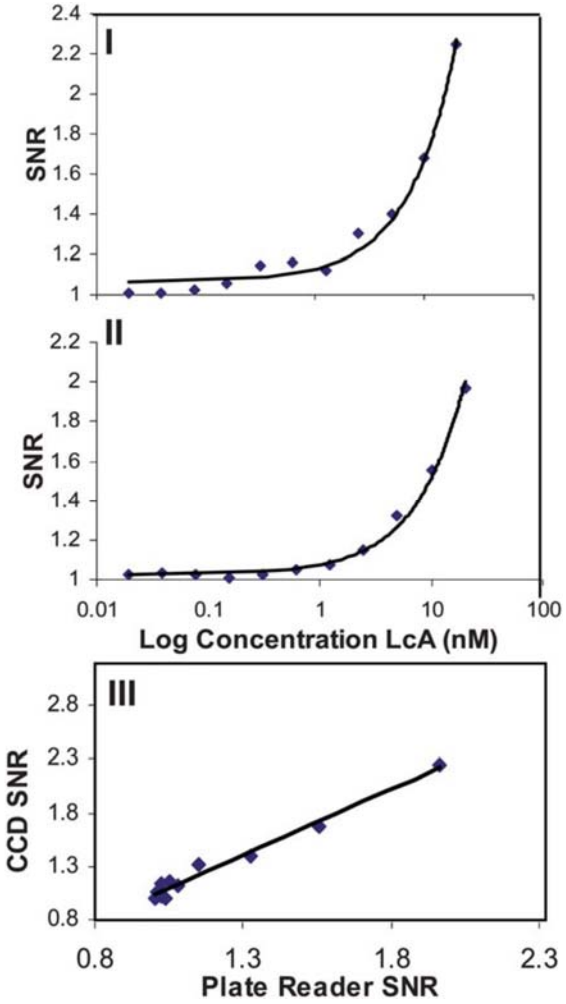

Figure 7 - Lensless in vitro activity detection of BoNT-A light chain (LcA) using the SNAP-25 cleavage assay - The SNAP-25 peptide substrate for BoTN-A is labeled with the FITC donor/DABCYL acceptor FRET pair. Cleavage of the substrate by the toxin light chain (LcA) disrupts the FRET resulting in increased FITC donor emission as measured by CCD with 15 s exposure. The FRET activity assay was performed in a 16 well plate with different concentrations of 2 fold LcA serial dilution in the range 0 to 20 nM. The assay was carried out for two hours in room temperature. The SNR of the FRET activity assay was calculated as the ratio between the value of the measurement to the value of the control (no LcA) and was plotted for (I) the lensless detector, and (II) the commercial plate reader. (III) Shows the correlation between the two device measurements.

T-test analysis was performed to determine the LOD for LcA detection (two replicas of the serial dilution each measured with six chips). For the lensless CCD-based fluorometer, the LOD is 1.25 nM, and for the plate reader the LOD (two replicas of the serial dilution each measured nine times) is also 1.25 nM. The LOD in previous results using the same assay were in the range 0.5-1.25 nM[50,90,92] These results suggest that the lensless CCD-based fluorometer is equivalent to the fluorescent plate reader and in the range of previous measurements of the BoNT-A activity detection assay.

3.2 Collimator design principles and modeling

The goal of collimation is to produce light rays which propagate parallel to one another. Thus an ideally collimated beam would not diverge over infinite distance (Figure 8-B). Classical collimating devices such as mirrors and lenses approximate this perfect collimation with varying degrees of success (Figure 8-C), which is one measure of the quality of these optical elements. However even a theoretically perfect lens could not produce a perfectly collimated beam due to diffraction effects. The question then is not of whether light is collimated or not, but to what degree it is collimated. The goal of the optical Söller collimator is therefore not to achieve perfect collimation, but to achieve a usably high degree of collimation.

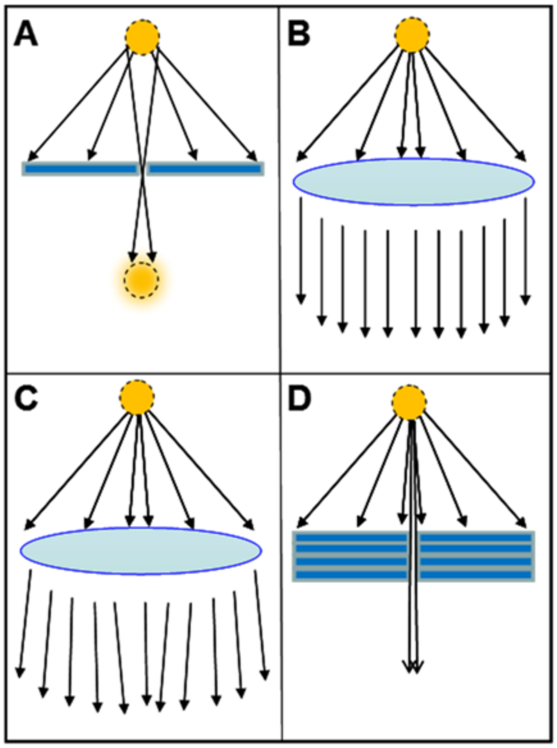

Figure 8 - Comparison of ideal and actual collimators - A) Pinhole apertures can produce an image, but the rays are not collimated. B) An ideal optical collimator (a lens in this case) will collimate any rays which emanate from its focal point. These rays will never converge or diverge over infinite distance. C) An actual lens, even a perfectly fabricated one, can never perfectly collimate light due to diffraction effects. D) An optical Söller collimator approximately collimates light by only passing rays which are nearly parallel to its optical axis.

The basic principle behind our optical Söller collimator is seen in Figure 8-D. It can be seen that our collimator bridges the gap between a traditional pinhole aperture (Figure 8-A) and a classical collimating element (Figure 8-C). The main element of the Söller optical collimator is the transmitting/absorbing array. As with traditional Söller collimators used for x-ray sources, this array is composed of two materials: one which absorbs and one which transmits the electromagnetic radiation in question. For our optical collimator we use black acrylic to absorb the light and air (holes) to transmit it. Light rays that diverge from the optical axis and strike the collimator walls are absorbed, so that the only light rays that exit are those which are propagating in the direction of the optical axis (or very near to it). The spacing of the holes in the collimators is critical to minimizing optical cross talk between channels by light rays that diverge from the optical axis and cause diffusion of the image.

Light ray modeling of optical Söller collimator

By increasing the thickness of the Söller collimator (marked as ‘L’ in Figure 9 B) it is possible to reduce the number of light rays that diverge from the optical axis. At the same time, the intensity of the light will also decrease with the increasing thickness because fewer light rays will reach the sensor. This tradeoff is demonstrated by comparing Figure 9 C and D. Image C was captured using a thin collimator, resulting in overlap between channels in the image. Image D was captured using a collimator 2.5 times thicker, resulting in a well-defined image where each channel is distinctly separate from its neighbors. At the same time the average intensity of each channel decreased by 77.5% (from an average pixel value of 51,000 to 11,500). To compensate for this, long exposure times can be used. Light from each sample cannot be accurately analyzed if there is overlap as seen in Figure 9 C. For less collimated light, the spacing between sample wells must be increased to prevent crosstalk. When there is better collimation, as seen in Figure 9 D, the density of sample wells can be increased and the throughput can be improved.

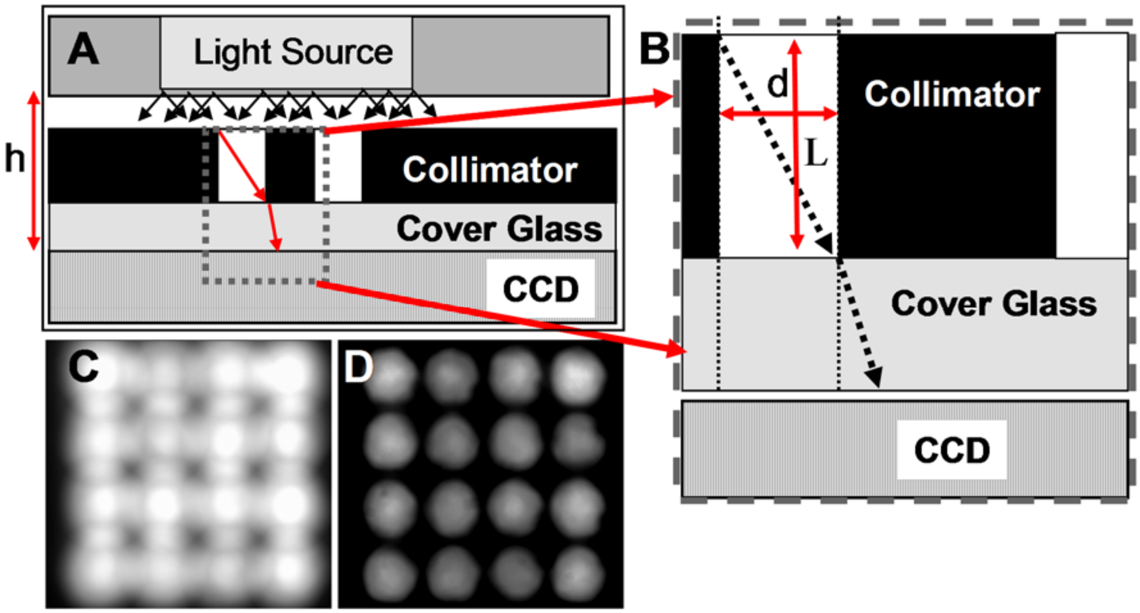

Figure 9 - Schematic of optical Söller collimator array - A) Side cutaway view of an array Söller collimator. The light path is shown from the light source through the collimator, refracting through the glass filter, and striking the CCD. B) Enlarged view of the collimator cross section showing critical dimensions. Aspect ratio is defined as L/d. C) Image captured using a collimator with too low an aspect ratio for a given hole spacing (note image overlap). D) Image captured using a collimator with suitably high aspect ratio. Note the well-defined image spots. Irregularities in hole circularity are imperfections due to laser machining.

The critical issues with the use of Söller optical collimators for biosensing are light distribution and intensity. A basic element defining the effectiveness of optical Söller collimators is the aspect ratio. This is the ratio of the length of the light-transmitting channel to its diameter. A higher aspect ratio indicates a longer/thinner channel, which as noted previously results in a higher degree of collimation and lower light output.

To analyze the Söller collimator, we used a conventional ray analysis. A schematic representation of the light ray path for our Söller collimator can be seen in Figure 9 A/B.

For the purposes of analyzing the performance of the collimator itself we removed many of the components used in the previously described experiment (including filters (Figure 3-A-2 and A-5) and the microfluidic chip (Figure 3-A-3 and B-3)). In our ray analysis we assumed that our light source was a uniform emitter. In other words, every point on the emitting surface has a uniform distribution of intensity in all directions. This assumption was checked using a spectrometer (Photon Control SPM-002-D) to verify spectral distribution and intensity levels at various angles from 5º to 90º and found to be accurate with an average intensity variation of less than 10%. The surface was then modeled as a collection of differential areas emitting uniformly and spherically, and the intensity contribution of each emitting area was summed over the detector surface. The geometry of the optical Söller collimator forces light to be constrained to certain areas of the detector, and this is reflected in the ray tracing.

To compute the final light intensity distribution from such a differential model we derived an integral equation to sum the individual intensity contributions from the two-dimensional emitting surface. The equation is for a single-hole collimator. To analyze the light distribution on the CCD/CMOS detector, we used the following equation:

$$\mathrm{I(x,y)} = \int_{y-(y+d/2)*h/L}^{y-(y-d/2)*h/L} \int_{x-(x+d/2)*h/L}^{x-(x-d/2)*h/L} F(x',y')dx'dy' \qquad (1)$$

where ‘d’ is the diameter of the collimator hole (see Figure 9 B) for the Söller collimator, ‘h’ is the distance from the illumination source to the CCD sensor, L is the length of the collimator hole, and F(x’,y’) is the intensity distribution of the illumination source. For our case, the distance ‘L’ varied from 3 mm to 25 mm, ‘h’ was fixed at 200 mm, and the illumination source was 50 mm in diameter (a variable which is incorporated into F(x’,y’).

Aspect ratio is the ratio of hole length to diameter (L/d). For this model, secondary (reflected) rays were ignored, as were effects due to refraction at the CCDs cover-glass. Therefore variables such as index of refraction and reflectivity are not included in this equation.

Testing the model for optical Söller collimator

Measurements were taken by placing a collimator with a particular aspect ratio over the image sensor and capturing an image. Exposure time was set such that the peak intensity in the brightest image (i.e. the image captured for the thinnest collimator sample) was just below the saturation point of the sensor. This resulted in an exposure time of 0.03 s, which was used for all subsequent exposures.

Light distribution profile

Light distribution profile measurements were compared with theoretical predictions of the light intensity profiles (Figure 10 B), as well as maximum intensity (Figure 10 A), and it was determined that to the first order there was good agreement. There were some discrepancies at higher aspect ratios of 16 and 24 (Figure 10 B, curves 5 and 6) which are likely due to second order effects, such as internal reflection (the plate material was not a perfect absorber) and the assumption of a uniform intensity for the illumination source. As described by Fresnel’s laws of reflection, the reflectivity of a surface approaches one as the angle of light incidence approaches ninety degrees. That is, a glancing ray nearly parallel to the reflecting surface will be almost totally reflected, even by a material which is highly absorptive at normal incidence. For small aspect ratio collimators these glancing rays should be an insignificant portion of the total light collected, whereas for large aspect ratios they would be less negligible.

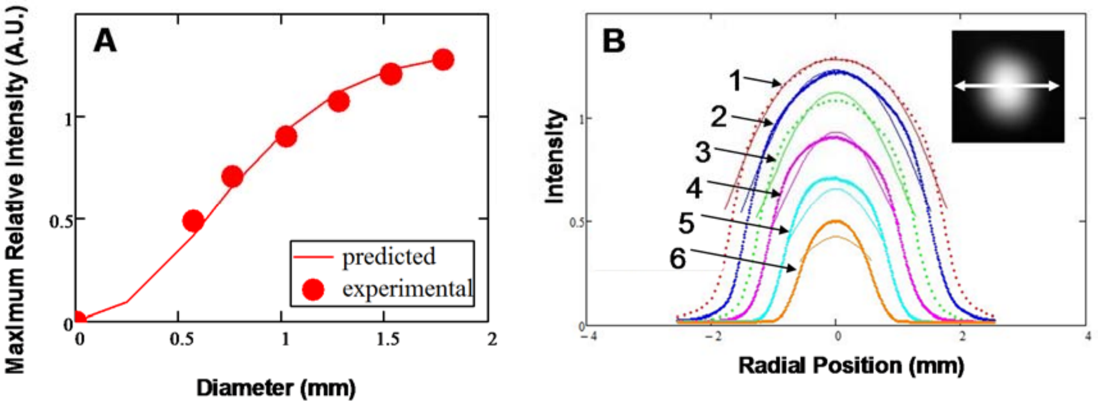

Figure 10 - Model Validation for simplified collimator test case - A) Test results from six collimators with identical aspect ratios (L/d) of various diameters (d) and thickness (L). The developed model agrees, with an R^2 value of 0.98. B) Transmitted intensity profiles numbered 1-6 corresponding to aspect ratios of 7, 8, 10, 12, 16, and 24, respectively. Solid thicker lines are measured data, thin/dotted lines are modeling results. Inset shows a single spot recorded from a typical SÖller collimator and where the profile is measured from (arrow).

Light intensity profile

Measurements of the light intensity can be seen in Figure 11 for different aspect ratios for a hole diameter of 2.54 mm. As aspect ratio is increased it can be seen in the 3D intensity plots B, C, and D that the slope of the profile increases (i.e. the profile shifts from conical to cylindrical as aspect ratio increases), corresponding to an increased degree of collimation. Figure 11 A provides a visual representation of these collimator geometries. In Figure 11-D details can be seen around the perimeter of the collimator hole which are irregularities caused by the laser machining process. These features can be resolved at higher aspect ratio because of the higher degree of collimation in the light. At lower aspect ratios, though the same defects are still present, they cannot be resolved. Another effect of increased aspect ratio is demonstrated in Figure 11 E/F: as aspect ratio is increased, transmitted intensity decreases.

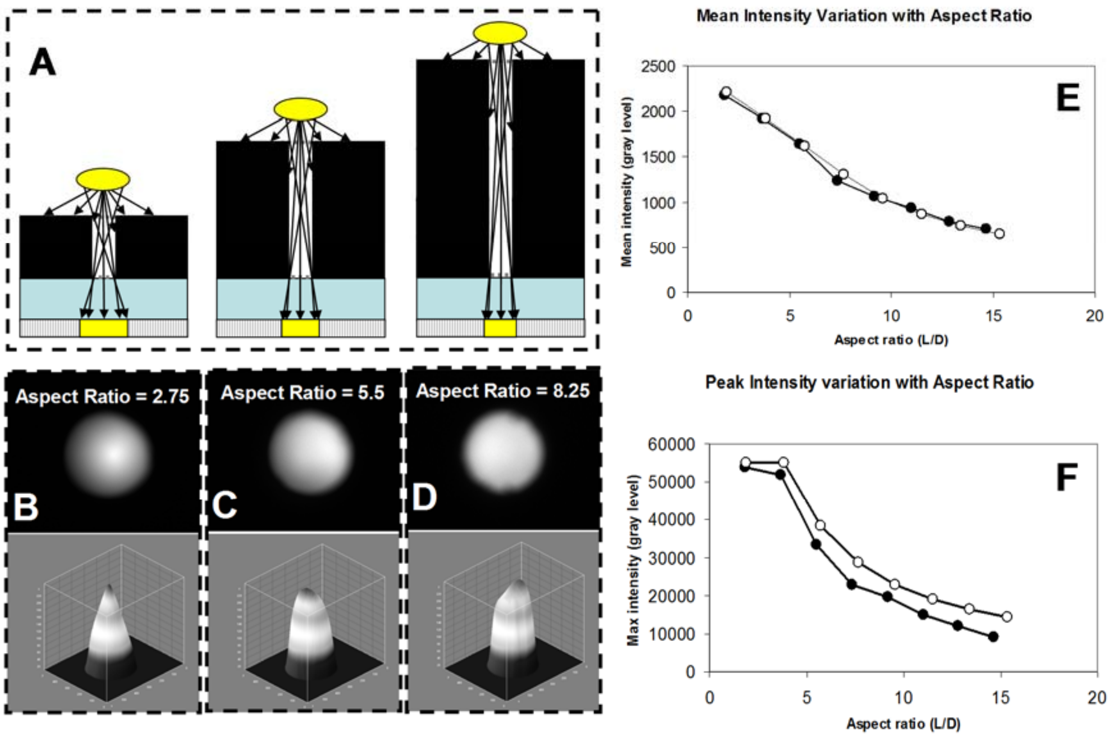

Figure 11 - Agreement between modeled and measured data - Schematic of the collimators analyzed in B, C, and D, demonstrating the absorption of diverging rays at higher aspect ratios. Images B, C, and D show light throughput of various aspect ratios for a given hole diameter and corresponding 3D intensity profiles (intensity profiles not to scale). E) Mean light intensity transmitted through Sӧller collimators of various aspect ratios. Measured and modeled data represented by solid and open circles, respectively. F) Similar to plot (E) but representing peak maximum intensity transmitted.

Predictive values of the model

To better understand the accuracy of the theoretical analysis and the parametric effects of the optical Söller collimator design, the measured maximum and mean light intensities were compared with the theoretical predictions in Figure 11 E/F. Mean light intensity was calculated over the area of each imaged spot. Area was measured in ImageJ by using a circular approximation for each spot. Maximum intensity is simply the highest pixel value recorded in each image. It can be seen that there is excellent agreement between the variation of the mean (R^2=0.990) and maximum (R^2=0.938) light intensities with aspect ratios. Points of agreement include the plateau effect in the maximum intensity at lower aspect ratios due to the finite size of the illumination source, as well as the asymptotic behavior at aspect ratios above 10 where the collimation begins to approach the ideal case and the light intensity is reduced by approximately 80%. It can also be noted that the primary aspect ratio effects are independent of the hole diameter. Therefore the aspect ratio becomes the critical design parameter for determining the appropriate geometry of plates to collimate light and the resulting light intensity for detection.

Regarding light intensity, many biosensing applications deal with extremely low light levels and in some cases involve photon counting. A primary principle of the Söller collimator is the purposeful rejection of a large percentage of this light. To compensate for this, long exposure times are used and background noise must be well controlled. This is a classical three-way tradeoff between cost, performance, and time. To deliver good results quickly a conventional plate reader can be used, which is costly. To deliver good results at low cost, a Söller collimator can be used at the cost of longer sampling time.

4. Image stacking approach to increase sensitivity of fluorescence detection

Many low cost consumer image sensors such as webcams and cell phone cameras are distributed with hardware that limits the maximum exposure time of the device to a range of standard video frame rates (e.g. 10-60 fps). Many fluorescence detection applications rely on a devices ability to detect low numbers of photons. In these cases, extended integration times are often required (as illustrated in the previous section). One approach, described here, to simulating extended exposure times in low cost consumer electronics for biodetection is a principle known commonly as image stacking. This technique relies on the use multiple captured images combined with time-domain signal averaging for image SNR enhancement. In the astronomy community this technique is used to combine many long exposure images. In the presented approach, hundreds or thousands of video frames are used to simulate such long exposures. While video mode is widely used for dynamic scene imaging, the use of image stacking on multiple video captured images was not reported previously for bio-detection.

4.1 Materials and methods

Fundamental principles

A digital image consists of large number of pixels, and for color CCD and CMOS, each image pixel contains three channels (red, blue and green). In video mode, many images (e.g. 30 frames per second) are captured from the camera. Using basic image processing software it is possible to calculate the average value of each pixel for a series of video frames in order to generate an averaged single image. Each pixel in an individual frame contains a combination of signal and various types of noise. By averaging large numbers of individual frames the random noise present in each frame approaches a constant value which can easily be subtracted after image stacking, while the signal present in all frames will be preserved. Thus, image stacking enables the removal of random sources of noise from a series of video images, creating a clear single static image with a significantly improved SNR.

Hardware

A platform similar to that used for the Söller collimator fluorescence experiments was implemented to benchmark the webcam detector. The CCD detector used previously was also employed to serve as a reference point. For the sake of simplicity, a fluorescent dye (fluorescein) alone was detected at varying concentrations in deionized water in order to determine relative limits of detection between the webcam, CCD and a commercial plate reader. Images for both imaging platforms (single frame for CCD and video file for Webcam) were captured using software supplied by the manufacturer: CamApp v. 1.0.0.9 (Aveo Corp., 2008), and AutoStar Envisage v. 7.03 (Meade Instruments Corp., 2007). The CMOS and CCD image intensities were analyzed using ImageJ software.

Image capture and processing guidelines

The incoming video stream from the webcam was modified using a software-based video processing amplifier built into the CamApp software. Most webcams and camera phones have hardware and software level adjustments which can be made by the user through an interface such as this. Typical adjustments include brightness, contrast, gamma, gain, and exposure time (or frame rate).

A brightness adjustment is used to apply a uniform shift to the luminance values of all pixels causing a uniform (i.e. scalar) increase in measured luminance. The brightness setting should be chosen such that no pixels are recorded as having a luminance value of zero. Because all pixels are generating a signal (due either to photons or to on-chip sources of noise), if any pixels in the image are recorded as having zero signal it means that signal is being discarded. This defeats the mechanism that allows image stacking to be successful, described in detail in the following section.

Contrast adjustments apply a linear stretch to the luminance of each pixel. This adjustment is a function of the pixel luminance value: the luminance of darker pixels is increased slightly, while the luminance of the brighter pixels is increased more. High contrast settings can limit the dynamic range of the sensor. This should be set to its default value. Contrast can be increased in low dynamic range imaging situations to improve on-screen visualization, but actual SNR is not affected.

Gain settings should be adjusted such that pixel value is increased by at least one ADU (analog to digital unit) for every photo-electron collected (unity gain). The experimental determination of this gain setting is described more completely in section 7.2. If gain cannot be adjusted on a particular device and its native setting is significantly less than one pixel unit per photo-electron, that device is likely not be suitable for low intensity fluorescence measurements.

Images from the webcam were captured using two methods: single frame and video. Single frame capture is identical to the operation of a conventional camera. Exposure time for this webcam was governed by an onboard controller, and had a lower limit of 1/30 s (dictated by frame rate, and typical of inexpensive units). In video mode a stream of frames was captured for ~10-30 seconds and saved as an AVI file. At thirty frames per second, this amounts to several hundred frames. The constituent frames of the video were then averaged together using ImageJ in 32-bit float format to produce a single image.

In both the single frame case and the video mode case one image (or video) is obtained with the excitation light turned on and the sample in place (a light frame). The excitation source is then turned off and another frame is captured using identical capture parameters (a dark frame). The dark frame records any background noise from the sensor (predominantly read/bias noise). The dark frame is subtracted from the light frame to remove this background signal. The degree to which the average noise in the dark frame is an accurate representation of the actual noise present in the light frame dictates how successfully this method can be applied (detailed in the following section).

4.2 Results and discussion

To measure the effectiveness of image stacking to improve CMOS measurement sensitivity, a thirty-six well plate was loaded with six concentrations of fluorescein each in six replicas. The plate was illuminated by a blue LED equipped with a blue excitation filter, and the plate was measured with a green emission filter. The signals of the wells were detected by the CMOS webcam operating in single frame mode and equipped with the original lens (f/3.8, focal length 5 mm) (Figure 12 A-B, LOD 1000 nM) and a CCTV lens (f/1.2, focal length 12 mm) (Figure 12 C-D, LOD 500 nM). The same CCTV lens was used on the CCD camera (Figure 12 E-F, LOD 30 nM). LODs for enhanced video mode images captured with the original f/3.8 lens (Figure 13 B-C) and the f/1.2 lens (Figure 13 D-E) were 60 nM and 30 nM, respectively. The LOD measured for the same samples by a fluorescent plate reader was also 30 nM. These results indicate a LOD improvement for this model fluorescent detection case of approximately 15X when this method of image stacking is employed. These results are consistent with a model developed in the following section.

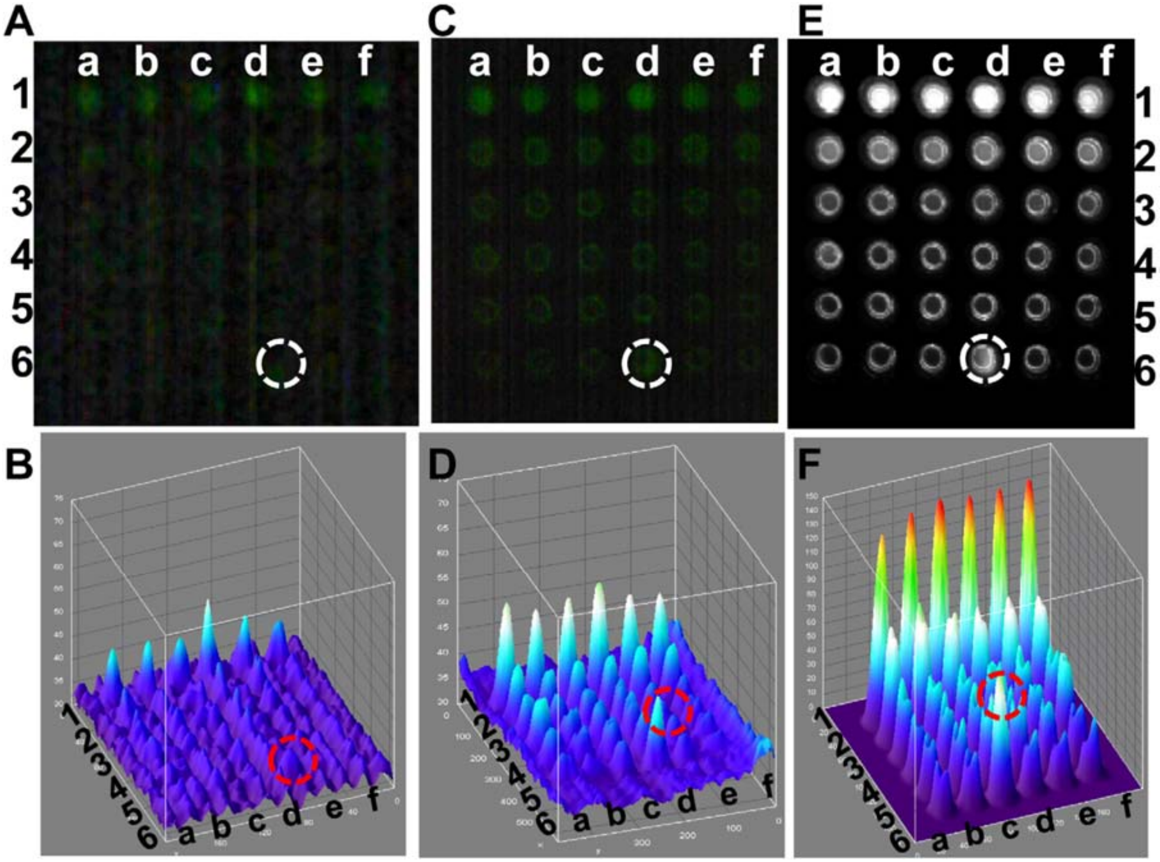

Figure 12 - Fluorescent LOD prior to image stacking - A thirty six well plate was loaded with six concentrations of fluorescein (rows 1–6) each in six replicas (columns a–f). (A) Detection *via* webcam equipped with its original f/3.8 mm lens, with (B) corresponding 3D plot. (C) Detection *via* webcam equipped

with f/1.2 CCTV lens, with (D) corresponding 3D plot. (E) Detection *via* CCD equipped with f/1.2 CCTV lens, with (F) corresponding 3D plot. LOD for cases A, C and E were 1000, 500 and 30 nM, respectively. The fluorescein concentrations used: row #1: 1000 nM, row #2: 500 nM, row#3: 250 nM, row #4: 60 nM, row #5: 30 nM and row #6: control (water). Row 6 column d (marked with a circle) is a reference point which was used to orient the plate.

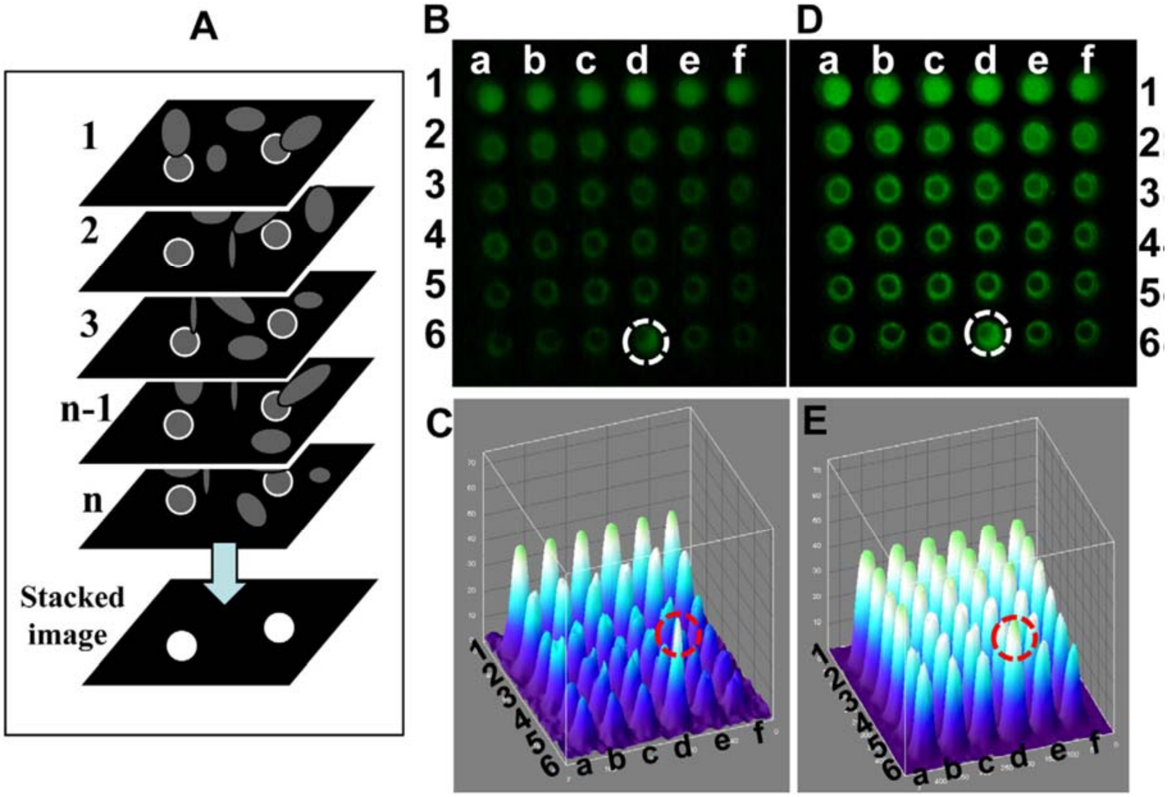

Figure 13 - Image stacking of webcam video captured images. A schematic of image stacking for enhanced imaging is shown in (A): the webcam in video mode captures n individual frames. Each frame contains signal of interest (marked with white circle) and noise (gray). (B) Dilutions of fluorescein (rows 1–6) each in six replicas (columns a–f) measured with the stock webcam lens and processed with image stacking (1000 video frames, LOD 60 nM), along with (C) the corresponding 3D representation of the data. (D) The same dilutions imaged with a 12mm f/1.2 lens (1000 frames, LOD 30 nM), with corresponding 3D plot in (E). The fluorescein concentrations used were: row #1: 500 nM, row #2: 250 nM, row#3: 125 nM, row #4: 60 nM, row #5: 30 nM and row #6: control (water). Row 5 column d (marked with a circle) is a reference point which was used to orient the plate.

Fundamental mechanism of image stacking improvement

Extended exposure times can be simulated by averaging many individual short exposures because of two fundamental concepts: the chaotic nature of photon arrivals, and pixel quantization error. The number of photons that arrive at a particular pixel in a given amount of time follows a Poisson distribution. That is, it has an average or expected value (λ), and a statistical variance which is also equal to λ. Because photons are quantized into discrete packets, the number of photons detected by a pixel must be an integer value. However the rate of photon arrival can be continuous (e.g. 1.2 photons per second).

The following illustrates the effects of pixel quantization error. Consider a pixel receiving photons at a rate of 1 photon per second with an exposure time of 0.25 second (i.e. an expected value of 0.25 photons per exposure). The probability this pixel will receive a certain number of photons during each exposure is plotted in Figure 14. The probability of recording zero photons is 78%. The probability of recording one, two or three photons is 19%, 2.4% and 0.2%, respectively. This is an example of a continuous variable (photon arrival rate) being quantized. In this case, none of the possible quantized states (0, 1, 2… photons per exposure) is an accurate representation of the true arrival rate because the true value lies between two quantized states (hence quantization *error*).

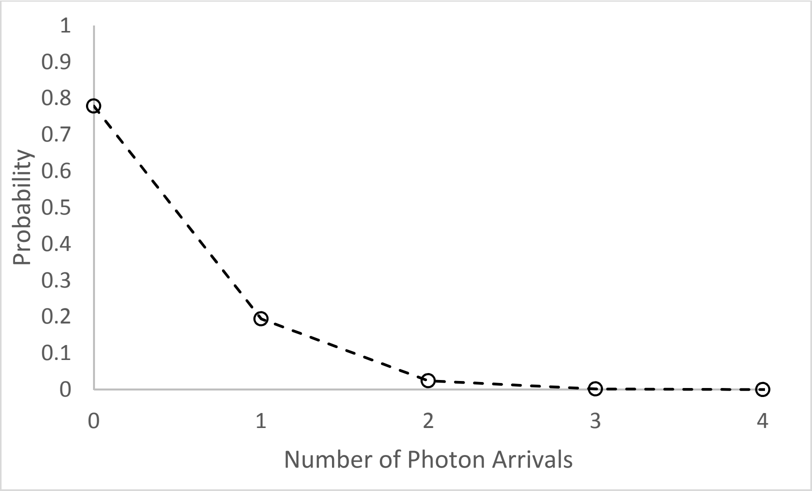

Figure 14 - Probability of photon arrivals – For an exposure time of 0.25 second and an average photon arrival rate of 1 photon/second, the probability of receiving a certain number of photons during a single exposure is plotted.

When time domain signal averaging is used on large numbers of images it is possible to extract a more accurate measurement of the true value from a large number of measured values containing quantization error. However in order for this to be effective, the bit depth of the average value must be greater than the bit depth of the original image. For example, the 8-bit images which webcams and cell phone cameras produce have 256 quantized intensity levels that each pixel can have; fractional states (i.e. decimal values) are not permitted. Using the pixel from the previous example, averaging thousands of measurements of this pixel would produce an average value very close to 0.25 photons (the true value). If this averaging was carried out at the native 8-bit pixel depth, the result would be rounded to the nearest quantized state: zero. A higher bit depth (such as 32-bit float format) must be used to preserve the true fractional value.

The basic mechanism behind improved detection limit with time domain averaging is the ability to measure photon arrival rates that are below the sensor noise cutoff level for a given sensor. Sensor noise is a combination of read noise, thermal signal, quantization noise, and noise due to pixel response non-uniformity (PRNU, i.e. fixed pattern noise). For the purposes of this analysis, the sensor noise cutoff is defined as the level below which a pixel value is indistinguishable from noise at the 99.9997% confidence level (i.e. 4.5 σ). This confidence level was selected such that it is unlikely for a single pixel on a typical small format digital sensor (i.e. <1 million pixels) to be above this limit. For a region of pixels containing intrinsic sensor noise with an average value of μ_0 and standard deviation of σ_0, this cutoff pixel value (μ_c) is equal to

$$\mu_c = \mu_0 + 4.5\sigma_0$$

When n image frames are averaged together, the standard deviation of the intrinsic noise and photon noise in the resultant image is decreased by a factor of $\frac{1}{\sqrt{n}}$, yielding

$$\mu_c = \mu_0 + \frac{4.5\sigma_0}{\sqrt{n}}$$

In practice, the DC offset caused by the average noise level μ_0 is subtracted by subtracting an average background dark frame from each signal frame. In a biosensing application, where a control sample is being measured to establish background noise level there will be an additional source of noise from photons in this region (μ_p), and the previous equation takes the form

$$\mu_{cp} = \mu_0 + \frac{4.5\sqrt{\sigma_0^2 + \mu_p}}{\sqrt{n}}$$

The relationship between number of averaged frames and the sensor noise cutoff μ_c is plotted in Figure 15 (black dashed line). This plot is for a sensor with an intrinsic noise level σ_0 equal to the signal from 7 photo-electrons. Measured data from a sensor with this same noise level is also plotted (circles). Red and blue dashed lines are plotted to show the number of frames required to decrease the noise cutoff from 10 photo-electrons per exposure to 1 photo-electron per exposure. This plot demonstrates one of the practical limitations to image stacking. It can be seen that the model and data agree fairly well until approximately 750 to 1000 frames are averaged. Beyond this, there are decreasing returns from averaging an increasing number of image frames. This is due to sensor drift which occurs during the image collection process and during the process of collecting the dark frames which were pre-subtracted. Use of a thermally stabilized camera (i.e. one that uses a regulated thermo-electric cooling device) can move this point of limiting returns out farther along the horizontal axis.

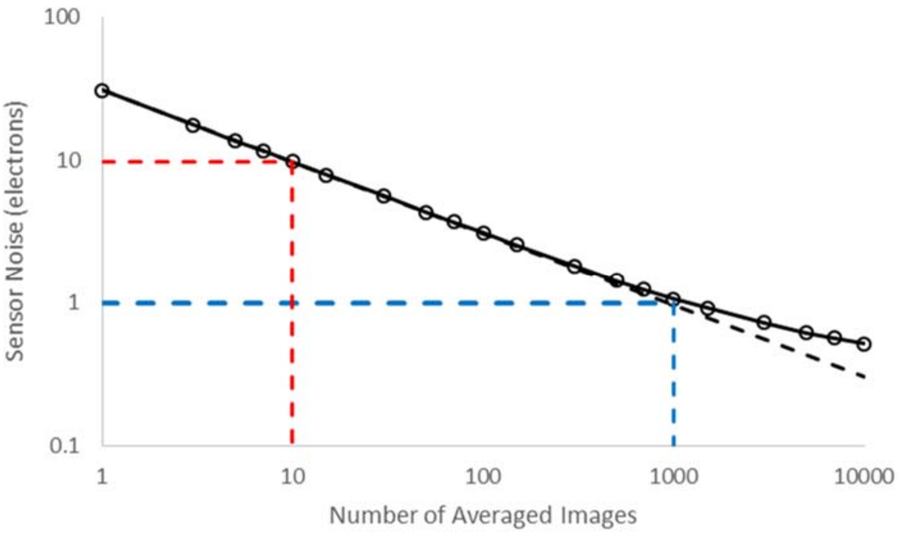

Figure 15 - Relationship between sensor noise cutoff, pixel SNR and number of averaged video frames – For a sensor with an average read noise of ~7 electrons, the relationship between number of averaged frames and sensor noise cutoff is shown (heavy black dashed line, μ_C), along with collected data showing the eventual deviation of measured values from this model (circles). Based on these two trends, the SNR of pixel regions with an average photon arrival rate of 100, 10, and 1 photons per exposure time are plotted against number of averaged frames (dashed lines show ideal SNR, solid lines show realistically obtainable SNR). A point of limiting returns can be seen beginning at around 1000 averaged frames in this example. The actual location of this point depends on sensor thermal stability. A horizontal line representing an SNR of 4.5 is plotted to show the relative number of frames each pixel region would require to reach this SNR (red dashed line).

5. Capillary array waveguide amplified fluorescence detector

mHealth analytical technologies have the potential to overcome the limitations of using current medical diagnostics in resource-poor settings. Effective mHealth devices for underserved populations need to be simple, low cost, and portable. For example, mobile phones equipped with cameras which have become ubiquitous in resource-poor settings have potential for use in mHealth optical detectors. However, the sensitivity of a mobile phone camera is currently too low to be effective for many of the diagnostic applications which depend on detection of weak fluorescent signals.

To improve the sensitivity of portable phones, a technique was developed for improving LOD of liquid-phase fluorescent assays by improving efficiency of excitation and collection of emitted photons via use of capillary waveguides. Based on this technique, a proof-of-concept mHealth platform was developed based on a mobile phone camera as a detector. Sensitivity near that of conventional methods was demonstrated using 10X smaller sample volumes.

5.1 Materials and methods

The main challenge of using a mobile phone for low light fluorescence detection in mHealth applications is the low sensitivity of the phone camera. Waveguiding capillaries were used in this work for evanescent excitation to increase sensitivity. The basic configuration of the fluorescence capillary array detectors as shown schematically in Figure 16-1 are: (A) a fluorescence excitation source, (B) excitation filter, (C) sample holder array, (D) emission filter, (E) objective lens, and (F) optical sensor. A photograph of the configuration is shown in Figure 16-2 where either a cell phone camera or a CCD camera is used as the optical sensor, the system includes a computer to acquire and analyze images. In this optical configuration (Figure 16-1) the excitation source is directly in line with the image sensor, so good quality excitation and emission filters are essential for blocking any excitation light reaching the detector, while still allowing the fluorescence emission to be transmitted.

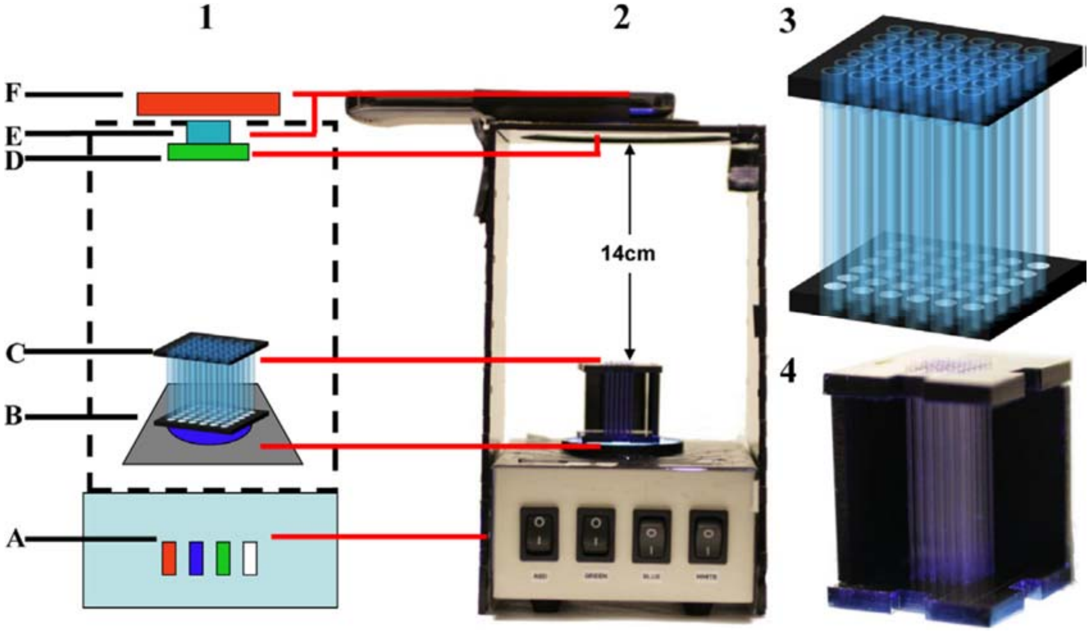

Figure 16 - mHealth capillary array fluorescence detectors - (1) A schematic configuration of the mHealth capillary array fluorescence detectors with the main system components highlighted in the schematic: [A] a portable phone or digital camera mounted in a homemade acrylic box, [B] lens [C] emission filter mounted on the end of the lens [D] capillary array, [E] excitation filter and multi-wavelength LED. (2) A photo of a portable phone-based fluorescence detector. A schematic image of capillary array is shown in (3) and a photo of the array is shown in (4).

To characterize the sensitivity of the mobile phone detector for mHealth, we used a Samsung Galaxy SII smartphone and a Meade astronomical 16-bit uncooled CCD from our previous work[135,136]. The lens used for the CCD camera is an f/1.2 Tamron manual 4-12 mm CCTV. The built in lens for the mobile phone (Figure 16-1-C) has a focal ratio of f/2.65 and a 4 mm focal length.

One challenge in using the mobile phone camera is the limited control on the light exposure. In the phone's built-in camera application, the exposure time is automatically set based on the image brightness. This is not ideal for scientific measurement applications because it makes quantitative comparison of multiple images difficult. To overcome this problem, an aftermarket application was used which allows the user to control the exposure time of the camera (Camera FV-5, Flavio González Vázquez). The range of control is dictated by the hardware of the image sensor, and the maximum exposure length is 1/15 s for the Galaxy SII phone.

A previously developed LED illumination module[90] was used for fluorophore excitation (Figure 16-1-A). It is comprised of a multi-wavelength LED illumination box and an excitation filter (Figure 16-1-B). The multi-wavelength LED illumination box is equipped with both white and RBG LEDs capable of exciting multiple fluorophores over a wide excitation spectrum of 450-650 nm. The fluorescein example has a peak excitation wavelength of 494 nm and an emission maximum of 521 nm. The excitation filter used for fluorescein is a 20 nm passband filter with 486 nm center wavelength, and for emission (Figure 16-1-D) a 50nm passband filter with center wavelength of 535 nm. To demonstrate the capability of this new technique, fluorescein was used as a model fluorescence media. Results were compared with a benchmark diagnostic system that we developed previously[103,115].

5.2 Results and discussion

Capillary array amplification of fluorescence signal

To study the effect of the capillary array on cell phone camera fluorescence detection, the signal from the capillary array was compared to the signal measrured from a plate assay. In both configurations the same volume (8.5 μL) was used. Both configurations were imaged by both a cell phone camera and CCD camera.

Serial dilutions of fluorescein in the range of 0–3320 ng/ml (0–10,000 nM) were analyzed using a ten-fold serial dilution (0.001 nM, 0.01 nM, 0.1 nM, 1 nM, 10 nM, 100 nM, etc.). Exposure time for the cell phone camera was set to 1/15 s and the camera gain was set to its maximum (800 ISO). Figure 17 (1) shows the emission image of six concentrations (column A–F in Figure 17 (1) and (3)) of fluorescein loaded via micropipette into the 36 capillary array compare to a 36 well plate array (Figure 17 (3)) in six replicas (rows1–6) recorded with the cell phone camera.

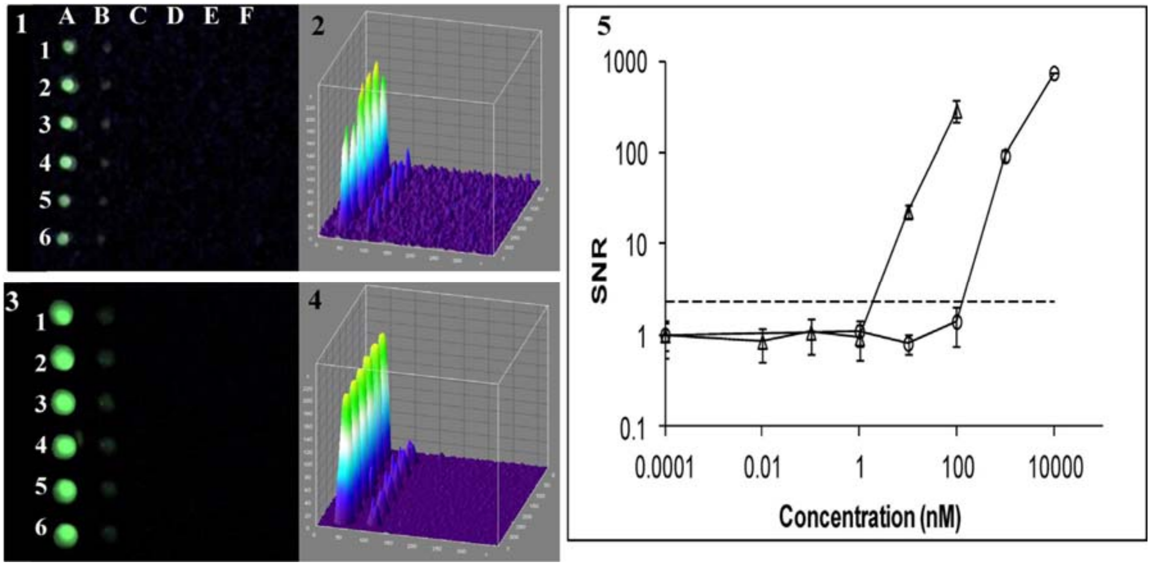

Figure 17 - Capillary array fluorescence amplification - Portable phone image of (1) the 36 capillary array loaded with 6 replicas (columns) of 6 different fluorescein concentrations (rows). (2) The corresponding ImageJ 3D image of (1). (3) Image of the 36 well plate array. (4) The corresponding ImageJ 3D image of (3). (5) Signal intensities from the image were quantified using ImageJ and the dose response curve was plotted on a log-log plot, triangles for the capillary array and circles for the well plate array. The assay units are signal to noise ratio (SNR), with each measured value divided by control (concentration 0 ng/ml). The error bars are equal to one standard deviation (n = 6). The fluorescein concentrations, from left (column A) to right (column F), are 0.01 nM, 0.1 nM, 1 nM, 10 nM, 100 nM and 10,000 nM. Each concentration was measured 6 times (rows 1–6). Limit of detection SNR is illustrated by a horizontal dashed line.

As shown in Figure 17 (5) the signal from the 36 well plates is lower than the signal image of the 36 capillaries array. The signal intensities from the images were quantified using ImageJ and the dose response curve was plotted. The signal-to-noise ratio (SNR) was calculated as the value measured divided by the control signal (concentration 0 ng/ml). Figure 17 (5) is a plot of the mean signal from each concentration of fluorescein as detected by the cell phone camera in both the capillary array and the plate array which suggest that capillary signals are ~100X higher than the plate signals for the same volume of fluorescein. Variation in the signals was found to be less than 5% for a given concentration.

Borosilicate glass is well known to autofluoresce when exposed to blue light. Therefore, a similar experiment was carried out using an Alexa Flor dye with an excitation peak at 654 nm and an emission peak at 674 nm. In this wavelength range, borosilicate does not strongly autofluorescent. As in the fluorescein case, LOD was improved by approximately 100×. In this case, the LOD was not dictated by the autofluorescence of the glass, but instead by the extinction coefficient between the two filters used.

To compare the level of detection of the phone to the level of detection of a CCD camera, the same concentrations of fluorescein were analyzed by an uncooled consumer grade CCD camera. A capillary array (Figure 18 (1)) and well plate array (Figure 18 (3)) were measured. It can be seen that the same amplification effect is measured with the CCD camera, with a similar amplification level of ~100x. Statistical analysis shows that the LOD, based on three standard deviations of the mean signal for water, is approximately 10 nM for the cell phone camera when using the capillary array and approximately 1000 nM when using the well-plate array. The CCD camera showed a LOD of 0.1 nM with the capillary array and 10 nM with the well-plate array. So while the CCD camera demonstrates a 100X better LOD than the cell phone camera, the capillary array increased the cell phone camera sensitivity 100x to achieve the same LOD as the CCD camera when interrogating a plate array.

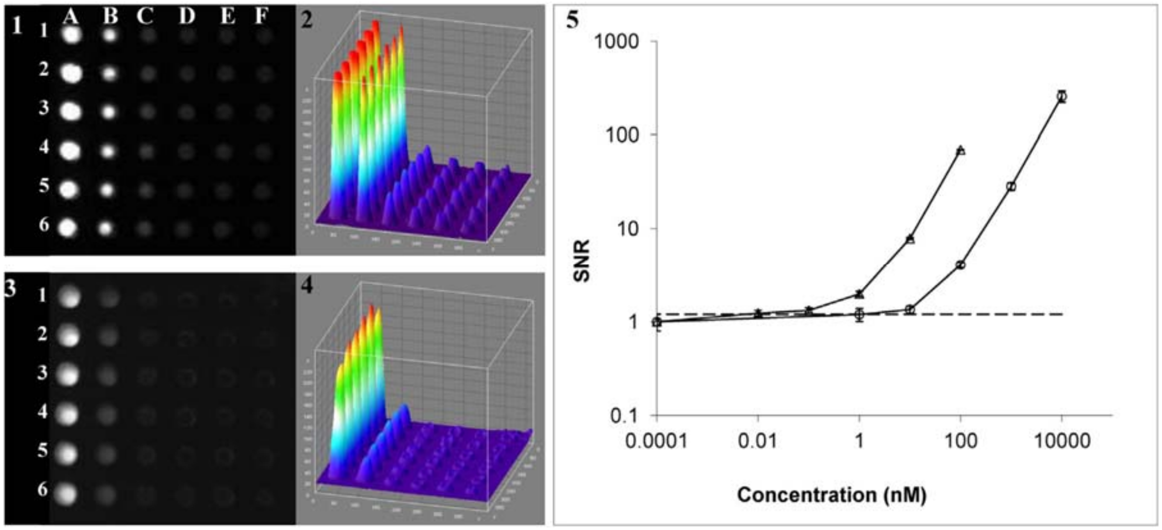

Figure 18 - CCD camera detection of waveguide capillary array fluorescence - CCD camera image of (1) the 36 capillary array loaded with 6 replicas (columns) of 6 different fluorescein concentrations (rows). (2) The corresponding ImageJ 3D image of (1). (3) CCD image of the 36 well plate array. (4) The corresponding ImageJ 3D image of (3). (5) Signal intensities from the image were quantified using ImageJ and the dose response curve was plotted, triangles for capillary array signal measurements and the circles for plate array measurements. The assay units are signal to noise ratio (SNR), with each measured value divided by control (concentration 0 ng/ml). The error bars are equal to one standard deviation (n = 6). The fluorescein concentrations, from left (column A) to right (column F), are 0.01 nM, 0.1 nM, 1 nM, 10 nM, 100 nM and 10,000 nM. Each concentration was measured 6 times (rows 1–6). Limit of detection SNR is illustrated by a horizontal dashed line.

The mechanism of waveguide amplification of fluorescence signal

The proposed mechanism for the signal amplification is fourfold. First, the light-wave energy propagating through the capillary walls can interact directly with and excite the fluorescein molecules near the walls via evanescent waves. Second, some of the emitted fluorescent light which is emitted under the right conditions will be guided by the capillary walls and will be more effectively directed at the detector. Third, the higher aspect ratio of the capillaries gives those photons traveling directly through the core of the capillary more opportunities to interact with a fluorophore. Finally, the emitted light from the fluorescent sample is imaged onto a fewer number of pixels in the case of a capillary, resulting in higher pixel SNR compared to images of a well where photons are spread out over more pixels. The third and fourth effects are strictly geometric and could be taken advantage of in a well plate with very deep wells. Additional modeling of evanescent wave signal amplification is presented in chapter 6.

To compare the relative effects of the waveguide portions of amplification and the geometric portions, two different sets of capillary tubes were used: one set was uncoated glass which could act as a waveguide (Figure 19 (1)), and one set was coated on all of its external surfaces with high-purity silver which interferes with total internal reflection and prevents the capillary from acting as a waveguide (Figure 19 (2)). The silver coating prevents waveguiding in two ways: first, by blocking light from being coupled into the ends of the waveguide by the excitation source, and second by frustrating any possible total internal reflection and thus blocking waveguide propagation. The array was illuminated by the LED illumination module equipped with a blue excitation filter, and the array was analyzed with a green emission filter as previously described. Both capillaries were loaded with four concentrations of fluorescein (Figure 19 (3), rows 1–4) each in three replicas (columns A–F) and the florescent signal of silver coated capillaries (Figure 19 (3), columns A, C and E) was compared to the signal of uncoated capillaries capable of waveguide propagation (Figure 19 (3) columns B, D and F). The signals of the capillaries were detected by the CCD camera equipped with an f/1.2 Tamron manual 4–12 mm CCTV lens and the corresponding ImageJ 3D image is shown in Figure 19 (4). Very weak signal from the highest fluorescein concentrations (100 nM) was measured in silver coated capillaries A-1, C-1 and E-1 (marked with circles) in comparison to the signal of capillaries without coating (B-1, D-1 and F-1) capable of detection at lower fluorescein concentrations (row #2: 10 nM, row #3: 1 nM, row #4: 0.1 nM). The data suggest that signal can be detected with the uncoated capillaries (columns B, D and F) down to a concentration of 0.1 nM, while no signal was statistically detectable in the coated capillaries below 10 nM (column A, C and F). This 100X difference indicates that the proposed waveguiding nature of the capillaries are predominantly responsible for the amplification seen.

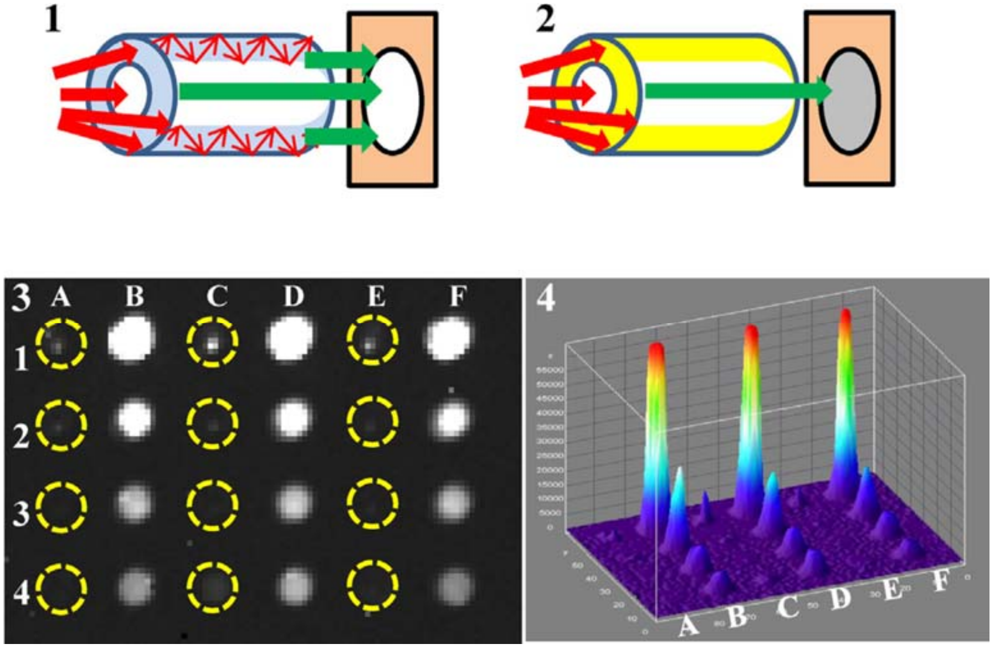

Figure 19 - Waveguide fluorescence capillary array amplification - Schematics of capillary with waveguide propagation through the capillary wall (1) and schematics of capillary with waveguide propagation blocked with silver coating. (2); an image with the actual capillaries (3) showing 6 × 4 array with 3 silver coated capillaries (column A, C and E) and uncoated capillaries (column B, D and F) loaded with four concentrations of fluorescein (rows 1–4), each in three replicas. The array was illuminated by a

blue LED equipped with a blue excitation filter, and the array was analyzed with a green emission filter. The signals of the capillaries were detected by the CCD digital camera equipped with Tamron manual zoom CCTV 4–12 mm, f/1.2 lens. (6) The corresponding ImageJ 3D image of V. The fluorescein concentrations used: row #1: 100 nm, row #2: 10 nM, row #3: 1 nm, row #4 0.1 nM.

Thousand-fold fluorescent signal amplification for mHealth diagnostics

To increase the sensitivity of mHealth technologies, we combined the previously described capillary design with computational enhancement via image stacking to increase sensitivity for fluorescence detection. This combined approach has the potential to form the basis for mHealth technologies using optical detection assays requiring high sensitivity using low cost medical diagnostic techniques with clinical utility in resource-poor settings for global health. Two types of detectors were used in this work, a generic webcam color video camera (AVEO Corp) with an 8 bit 640 x 480 pixel CMOS sensor enabling 256 levels of gray scale (typical Ebay vendor) used in previous work[161] and Samsung Galaxy SII smart phone (Samsung Electronics Co.) with a built-in lens with a focal ratio of f/2.65 and a 4 mm focal length. The phone was used with an aftermarket application which allows control of the exposure time and gain of the camera (Camera FV-5, Flavio González Vázquez).

Combine detection modes utilizing computational image stacking and optical amplification to improve detection sensitivity

The computational image enhancement of images captured from a webcam video enables a 10X increase in sensitivity (see chapter 4), and the optical amplification using capillary tubes enables 100X increase in sensitivity (previously discussed in this chapter). Therefore, we combined both detection approaches using the webcam camera in video mode to image the capillary array, and then processed the images by image stacking.

In this experiment, ten-fold serial dilution (0 nM, 0.01 nM, 0.1 nM, 1 nM, 10 nM, 100 nM) of fluorescein in capillary array was analyzed by the webcam using single frame without stacking or with video mode followed by image stacking (Figure 20). Figure 20 shows a plot of the mean signal from each concentration of fluorescein in the capillary array as detected by the webcam camera single frame with LOD of 10 nM compared to the LOD of 1000 nM without the capillaries as previously reported. This 100X increase in sensitivity is similar to the 100X increase of LOD shown for the mobile phone detection (Figure 17). The use of the video mode followed by image stacking increased the sensitivity by another ~10X to a LOD of 1nM. This combination enabled a 1000X increase in sensitivity from 1000 nM to 1 nM.

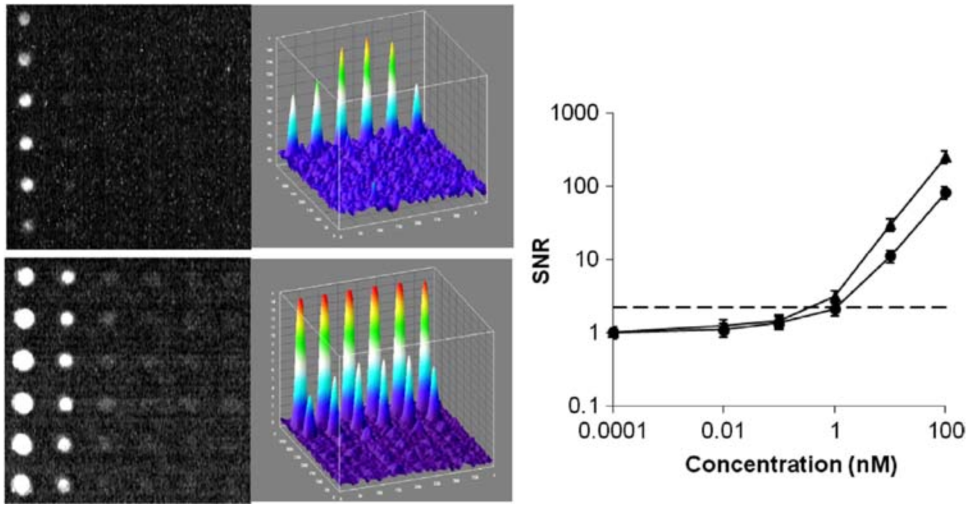

Figure 20 - Waveguide capillary array fluorescence amplification combined with computational image stacking - A thirty six capillary array was loaded with six concentrations of fluorescein (column 1-6) each in six replicas (rows A-F). The capillary array was analyzed by webcam operating in a still single frame mode (I). The corresponding ImageJ 3D image is shown in (II). The same capillary array was analyzed in video mode and the image was enhanced by image stacking, shown in (III) with the corresponding ImageJ 3D image in (IV). The signal-to-noise ratio (SNR) was plotted against the various fluorescein concentrations (V). Triangles are data points for video captured stacked images and circles are single image mode with no stacking. The LOD (the mean plus three times standard deviation of a control (water)) is marked as a dashed line. The fluorescein concentrations used were (columns #1-6): 100 nM, 10 nM, 1 nM, 0.1 nM, 0.01nM and control (water).

Extension to mobile phone platform

The computational image enhancement technique described previously was used to further increase the sensitivity of the capillary array device for mHealth fluorescence detection. As demonstrated previously, this technique resulted in a 10x improvement in LOD when used with a conventional CCD camera and a CMOS webcam. The same approach was used in an attempt to improve the LOD for a portable phone camera (Figure 21). The exposure time for the cell phone camera set to its maximum (1/15 s) and the camera gain was set to its maximum (800 ISO). With no stacking the LOD was 1000 nM for fluorescein, similar to the webcam results. However, image stacking did not improve the LOD, which was again 1000 nM. In fact, the plot shown in Figure 21 is of both curves: they are identical. Analysis of the image files suggest that the image processing native to the phone camera filters out weak signals by clamping the background signal level to zero at an arbitrary cutoff point, which renders computational approaches for weak signal enhancement useless. Therefore, optical amplification of the signals has to be used to increase the level of light intensity from a fluorescent sample to one that is high enough that the phone camera hardware will not reject it as noise.

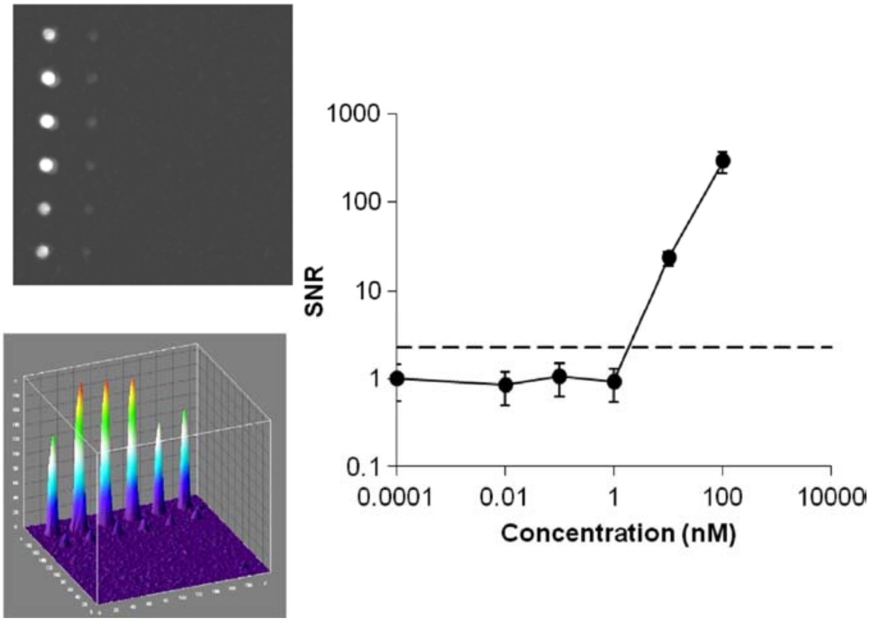

Figure 21 - Waveguide capillary array fluorescence amplification images captured with mobile phone - A thirty six capillary array was loaded with six concentrations of fluorescein (column 1-6) each in six replicas (rows A-F). The capillary array was analyzed by mobile phone operating in a still single frame mode (I). The corresponding ImageJ 3D image is shown in (II). The signal-to-noise ratio (SNR) was plotted against the various fluorescein concentrations (III). The fluorescein concentrations used were (columns #1-6): 100 nM, 10 nM, 1 nM, 0.1 nM, 0.01nM and control (water). The LOD is marked as a dashed line.

Dependence of amplification factor on pH

An interfering effect was noted when fluorescein dye was used in pH un-buffered solutions. Capillaries loaded with pH un-buffered dye solutions were noted to have amplification factors that were approximately 5X greater than those loaded with pH buffered solutions made using PBS. Because serial dilutions were carried out using 10-fold dilutions steps this effect was not typically noticed. A similar effect was measured in plate arrays but to a lesser degree (typical difference between buffered and un-buffered solutions was ~1.5-2X). Therefore the stated amplification factors (which compare the signal levels in plate arrays and capillary arrays) should be divided by a factor of 2.5-3.5 when considering experiments conducted in pH buffered solutions.

5.3 Orthographic projection capillary array fluorescence sensor

One issue with the capillary array is the uniformity of the fluorescent signal measurements when a compact optical system is used. Designing the optical configuration for detecting such capillary array sensors is a challenge which requires a system capable of uniformly detecting optical signals through long parallel capillaries tubes distributed in a large space. To image the capillary array, orthographic projection, which is capable of representing three dimensional objects in two dimensions, can be applied. Orthographic projection is a form of parallel projection of 3D objects with all the projection lines orthogonal to the projection plane, resulting in every plane of the captured image retaining straight lines and parallelism (an affine transformation) on the sensor. We describe here an orthographic projection sensor capable of uniform fluorescent measurements from capillary arrays.

Design of orthographic projection optics

To image the capillary array, orthographic projection optics using an object-space telecentric lens to represent the three dimensional array in two dimensions was used. The term “object-space telecentric” indicates that an object at any distance from the lens will appear the same size in the resultant image. The basic optical configuration of the telecentric optics is shown schematically in Figure 22 A. The principle elements are shown: a plano-convex lens (Figure 22 A-i) and the principal rays imaged by the lens of the phone camera (Figure 22 A-ii) focusing the image onto the camera’s sensor (Figure 22 A-iii). The capillary array (Figure 22 B) is imaged with the plano-convex lens (4.5 cm diameter, 15 cm focal length) in three different positions. As shown in Figure 22 C, at the ideal camera-to-lens distance where the focal points of the camera phone lens and the secondary lens are aligned, the object-space telecentric condition is achieved and a parallel projection of the 3D capillary array is seen in Figure 22 B. All of the projection lines (i.e. light rays imaged by the telecentric lens) from the 3D capillary array are orthogonal to the projection plane, resulting in every plane of the captured image retaining straight lines and parallelism on the sensor. In Figure 22 D, the image is taken with the secondary lens at a distance too far from the camera, and in Figure 22 E the distance is too close. Both configurations, D and E, result in images where the capillaries seem to converge or diverge towards the viewer. In a fluorescence measurement scenario, this results in the center capillaries appearing brighter than the peripheral capillaries. At the ideal camera-to-lens distance, the focal points of the camera lens (Figure 22 A-i) and the secondary lens (Figure 22 A-ii) are aligned. This is the simplest possible object-space telecentric setup.

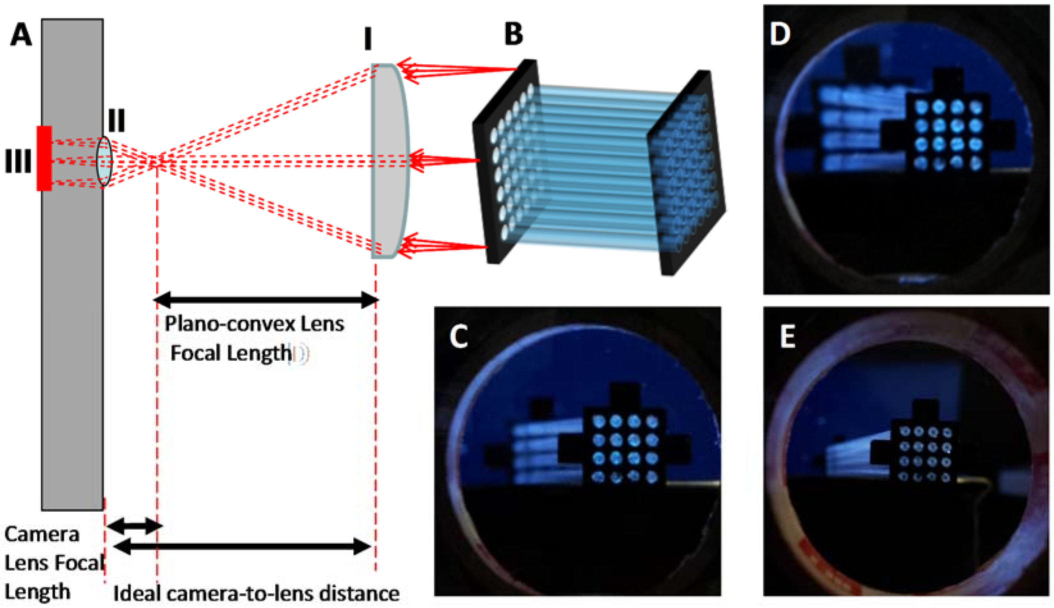

Figure 22 – Orthographic projection optics - (A) Schematic of the object-space telecentric optics with (I) the plano-convex lens and the principal rays imaged by (II) the lens of the phone camera which focuses the image onto (III) the camera sensor. (B) Schematic of the capillary array. The capillary array was imaged at three different camera-to-lens distances: C = 14.5 cm, D = 30cm and E = 5 cm. The object-space telecentric condition (C) is at the ideal camera-to-lens distance so that all capillaries of the arrays shown in (B) appear parallel, (D) position too far of a camera-to-lens distance, and (E) position at too close of a camera-to-lens distance.

The main elements of the orthographic projection fluorescent sensor are shown in Figure 22: a schematic of the camera phone fluorometer with the telecentric lens configuration (Figure 22 A), and a photo of the actual device (Figure 22 B). The main components are: (i) a camera phone, (ii) an emission filter, (iii) a secondary lens, (iv) an alignment fixture, (v) a capillary tube array, (vi) two spaced excitation filters, and (vii) a multi-wavelength LED light box. The system also includes a computer to acquire and analyze images. In Figure 22 A, d_f is the distance between the capillaries and the camera lens which can be minimized by proper secondary lens selection. In the configuration shown, d_f is 32 mm to achieve both focus and uniform capillary illumination. Without the secondary lens the minimum d_f is 65 mm to achieve focus, and approximately 140 mm to achieve uniform capillary measurements.

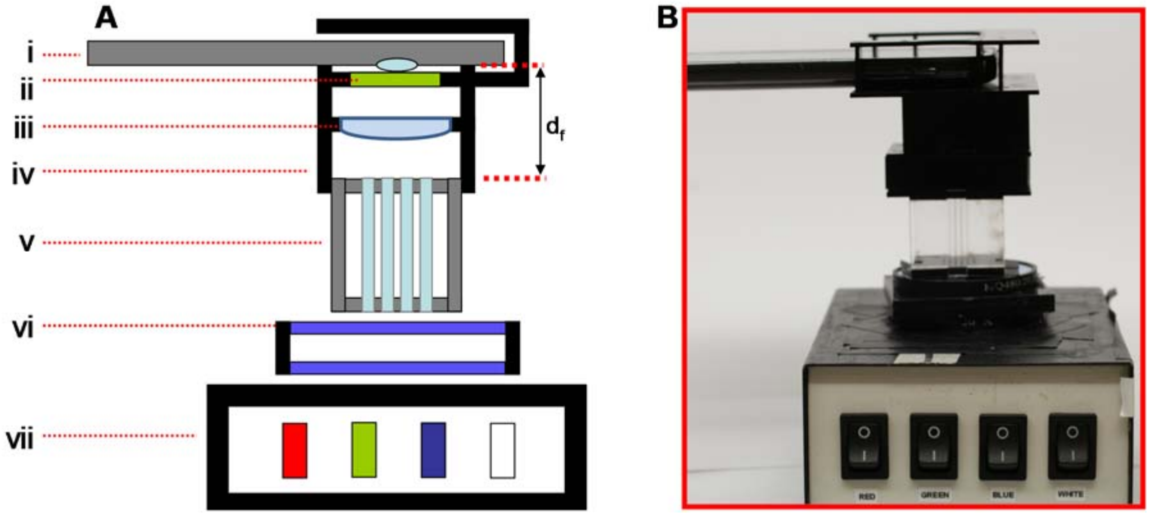

Figure 23 - Orthograpic projection optics - Orthographic projection fluorescent sensor for mHealth (A) a schematic configuration of the orthographic projection fluorescent sensor and (B) A photograph of the device. Constituent parts are: (i) camera phone, (ii) emission filter, (iii) plano-convex lens, (iv) alignment fixture, (v) capillary tube array, (vi) two spaced excitation filters, and (vii) multi-wavelength LED light box. df is the distance between the capillaries and the camera lens.

In the configuration shown in Figure 23, two excitation filters (Figure 23 A-vi) are used. This is because the excitation filters used are interference filters, and the light source is diffuse. The wavelength of light allowed to pass through this type of filter is highly dependent on the angle at which the light passes through the filter. In order to ensure the narrow excitation bandwidth necessary for the emission filter to block the excitation light, the angle of light passing through the filters must be constrained. One very simple method to effectively constrain this angle is to use two filters separated by some distance. The greater this distance, the more constrained the angle of light will be (in this case a distance of approximately 10 mm was found to be suitable). A more ideal solution is to use a light source which is collimated well enough that all of its light falls within the range of angles, allowing a single filter to be used. This corresponds to an angular divergence of approximately twenty degrees.

Light distribution using orthographic projection optics

To demonstrate the capability of the orthographic projection fluorescent sensor, fluorescein (a dye used commonly in many biological assays) was used as a model fluorescence media. A 3D graphical representation of the 2D light intensity distribution without the telecentric lens is shown in Figure 24 A. It can be seen that the light is not uniformly distributed across the space being imaged, especially toward the edges of the imaging field. There is a relative intensity difference of approximately 30-50% between the center of the field and the edges. The comparable distribution of the light obtained using the telecentric lens (Figure 24 D) is significantly more uniform. When imaging a 4x4 capillary array with standard lens configuration (Figure 24 B), there is significantly uneven florescence signal from the capillaries, as shown graphically in Figure 24 C, especially at the edges of the capillary array. In contrast the fluorescent emission is more uniform using the orthographic projection configuration (Figure 24 E), resulting in a much reduced edge effect for the fluorescent signal (Figure 24 F). These results clearly demonstrate the advantage of using orthographic projection optics in this case.

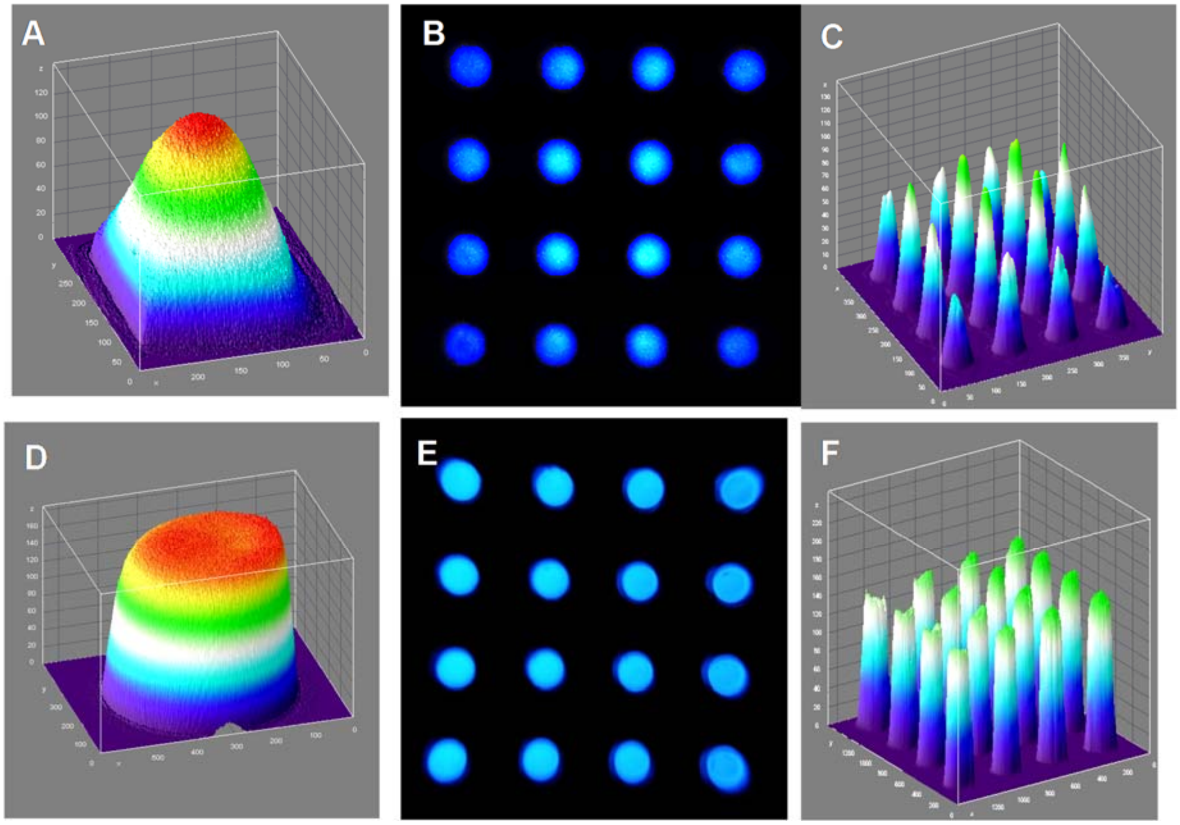

Figure 24 - Light distribution with orthographic projection optics - A sixteen capillary array was loaded with fluorescein (1 µM). The array was analyzed by the mobile phone using standard phone lens (A-C) or in orthographic projection optical configuration with a telecentric lens system (D-F). (A) A 3D visualization of a planar illumination source is shown as seen with the single lens system. (B) The light field seen by the single lens system when looking at an array of 16 capillary tubes, with (C) corresponding 3D visualization. (D, E, F) Corresponding results for the telecentric lens system are also shown, demonstrating a significantly more uniform illumination field.

Detection of Adenovirus using capillary device

Adenoviruses, linear dsDNA viruses, are the most common cause of respiratory illness. In addition, adenovirus is a cause of gastroenteritis, cystitis, conjunctivitis and rashes. We amplified adenovirus DNA with PCR and labeled it with SYBR green or fluorescein. The 167-bp amplicon was analyzed in several different ways, using either gel electrophoresis or fluorimetry with a plate reader, or fluorimetry with our capillary florescent detector.

As shown in Figure 25 A, adenovirus DNA stained with SYBR green was detected using gel electrophoresis at a concentration of 6 µg/mL and fluorescein-stained DNA was detected at a concentration of 1 µg/ml. The DNA stained with SYBR green or fluorescein was also analyzed by a plate reader and the capillary array. Figure 25 B shows these results for SYBR green. The LOD for the capillary array and plate reader were 5 µg/mL and 1 µg/mL, respectively. Similar results were obtained using DNA stained with fluorescein (Figure 25); the LOD of the capillary array was calculated to be 0.4 µg/mL and that of the plate reader calculated at 0.08 µg/mL. With both dyes, the plate reader had a limit of detection approximately five times lower than that of the capillary array. Although the mean SNR for each concentration from both devices was similar, the variance of the measurements from the capillary array was higher than that of the plate reader. This resulted in a higher calculated LOD.

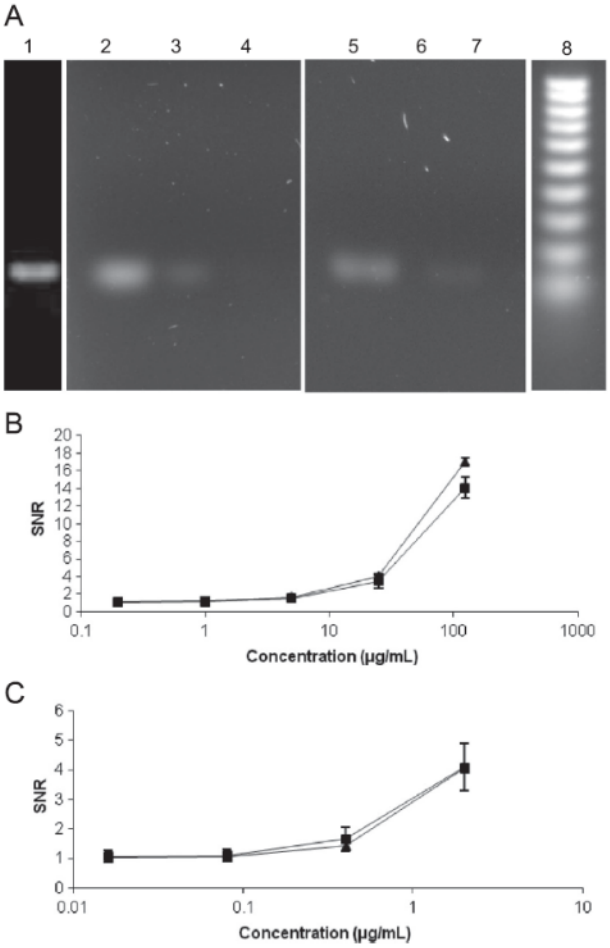

Figure 25 – Adenovirus detection by gel electrophoresis and fluorimetry - Adenovirus DNA was amplified with PCR. The 167-bp amplicon was labeled with SYBR green or fluorescein and was analyzed by gelelectrophoresis (A). In addition, the labeled DNA was measured by fluorimetry with a plate reader or with our capillary array using either SYBR green (B) or fluorescein (C). Panel A shows gel separation of a 10x serial dilution of adenovirus DNA stained with SYBR green (lanes1–4): lane 1 – undiluted DNA at 600 ug/mL; lane 2 – 60 ug/mL; lane 3 – 6 ug/mL and lane 4 – 600ng/mL. The DNA samples were also stained with fluorescein (lanes 5–7): lane 5 – 10 ug/mL; lane 6–1 ug/mL and lane 7–100 ng/mL. Lane 8 shows a100bp DNA ladder. Panel B shows the SYBR green stained 5x serial dilution (125, 25, 5, 1, and 0.2 ug/mL) analyzed by fluorimetry. The SNR was plotted against the various DNA concentrations. Triangles are data points for plate reader measurements, and rectangles are capillary array measurements. Panel C shows the same for fluorescein labeled DNA.

6. Micro-array reading with non-uniform excitation[1]

A technique to allow for quantitative measurement of fluorescently tagged antibody micro-arrays in the presence of non-uniform spatial excitation was developed. Conventional micro-array readers rely on scanning optics to provide uniform spatial illumination which allows for quantitative comparison of array spots. This new technique allows for the use of low cost optics without moving parts, resulting in designs that are potentially more robust and simpler to maintain by minimally trained staff.

Based on this technique, a novel CCD-based micro-array reader was developed for low cost high sensitivity biological assay measurement. Micro-arrays are commonly used for fluorescence based assays with a variety of target analytes including DNA, proteins, and antibodies. In this case a protein assay for staphylococcal enterotoxin B (SEB), a major contributor to food poisoning and a potential bio-terror weapon, was used to benchmark the performance of the system. Quantum dots were used as fluorescent markers due to the large separation in their excitation and emission wavelengths. A simple microfluidic device was developed to allow micro-array generation in a laboratory setting without the use of an array spotting device.

---

[1] This project was the result of collaboration between the author and Samantha Spindel, a doctoral student in the UMD Biomedical Engineering department. Her research group was responsible for assay design and optimization, the results of which are reported in section 6.2

6.1 Materials and methods

Assay preparation

Quantum dot-tagged protein assays were created on glass microscope slides through the following process: 1) glass slide pre-treatment with KOH, 2) immersion in 2% (3-mercaptopropyl) trimethoxysilane in toluene, 3) rinse in toluene, 4) expose to 2 mM γ-maleimidylbutyryl succinimide in ethanol (crosslinker), 5) flow solution of capture antibody (anti-SEB) and wash, 6) flow solution of target antibody and wash, 7) flow solution of biotin-anti-SEB and wash, 8) flow solution of quantum dots conjugated with streptavidin and wash.

In order to generate the assay in an array format on a glass microscope slide, a cross-flow microfluidic device was designed using laser machining and layered object manufacturing (LOM). Assay fluidic channels were laser cut from vinyl sheet with one side coated with adhesive for temporary bonding to glass slides. A schematic of assay channels and input ports is shown in Figure 26. After the assay was prepared the microfluidic layers were removed.

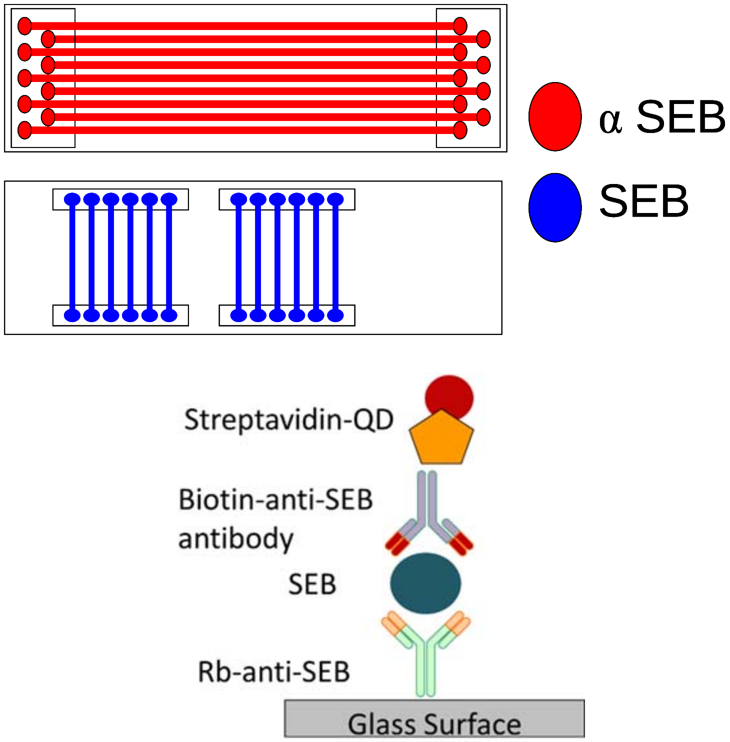

Figure 26 - Schematic of cross flow microfluidics – Orthogonal flow channels allow for the screening of multiple analytes simultaneously. Also shown is a schematic of the sandwich assay used.

Array reader design

A laser with center-wavelength of 450 nm was used to excite fluorescence in the quantum dots used for this assay (emission 655 nm). In order to illuminate the entire slide with minimal optical elements, the body of the slide was used as a waveguide for the laser and excitation took place through evanescent wave interactions with the surface-bound quantum dots. The laser was first passed through a line generator, resulting in a laser line which maintained a Gaussian profile. This line was coupled into a blank glass slide which, through many internal reflections, served to substantially homogenize the beam (Figure 27).

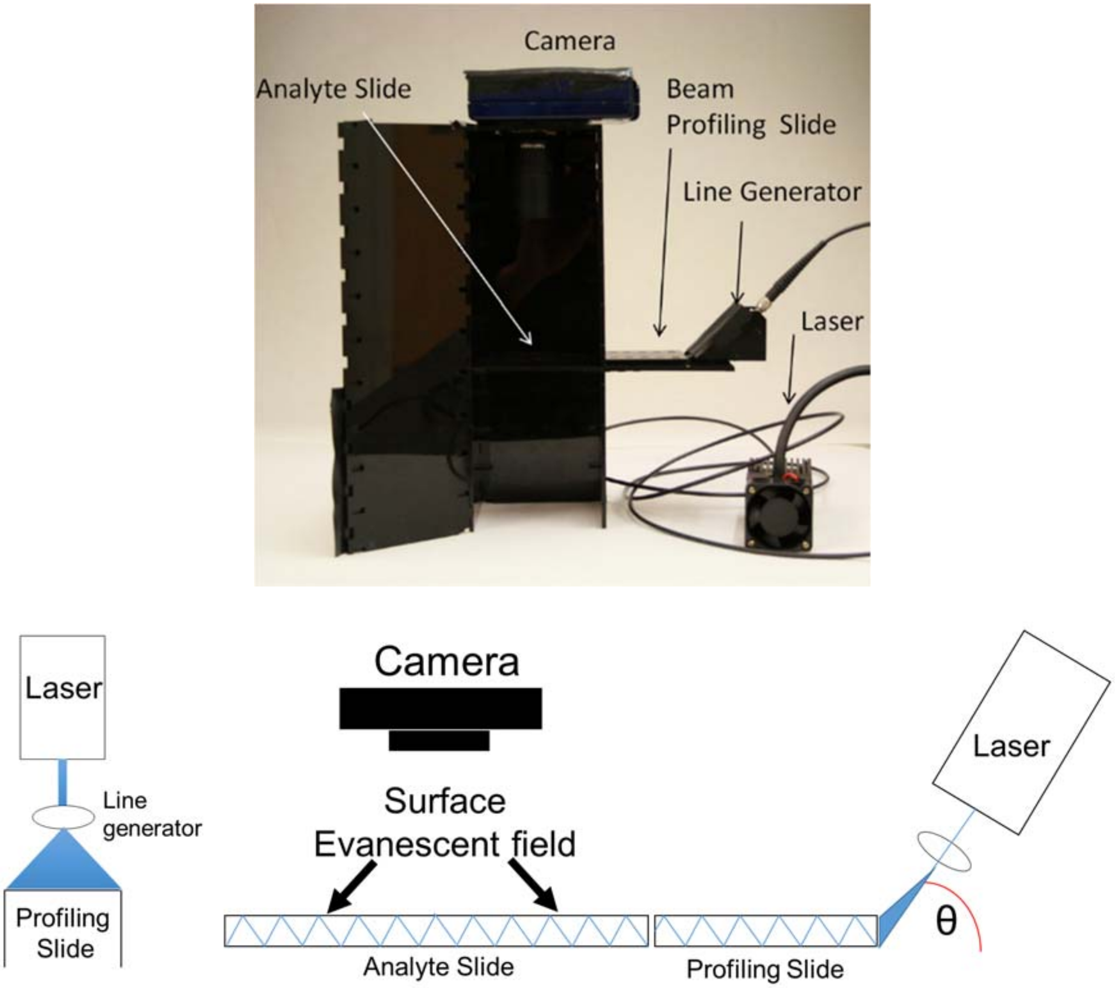

Figure 27 - Microarray reader schematic – A line generator and blank glass slide were used to homogenize the laser source used to excite fluorescence in the array reader. Evanescent wave interactions serve to excite surface-bound fluorophores in this design.

Figure 28 demonstrates the result of the excitation laser profiling. The background fluorescence of a plain borosilicate glass slide was measured and is shown here as a 3D surface plot. This background fluorescence is linearly proportional to excitation intensity, so this provided an indirect measurement of excitation field strength. Prior to beam profiling, background fluorescence showed an amplitude variation of approximately 25% (minimum to maximum) where the laser was injected into the slide, decreasing to <5% at the terminal end of the slide (Figure 28-A). After beam profiling, background fluorescence showed a variation starting at approximately 3% and decreasing to less than 1%.

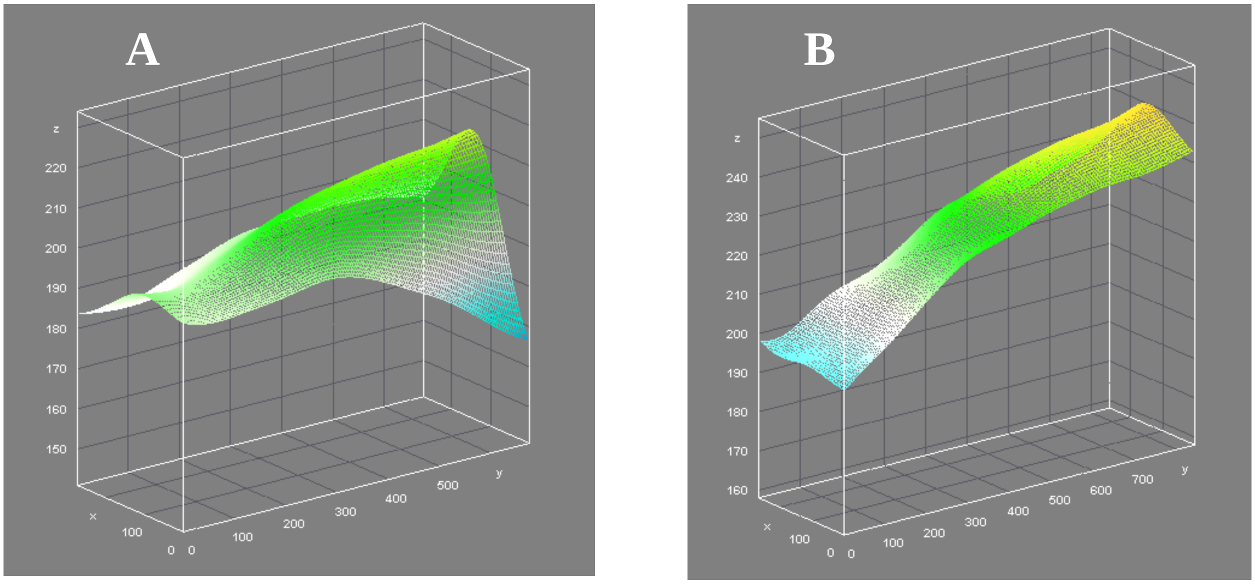

Figure 28 – Slide background fluorescence profile – (A) The background fluorescence profile of a blank slide before laser profile smoothing. The min-max variation across the short axis of the slide is ~25% at the left end where the laser is injected. (B) Background fluorescence after laser profile smoothing. The min-max variation has been reduced to 3%.

The background fluorescent emission was predominantly in the green range, and it necessitated the use of an emission filter matched to the 655 nm quantum dots. This was discovered when a multiplex assay using green (535 nm) quantum dots was attempted and their LOD was found to be significantly worse than that of their 655 nm counterparts. It was noted that the use of quartz slides significantly reduced this problem. However, for the purposes of designing an assay platform for global health, quartz slides were deemed to be too expensive to be practical. A typical image of a successful SEB assay using 655 nm quantum dots can be seen in Figure 29, along with the characteristic background fluorescence.

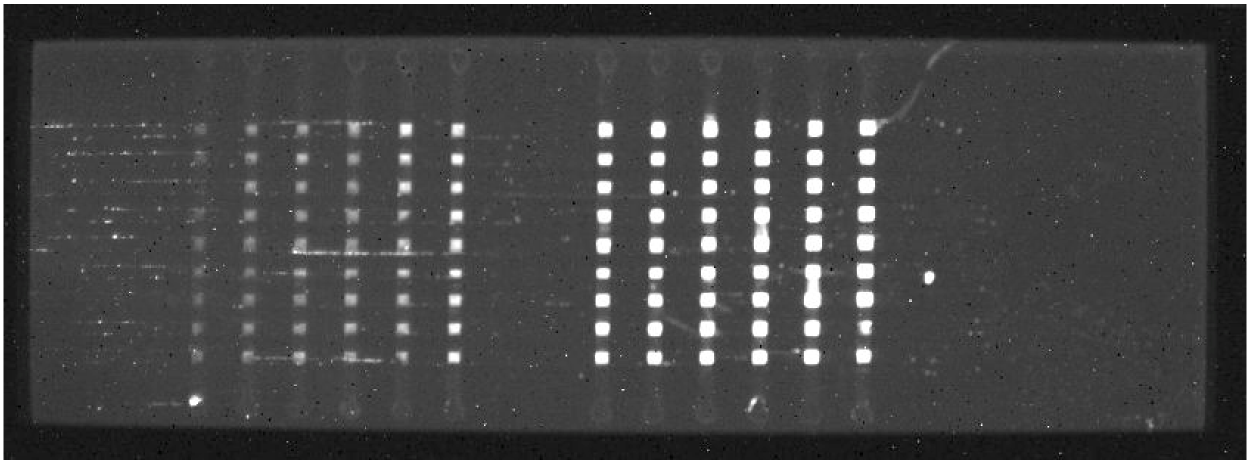

Figure 29 – SEB protein assay result – A 2X serial dilution of the target SEB protein, starting at 800ng/mL at the right hand side and decreasing to 80ng/mL, followed by a control sample at the far left side. Here, the background fluorescence from the slide is clearly visible in contrast to the black background.

Localized excitation normalization

As seen in Figure 28, though difficult to discern visually in Figure 29, the background fluorescence decreases across the length of the slide. This is due to the excitation light both being absorbed by the slide as well as it escaping from the edges of the slide where the total internal reflection condition is not met. This results in areas of the assay receiving different levels of excitation. In order to correct for this, each assay spot was measured and compared to its local fluorescent background level. Both the background fluorescence and the assay spot fluorescence are linearly proportional to the intensity of excitation light present in each portion of the slide. Points on either side each assay spot (in the direction of light propagation) were measured and interpolated to find the approximate background level at the point of the assay spot. The interpolated background levels for each column of spots were then normalized to a maximum value of one. This normalized value was interpreted as the relative strength of the excitation field. The strength of the wall intensity of an evanescent wave is related to the strength of this excitation field by the following two equations[191] for parallel and perpendicularly polarized light, respectively:

$$I_e^{||} = I_0^{||} \frac{4\cos^2(2sin^2\theta - n^2)}{n^4 cos^2\theta + sin^2\theta - n^2}$$

$$I_e^{\perp} = I_0^{\perp} \frac{4cos^2\theta}{1 - n^2}$$

Where $n = \frac{n_2}{n_1}$, n_2 is the refractive index of the measurement medium (1 in this case, for air), and n_1 is the refractive index for the micro array substrate (borosilicate glass, $n_1 \approx 1.52$). Here θ is the angle of incidence, which has a maximum of 90º and a minimum of θ_c, the critical angle for total internal reflection, given by $\operatorname{asin}(n) = 41.1°$. The formulae for evanescent wave intensity represent an upper and lower bound, plotted in Figure 30. The approximate operating location of the micro array reader is plotted based on a laser injection angle of 45º, and a mixed polarization state due to the use of a fiber optic delivery system between the laser source and the slide. Also, not all rays maintained their initial trajectory of 45º due to scattering at each end of the beam profiling slide, as well as scattering between the output of the beam profiling slide and the sample slide. It is therefore likely that this estimate of evanescent field wall intensity represents an upper bound. The effect that the adsorbed material in the assay spots have on the evanescent field strength was not quantified in these experiments. However it has been previously shown[192,193] that adsorbed monolayers of fluorescently tagged antibodies do not substantially affect the strength of an evanescent field via their absorption.

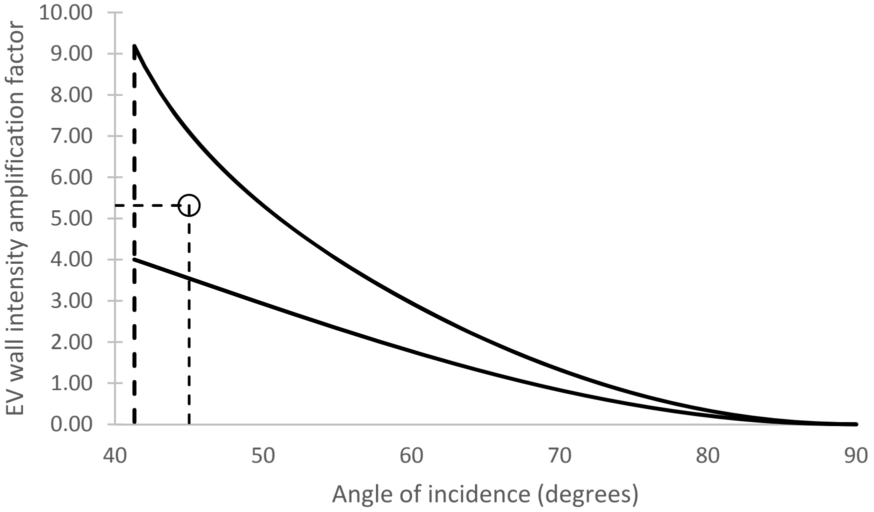

Figure 30 - Evanescent field amplification factor and operating location – Upper and lower bounds are plotted for the evanescent field intensity normalized to incident field intensity. The approximate operating condition of the micro array reader is plotted as a circular spot, with an injection angle of 45º and assuming a 50/50 mix of polarizations.

From Figure 30 it can be seen that a relative change of unit intensity in the excitation field within the glass slide results in a change in the evanescent field that is amplified by a factor the upper limit of which is 5. This factor was fitted to the data collected, and a best fit was achieved by a factor of 4. The effect of local normalization based on measurements of background autofluorescence and an evanescent field correction factor of 4 on a data set is seen in Figure 31. For the assay used to benchmark this system, the linear response range before local normalization was from 1.5 ng/mL to 6.25 ng/mL. After normalization the upper bound was improved to 12.5 ng/mL (a factor of 2). This modest improvement demonstrates the proof of principle. Further analysis and optimization of the assay itself could yield a further expanded range of sensitivity.

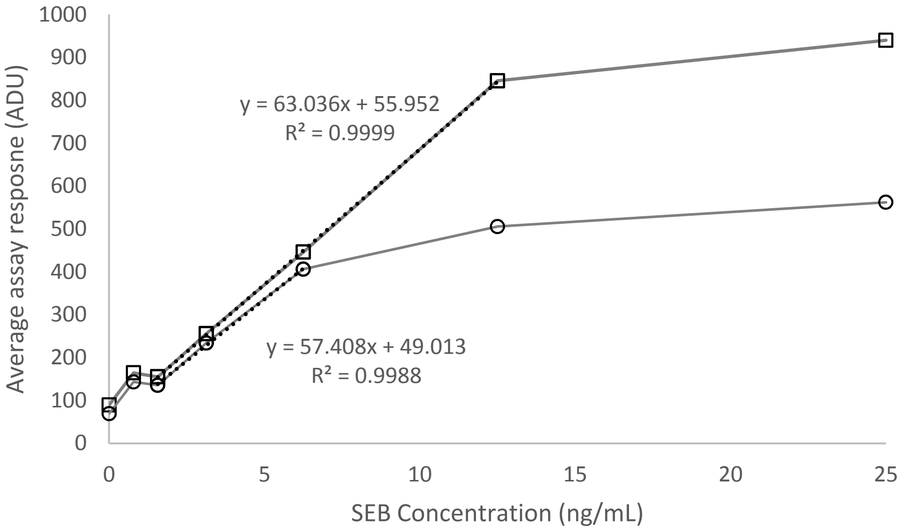

Figure 31 - Extended linear response range – Results from a typical micro array assay are shown before (circles) and after (squares) local normalization correction. The linear response range of the micro array reader was extended by a factor of 2 after local normalization in this example.

In order for this approximation to be accurate, an average dark frame must be subtracted from the image being analyzed. Exposure time of both frames must be equal. This is required because there will be a DC offset caused by the signal in the dark frame (thermal and bias signal) that will vary along the length of the slide (i.e. in the direction of digital image readout from the sensor). The necessity for removing this DC offset is seen by comparing Figure 32 and Figure 33. Without background subtraction, the two sources of fluorescence are not well correlated.

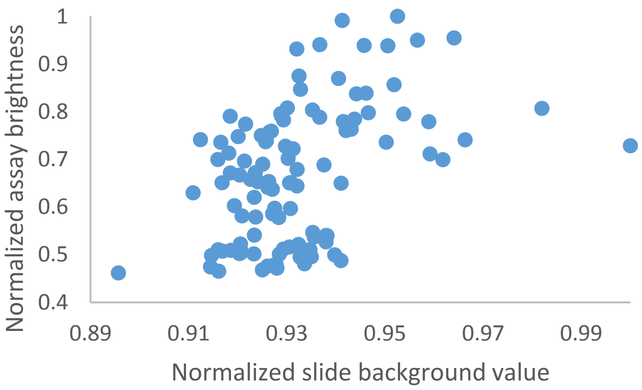

Figure 32 - Raw slide data – Very weak correlation between local slide background fluorescence and assay spot fluorescence value is seen prior to background subtraction.

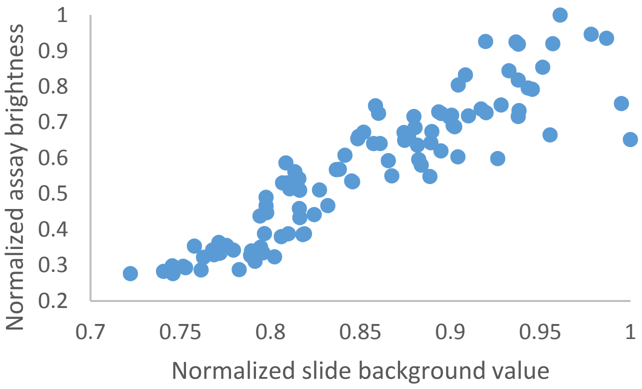

Figure 33 - Background subtracted slide data – Improved correlation between local slide background fluorescence and assay spot fluorescence is seen after background subtraction to remove offsets due to image bias and thermal signal.

6.2 Results and discussion

For the purposes of benchmarking method and device performance against a conventional detector, serial dilutions of antibodies were injected in the sixteen vertical channels in order to establish LOD. From the results of this experiment, an example of which are shown in Figure 29 and plotted in Figure 34, a LOD of 0.8 ng/mL was calculated for SEB detection, which is the same as the results for a similar ELISA-based assay conducted using a conventional plate reader. Results for this and other assays are presented in Figure 35. This data is presented here as a verification of the utility of the described method. Assay design and optimization, as well as data collection and analysis, were the original work of Dr. Samantha Spindel, and her results are reproduced here with permission. Results regarding the optimization of similar quantum dot labeled antibody assays (research on which Dr. Spindel was a primary contributor) for a 96-well plate reader format have been previously published[194,195]. The results discussed here are pending publication[196].

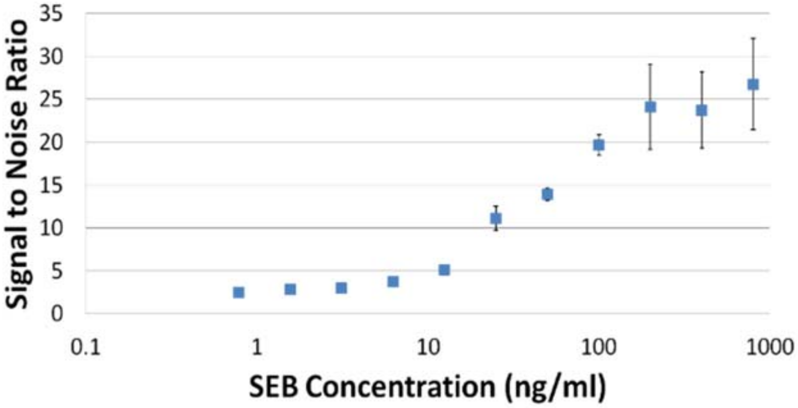

Figure 34 – Detection of SEB *via* fluorescent sandwich assay – A 2X serial dilution starting at 800 ng/mL and ending at 80 ng/mL was measured using the described micro-array reader. Note that the data point representing the control measurement is not shown – it represented a concentration of 0 ng/mL and could not be plotted due to the log scale of the x-axis.

Two multiplex version of the assay was also carried out: a spatial duplex and a spectral duplex. In the spatial duplex, each array spot had one of two antibodies bound (chicken IgG or SEB), and a multiplexed analyte solution could be analyzed based on the relative intensities of different spots. In the spectral duplex, each array spot had both antibodies bound to the slide surface, and a multiplexed analyte solution (with each species tagged with a different wavelength quantum dot) was analyzed based on the relative intensities of the same spot when imaged at two different wavelengths. Results are presented in Figure 35

Plate Reader Results

Target	Tracer	Format	LOD (ng/ml)
Chicken IgG	QD-605	Single	9.8
	QD-605	Duplex	9.8
SEB	QD-650	Single	7.8
	QD-650	Duplex	7.8

Micro-Array Reader Results

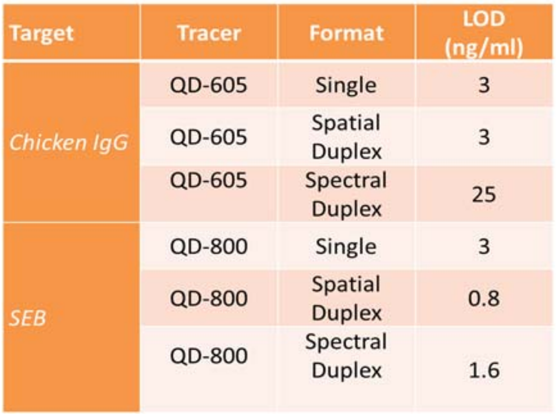

Target	Tracer	Format	LOD (ng/ml)
Chicken IgG	QD-605	Single	3
	QD-605	Spatial Duplex	3
	QD-605	Spectral Duplex	25
SEB	QD-800	Single	3
	QD-800	Spatial Duplex	0.8
	QD-800	Spectral Duplex	1.6

Figure 35 - Comparison of micro-array reader and plate reader performance - Assays were carried out in a conventional 96-well plate and in the micro-array format. In most cases, LOD of both systems was within the same order of magnitude with the micro-array reader yielding slightly lower numbers. One exception is the results for chicken IgG when a spectral duplex was carried out with SEB (i.e. both antibodies co-located in one array spot or in one well). In this case the effectiveness of the chicken IgG antibody was substantially diminished in the array format while no effect was noted in the 96-well plate format.

These results indicate that the presented methods for micro array generation, excitation, reading, and normalization result in a platform with effectiveness that is limited by the effectiveness of the assay utilized.

7. High throughput flow cytometry for rare cell detection

A technique for optimizing the physical design and operating parameters for a wide-field flow cytometer were developed, along with a technique for the qualification and implementation of low cost image sensors for the application of rare cell detection. Fundamental imaging principles were adopted from the machine vision, astronomical imaging, and fluid velocimetry communities. These methods were used to develop and refine a proof of concept flow cytometer capable of sample throughput of up to 10 mL/min, and accurate counting of rare cells at concentrations of 0.1 cell/mL.

All of the aforementioned projects have been concerned with the development of viable biodetection platforms for the global health arena. However, they have all been developed and used for the analysis of spatially static objects (*i.e.* immobilized arrays of assay products). It was therefore possible to obtain highly sensitive fluorescence measurements using relatively inexpensive equipment by employing time-domain signal averaging: faint sources of fluorescence were detected by using extended integration times, and sources of noise were mitigated using repeated measurements.

For biodetection applications that involve spatially dynamic samples (such as flow cytometry) these methods are not directly applicable. To expand the scope of this research a new methodology for fluorescent based flow cytometry for rare cell detection was developed which is suitable for the global health arena. Rare cells, such as circulating tumor cells, are currently under investigation as potential biomarkers for the early detection of cancer. These cells are typically found at the rate of one to ten cells per mL of whole blood. A typical blood collection volume is 7.5 mL, so in order to have sample analysis times of less than one hour, sample throughput rates must be at least 125 μL/min, with a preferred target of better than 750 μL/min for complete analysis in under ten minutes.

For a fixed device design, increasing flow rates results in increased particle velocity and decreased signal to noise ratio due to shorter residence time in the sensor field of view and correspondingly fewer photons collected. In order to increase flow rates without sacrificing accuracy, the SNR of the cell signals must be increased. This can be accomplished in two fundamental ways: collecting more photons from each cell, and decreasing the level of background noise in the measurement. The first option can be accomplished in several ways: attaching more fluorophores to each cell, using fluorophores with higher quantum yield, using more efficient collection optics, or using higher power excitation sources. The second option, decreasing background noise, can be accomplished be eliminating sources of photon noise (primarily from autofluorescence of the flow cell material and scattered rays from the excitation source[202]), or by choosing a sensor with lower intrinsic noise. The former is typically the dominant noise source when scientific CCD cameras are utilized. For low cost CMOS sensors, such as those found in webcams, at low illumination levels intrinsic sensor noise can easily become the dominant noise source.

Increasing the efficiency with which the emitted fluorescent photons are detected is typically accomplished via specialized collection optics and high quantum efficiency detectors such as PMTs, EMCCDs, or back-thinned CCDs. These advanced detectors are not suitable for deployment in resource-poor regions. Not only are they expensive, but they are generally not field-serviceable or readily replaceable in the event of a failure. For these reasons we selected a CMOS webcam (price $40) for our initial experiments in rare cell detection. We later added a low end scientific CCD camera ($300) in order to accurately characterize certain aspects of system performance and expand functionality.

7.1 Conventional imaging-mode rare cell detection

Current flow cytometry which is based on photomultipliers or other narrow field detectors relies on flow focusing to constrain the spatial location of cells to a very narrow region. Hydrodynamic flow focusing allows cells to be interrogated one at a time by the narrow field detector. There are several advantages to a flow focusing design. Because the path of every cell is nearly identical, the area over which laser excitation is needed is much smaller. This allows for a lower power laser to be used if it is focused onto this small area (decreasing power requirements and device cost). Similarly, the narrow field detector can be focused to a point measurement. Such detection schemes are used in commercial flow cytometers which use point detectors (typically photomultiplier tubes). However, typical flow rates used in devices such as this are on the order of 10 μL/min which is not suitable for analysis of rare cells. At this flow rare, 7.5 mL of sample (a volume commonly used for CTC analysis) would require 12.5 hours to measure. So there is a need for large volume high throughput cytometer rare cell detection

7.1.1 Materials and methods

Flow cell fabrication

A flow focusing cell (Figure 37) was fabricated using an Epilog Legend CO_2 65 W laser cutter (Epilog, Golden, CO) using similar techniques described in our previous work[210,220-

[224]. The flow cell consisted of three functional layers. The top layer consisted of a 3 mm thick clear acrylic plate (75 x 25 mm) with laser machined inlet and outlet ports into which 18GA needles were pressed and bonded to allow for sample injection and waste collection. The middle layer, which defined the shape of the fluid flow, was laser machined from a single layer of 3M 9770 double-sided adhesive transfer tape (Piedmont Plastics, Beltsville, MD), resulting in a flow cell with width 0.2 mm, length 45 mm, and depth of approximately 0.075 mm. The bottom layer consisted of a single glass microscope slide. The wide field flow cell (Figure 38) was fabricated with steps identical to those of the flow focusing cell, with the exception of the width of the channel in the middle layer, which was 4 mm (20X wider). A Fusion100 syringe pump was used for flow rate control (Chemyx, Stafford, TX).

Webcam-based cytometer platform

A Sony PlayStation® Eye webcam was used as the photodetector. A c-mount CCTV lens (Pentax 12 mm f/1.2) was used to replace the stock webcam lens. For florescence detection, a green emission filter with center wavelength 525 nm and bandwidth 50 nm (Chroma Technology Corp., Rockingham, VT) was used for detecting fluorescent emission. For fluorescent excitation, a 1 W 450 nm laser module was used (Hangzhou BrandNew Technology Co., Zhejiang, China). The laser illuminates the flow cell at an angle of approximately 45º. The flow cytometer platform was constructed using 0.5 inch thick clear acrylic sheet and nylon rod (McMaster-Carr, Robbinsville, NJ).

Computer control and data analysis

The webcam sensor was connected to a 32-bit Windows-based laptop computer via a USB2 port. Drivers and software allowing the webcam to be controlled on a personal computer were developed and freely distributed by Code Laboratories, Inc. (Henderson, NV). The camera control software (CL-Eye Test) was used to set camera parameters (exposure time, frame rate, and gain) and to capture and save video in uncompressed AVI format. Video files were analyzed using ImageJ software (freely distributed by NIH, http://rsb.info.nih.gov/ij/download.htm), and data analysis and plotting was carried out in Microsoft Excel (Redmond, WA).

Cell culture and staining

Fluorescently stained THP-1 human monocytes were used as a model to simulate rare cell events. Though monocytes themselves are not rare, they were diluted to levels similar to those of rare cells such as CTCs. Cells were removed from an active culture, pelleted by centrifugation and resuspended in deionized water. 10 µL SYTO-9 dye (3.34 mM stock concentration) was added to 1 mL of suspended cells and allowed to rest at room temperature in the dark for 20 minutes.

Rare cell dilution preparation

After staining, the stock solution of cells was diluted to a level of approximately 10 cells/µL (measured by microscopy) to allow for manual counting. Cell concentration was measured by placing 3 µL sample droplets on a microscope slide and counting cells in the droplet in real time under laser excitation using the same imaging platform employed to image the flow-cells in these experiments. This was repeated many times (N > 20). An average cell concentration of 9.3 cells/μL with a standard error of 0.4 is an example of a typical result of these measurements. From this relatively high concentration, lower concentration samples of 100, 10, and 1 cell/mL were generated by single-step dilution. For each dilution, 107.5 μL of stock solution (with measured concentration of 9.3 cells/μL) was diluted into a volume of buffer to yield the final target concentration (10 mL, 100 mL, and 1000 mL of buffer for concentrations of 100, 10 and 1 cell/mL, respectively). Based on a normal sampling distribution with standard error of 0.4 cells/μL, the 95% confidence range for each concentration was 92-108, 9.2-10.8, and 0.92-1.08 cells/mL for concentrations of 100, 10 and 1 cell/mL, respectively. Pipetting volume error was measured to be less than 1%.

Rare cell counting

Cell dilutions were loaded into a 3 mL syringe and injected through the wide-field flow cell at a rate of 500 μL/min. This was the highest flow rate that resulted in cell images which were not streaked when imaged at the maximum frame rate of the webcam sensor (187 fps). Video of this flow was saved and analyzed later in ImageJ. The video files generated were typically around 10-15 GB in size, and had to be opened and analyzed in several fragments. After being opened in ImageJ, each fragment of video was split into its three color channels (red, green, and blue). The fluorescent dye used in this case had its emission peak in the green channel, so the red and blue channels were discarded to reduce background noise.

7.1.2 Results and discussion

Fluorescent dye characteristics

In initial experiments, presented in Figure 42, cells were noted to lose fluorescent intensity over time. To measure this effect, a 30 mL sample was prepared with freshly stained cells. This sample was run through the flow cytometer at a flow rate of 125 μL/min and imaged at a frame rate of 1 fps. Brightness measurements were made on over 5,000 cells during this four hour experiment (average concentration of 175 cells/mL). The raw data is plotted in Figure 36, along with the following model to predict the rate of diffusion:

$$\frac{d\mu}{dt} = C_1 erfc\left(\frac{C_2}{\sqrt{C_3 t}}\right)$$

where μ is mean pixel brightness value, *erfc* is the complementary error function, and constants $C_{1\text{-}3}$ are used to fit the *erfc* function to the data.

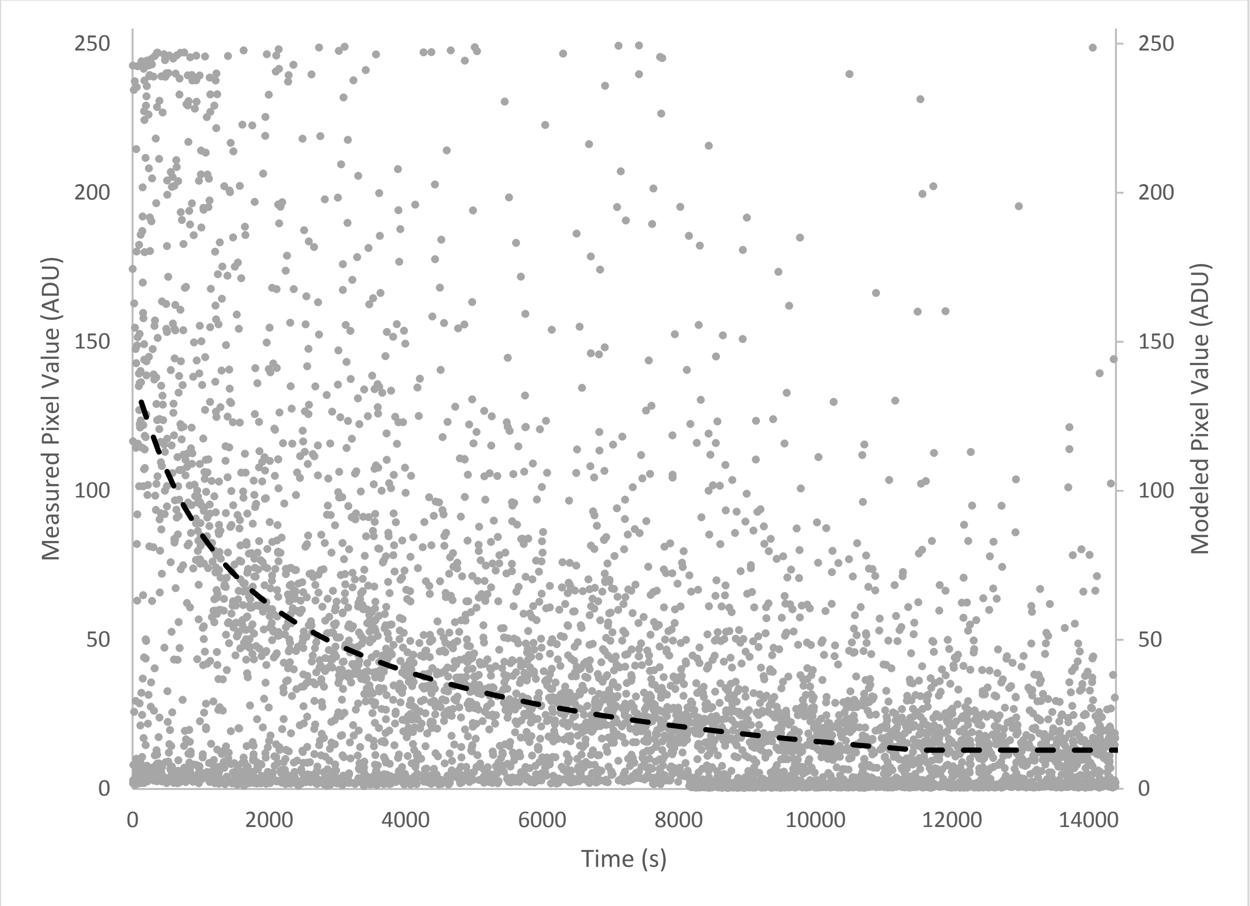

Figure 36 - Dye diffusion modeling – Syto-9 dye is a DNA permanent dye. After being removed from a high concentration of dye, unbound dye within the cell diffuses out over time, following a classic diffusion curve.

A population of faintly stained cells can be seen along with the bright THP-1 monocytes in Figure 36 as a band of data points that stays close to the horizontal axis during the experiment.. The ratio of cell brightness between these two populations was approximately 10-15X after diffusion was complete. An apparent discontinuity can be seen in this population of cells at the 8000 second mark in the plot. This is a result of a change in the searching algorithm that allowed for these faint cells to be detected. The overall trend in the primary bright population of cells was not affected by this change. Syto-9 dye is known to have a quantum yield of approximately 0.6 when bound to nucleic acids, and less than

0.01 otherwise. In live eukaryotic cells such as these, the dye is known to show diffuse cytoplasmic staining. Fluorescent microscopy confirmed the presence of a sub-population of cells which lacked the characteristic bright nuclear staining of healthy live cells and showed only faint staining. A likely explanation for this is cell anucleation due to cell culture stress.

Flow focusing cytometry

The first iteration of our imaging flow cytometer platform was based on a flow focusing cell and a webcam as detector. Figure 37-I shows a schematic of the flow focusing cell. In this cell configuration there are three fluidics inlets, a sample inlet (A) and two sheath fluid inlets (B). The interrogation region for the webcam is shown at (C) and a waste outlet at (D). A schematic (Figure 37-II) and a photograph (Figure 37-III) of the flow focusing effect are shown using food dye for visualization shows a focused stream of ~30 μm in a 150 μm channel.

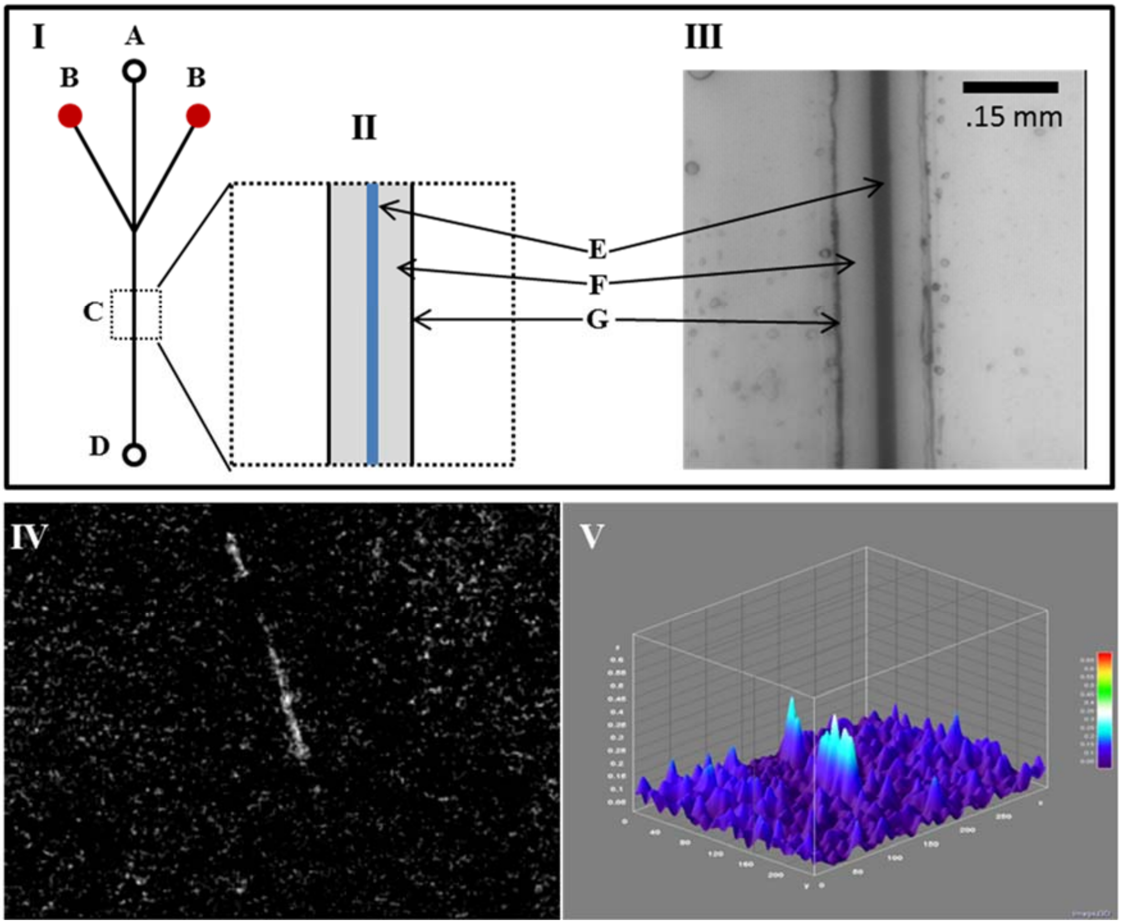

Figure 37 - Hydrodynamic focusing flow cell design - (I) A schematic of the flow focusing cell shown with key structures: A) sample inlet, B) sheath fluid inlets, C) interrogation region, D) waste outlet. (II) A schematic of the flow focusing interrogation region with features labeled E) focused sample stream (food dye used for visualization), F) sheath fluid, G) channel boundary. (III) A photograph of flow focusing. (IV) An image of flow-focused 5 µm polystyrene beads, (V) 3D representation of image signal from IV.

One of the main limitations of this focusing flow-cell fabricated by lamination is the maximum sample flow rate. We found that the maximum flow rate achievable was limited by the ability of the flow cell to withstand pressure. The hydrodynamic resistance from the Poiseuille flow through a narrow channel of effective diameter, d, increases proportionally to $1/d^4$. In our flow cell, leaks developed around the chip interface ports at flow rates above 100 µL/min, and the layers of the flow cell began to delaminate.

We tested the flow focusing cell for the detection of 5 µm polystyrene beads, detected by a regular 30 fps webcam. Even with low flow rate we were unable to image the beads due to image streaking and poor image quality. So, a webcam with a faster frame rate was employed (Sony PlayStation® Eye webcam). For a typical rare cell detection case, several milliliters of sample must be interrogated. For a 10 mL sample, a flow rate of 100 µL/min would result in a 100 minute analysis time. Even with a flow rate of 100 µL/min in our flow focusing cell, using the maximum camera frame rate of the webcam sensor we employed (187 fps) was not sufficient to capture all of the passing cells. A reduced flow rate of 10 µL/min was required because of the camera limitation. Even with this flow rate (which would requires 16.7 hours for 10 mL analysis) bead streaking caused by the movement of the beads in the 1/187 second was observed (seen in Figure 37 and Figure 40) suggesting that flow focusing combined with webcam detection is not practical for rare cell detection. It is for this reason that a non-focusing wide-field flow-cell was developed.

Webcam-based flow cytometer with wide-field imaging for high throughput rare cell detection

A wide-field flow-cell was developed in order to overcome the flow rate limitations of a flow focusing cytometer design. The design utilizes the inherent wide-field imaging capability of an array sensor and reduces the analysis time for rare cell detection.

As shown in Figure 38, the flow cytometer consists of four modules: a webcam sensing element, a laser excitation source, a flow cell, and a focusing stage to hold each module in alignment and enable focusing. The sensing element consists of the internal elements of a webcam, a 12 mm f/1.2 CCTV lens, a green emission filter, and a computer to collect and analyze data. The excitation source is a 1W 450 nm laser module. The sample handling module consists of a flow cell and a programmable syringe pump.

The flow-cell (Figure 38-B) consists of a 4 mm wide channel through which sample is injected via an inlet and collected at the outlet. The maximum flow rate achievable through this flow cell was 10 mL/min (limited by flow cell integrity). However, the flow rate in experiments was limited to 500 μL/min due to the maximum frame rate achievable by the webcam employed for sensing. This was done to eliminate cell image streaking. As will be explained in later sections, the requirement imposed here for no image streaking was not necessary for the case of rare cell detection and actually resulted in lower device sensitivity.

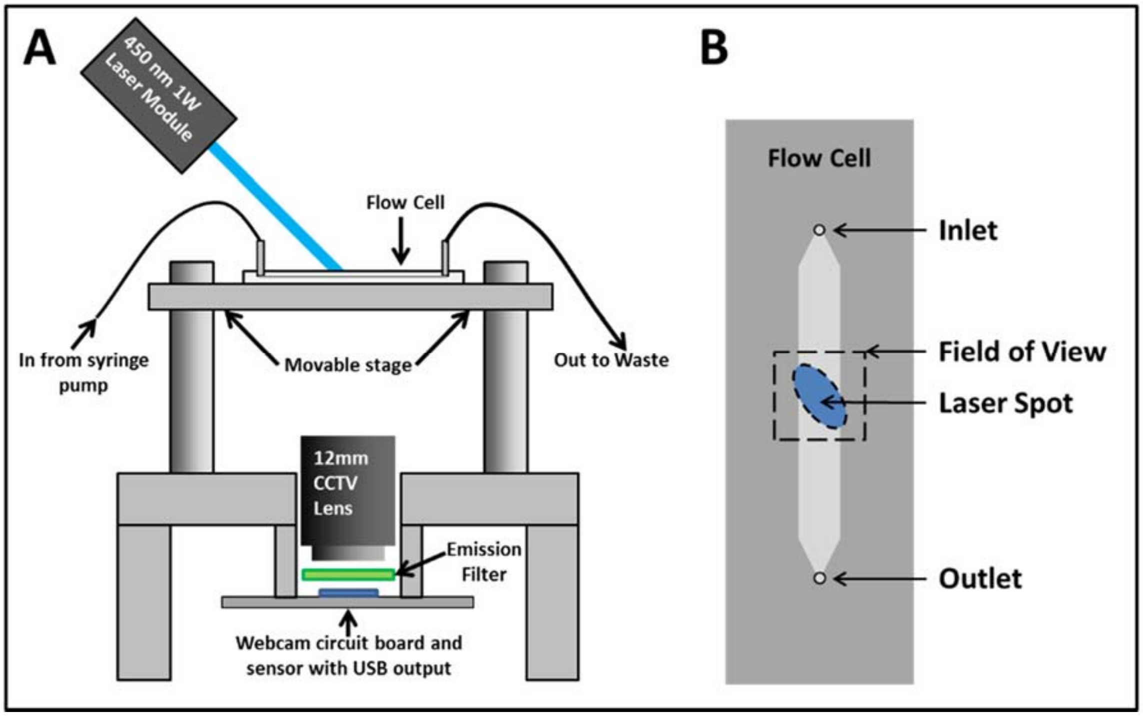

Figure 38 - Schematic of webcam-based wide-field flow cytometer – (A) The wide field flow cytometer consists of four modules: a sensing element, excitation source, flow cell, and a stage to hold each module in alignment. The sensing element consists of the internal elements of a webcam, a 12 mm f/1.2 CCTV lens, a green emission filter, and a computer to collect and analyze data. The excitation source is a 450 nm 1W laser module. The sample handling module consists of a flow cell and a programmable syringe pump. (B) A schematic of the wide-field flow call with key elements labeled.

A challenge inherent in fluorescent imaging of a wide field flow cell is uniform excitation. In this case, a 1 W consumer laser was used to project an elliptical spot which covered the width of the flow cell. A laser such as this is fairly expensive (~$300) for a device designed for use in a low-resource setting. To reduce the cost of the laser, a lower power laser with line generator optics could be used to further focus the laser spot. This could allow the critical parameter of photon flux to remain unchanged while reducing overall power. Another alternative is to use high power LEDs which are significantly less expensive, but which would require the addition of an excitation filter in order to prevent leakage into the emission band of the dye, as well as optical elements for collecting and focusing excitation light onto the interrogation region.

A Sony PlayStation® Eye webcam was used as the photodetector in this platform by converting the webcam to a wide-field microscope. The device was disassembled and the main circuit board (with attached image sensor and USB cable) was removed. The circuit board was incorporated directly into the flow cytometer platform, and a C-mount CCTV lens (Pentax 12mm f/1.2) was used to replace the stock webcam lens.

The webcam sensor employs a typical Bayer pattern color filter array, in which one half of all pixels has a green filter, 25% have a red filter and 25% have a blue filter. Typical spectral response curves for these color filters is shown in Figure 39, along with the emission profile of Syto-9 dye. As Syto-9 has most of its emission in the green spectrum only the green channel of images was used for analysis while red and blue channels were discarded due to low SNR.

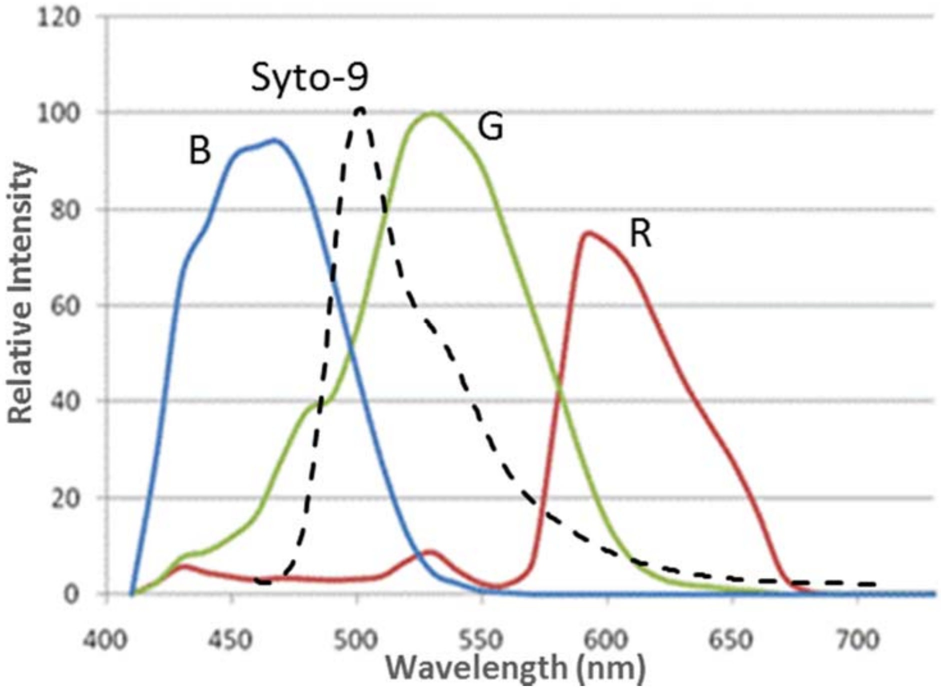

Figure 39 - Emission spectrum of Syto-9 dye compared to sensitivity of CMOS sensor – A typical spectral response for a color CMOS sensor is shown, comparable to the sensor found in the webcam used here. The emission spectrum for Syto-9 dye is overlaid, showing its greatest overlap with the green channel of the sensor.

A single video frame of THP-1's stained with SYTO-9 dye in wide-field flow cell at a flow rate of 500 μL/min is shown in Figure 40-A. The flow-cell geometry and fluorescent detection optics allow for a high signal to noise ratio for easy detection of these cells (Figure 40-B). Compared to a single video frame from flow-focused cell flowing at 10 μL/min (Figure 40-C and Figure 40-D), this suggests that the wide-field cytometer has potential for large volume, high throughput rare cell analysis.

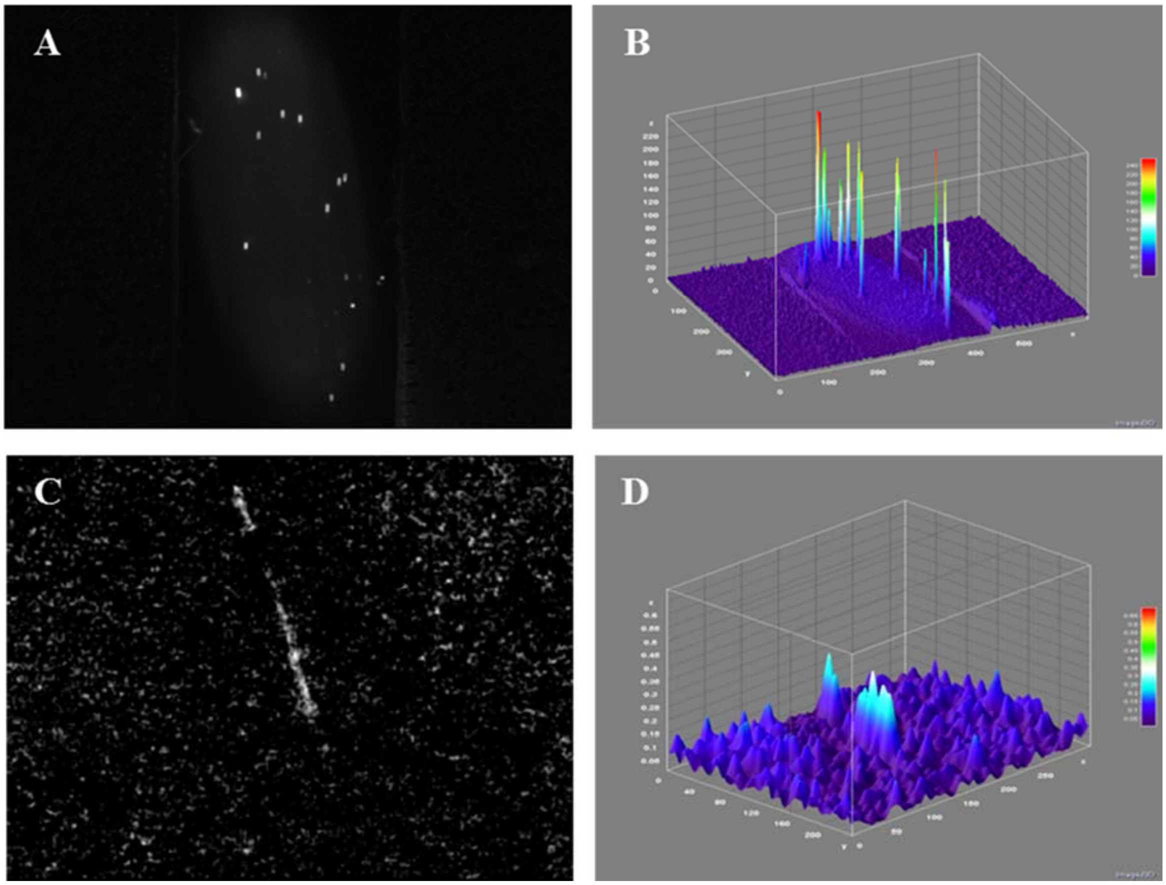

Figure 40 - A comparison between webcam-based wide-field flow cytometer and webcam-based flow focusing cytometry - A) single video frame of THP-1 human monocytes in wide-field flow cell flowing at 500 μL/min, B) 3D visualization of A, C) single video frame of polystyrene beads in flow-focused cell flowing at 10 μL/min, D) 3D visualization of C.

Rare cell counting

To analyze the performance of the wide-field cytometer, human monocytes stained with SYTO-9 dye were analyzed. Figure 41 shows the analysis of a video clip where a single cell moves through the laser spot. Figure 41-A shows a schematic of the primary elements in each video frame: the flow channel, the laser spot (visible due to autofluorescence of the flow cell), and the direction of flow. Figure 41-B shows the green channel of a single video frame where no fluorescent cells are present, and Figure 41-C shows a single frame where a single cell (circled) can be seen moving through the flow cell. In this example, a video clip containing 2,000 frames (10.7 seconds of video) showed a single cell passing through the flow cell. In order to quickly find a rare event such as this without manually scanning each frame, an image stacking approach was used. The median value and the maximum value of each pixel in the stack of 2,000 frames was calculated. The median image is shown in Figure 41-D, and the maximum image is shown in Figure 41-E with the cell position in each frame marked with an arrow. The median image represents the typical background signal, while the maximum image represents the highest signal recorded at each pixel during the video. In the maximum image, the path taken by a single fluorescent cell can be clearly seen. In order to aide in distinguishing the cell images from background signal, the median image was subtracted from the maximum image to produce Figure 41-F which allows for improved visualization of cell movement. This method of combining multiple video frames was useable for concentrations of cells up to 100 cells/mL when small sub-stacks of frames were analyzed. At higher concentrations, the overlap of cell images made it difficult to uniquely identify single cells and frame by frame counting was required.

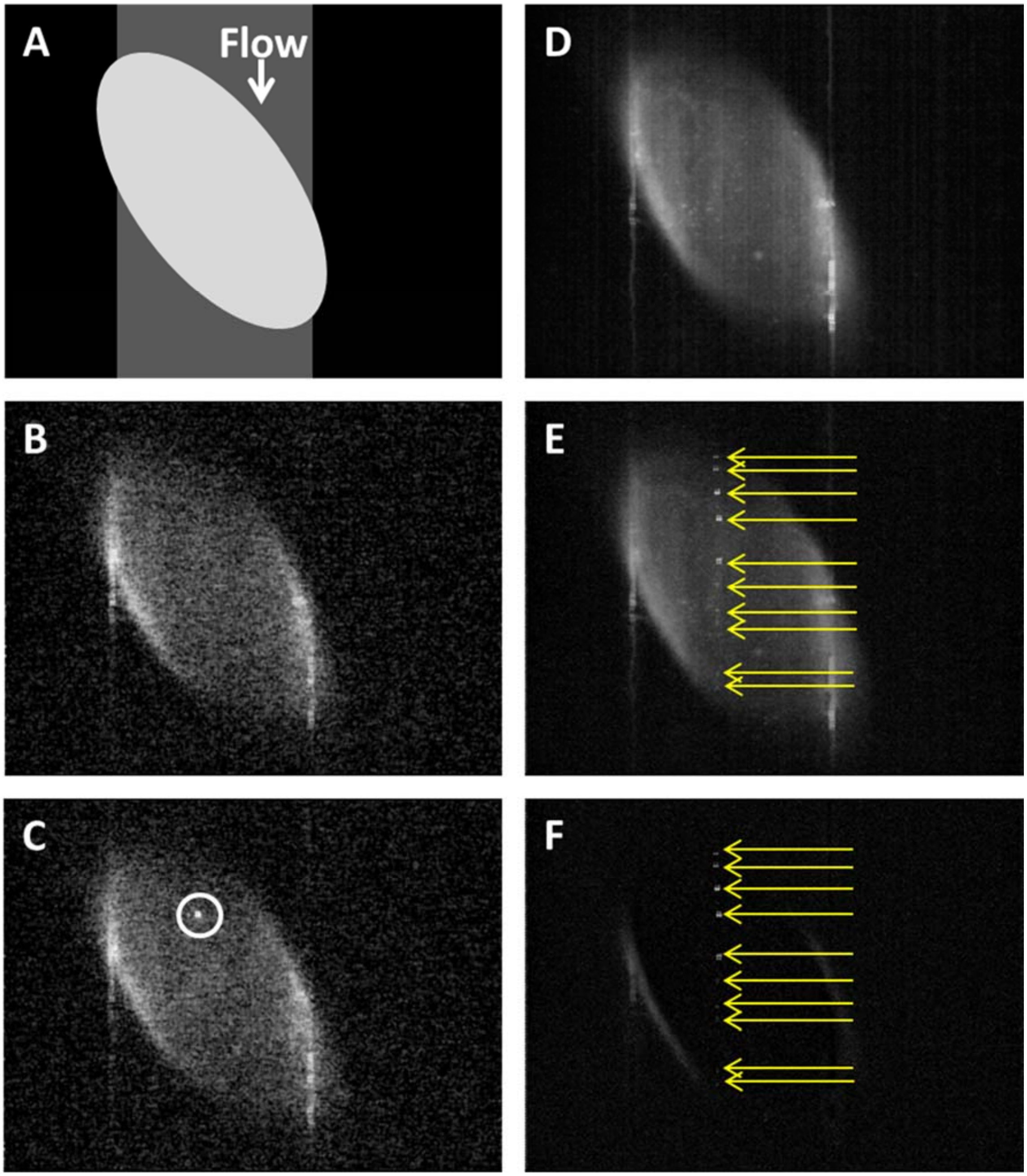

Figure 41 - Analysis of a single cell using webcam-based wide-field flow cytometry - (A) Schematic of webcam field of view showing flow channel, elliptical laser illumination spot and flow direction, (B) single raw video frame showing no fluorescent cells present, (C) single frame showing one cell, (D) median pixel value from 2000 frames showing average background autofluorescence from flow cell, (E) maximum pixel value from 2000 video frames showing a single cell moving through the laser spot (marked with arrows), (F) result of subtracting image D from image E, allowing for improved visualization of cell movement and faint cell images.

Flow cytometer counting performance

To determine the counting accuracy of this flow cytometer platform serial cell dilutions were counted (100, 10, and 1 cells/mL). The expected number of cells was determined as described previously (*"Rare cell dilution preparation")*. The number of expected cells in each dilution was compared to the average number of cells counted by the wide-field flow cytometer (N > 10). Figure 42 compares these two values with error bars representing 95% confidence intervals. In general there was agreement between the calculated expected number of cells and the number measured. The average cell numbers measured by the flow cytometer for were 84 cells/mL (100 cells/mL target), 7.9 cells/ml (10 cells/mL target) and 0.56 cells/mL (1 cell/mL target).

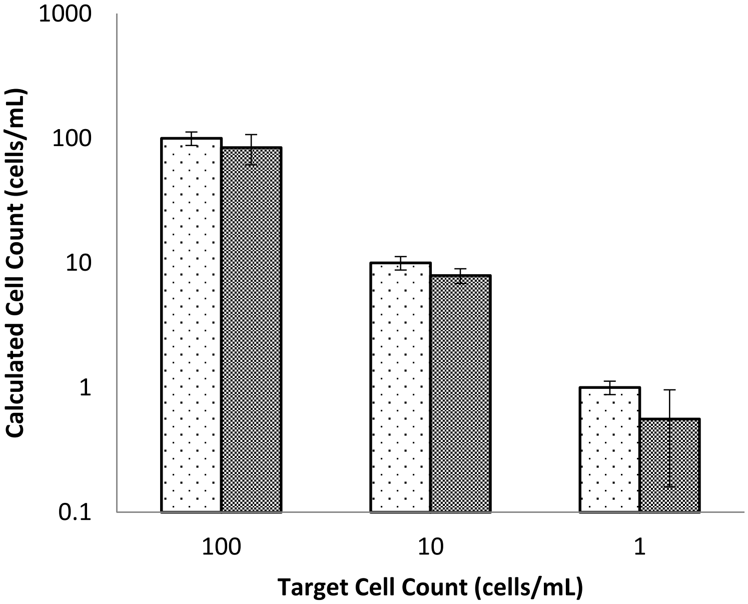

Figure 42 - Webcam-based wide-field flow cytometer counting efficiency - Results of three concentrations of human monocytes counted manually (sparse fill) and using the webcam-based flow cytometer (dense fill). Error bars represent standard error for each data set. Manual counting was performed at a higher stock concentration (1000 cells/mL) and the results for each target concentration were calculated. It was later found that lingering unbound dye in the cells was causing them to appear artificially bright in

experiments conducted shortly after staining, and gradually loose fluorescent intensity as this unbound dye was diffused. In this experiment, the 1 cell/mL data was collected last so its cells had diminished in brightness significantly.

This plot data suggests that the flow cytometer platform is capable of measuring in a range of cell concentrations applicable to rare cell detection, although the counting efficiency appears to decrease with decreasing concentration. This decrease in performance can be understood based on two factors which were only completely understood several weeks after this data was collected. The first factor is the diffusion profile of the dye, presented originally in Figure 36 and repeated in Figure 43. The second factor is the relationship between image SNR and flow rate.

For the experiments behind the data in Figure 42, stained cells were diluted to the three desired concentrations, and then the three concentrations were measured in series starting with 100 cell/mL and ending with 1 cell/mL. This resulted in the cells of the 1 cell/mL stock solution waiting for approximately 1 hour before being processed, in which time their inherent brightness would have decreased by a factor of ~2 compared to the brightness of the cells in the first experiment. The approximate location of the cells on the diffusion curve has been circled in Figure 43.

As previously explained, flow rate was set to the highest value that resulted in un-streaked cell images at the highest frame rate the camera was capable of. It will be shown in section 7.2.2 that this operating condition results in the lowest possible SNR for imaged cells. This can be readily understood by considering the number of photons deposited by a cell in each image frame. This number decreases with increasing frame rate, and decreases with increasing flow rate. Therefore by maximizing both frame rate and flow rate, SNR was minimized, resulting in an elevated limit of detection. When average cell brightness decreased by a factor of ~2, this placed some cells below the LOD of the operating conditions.

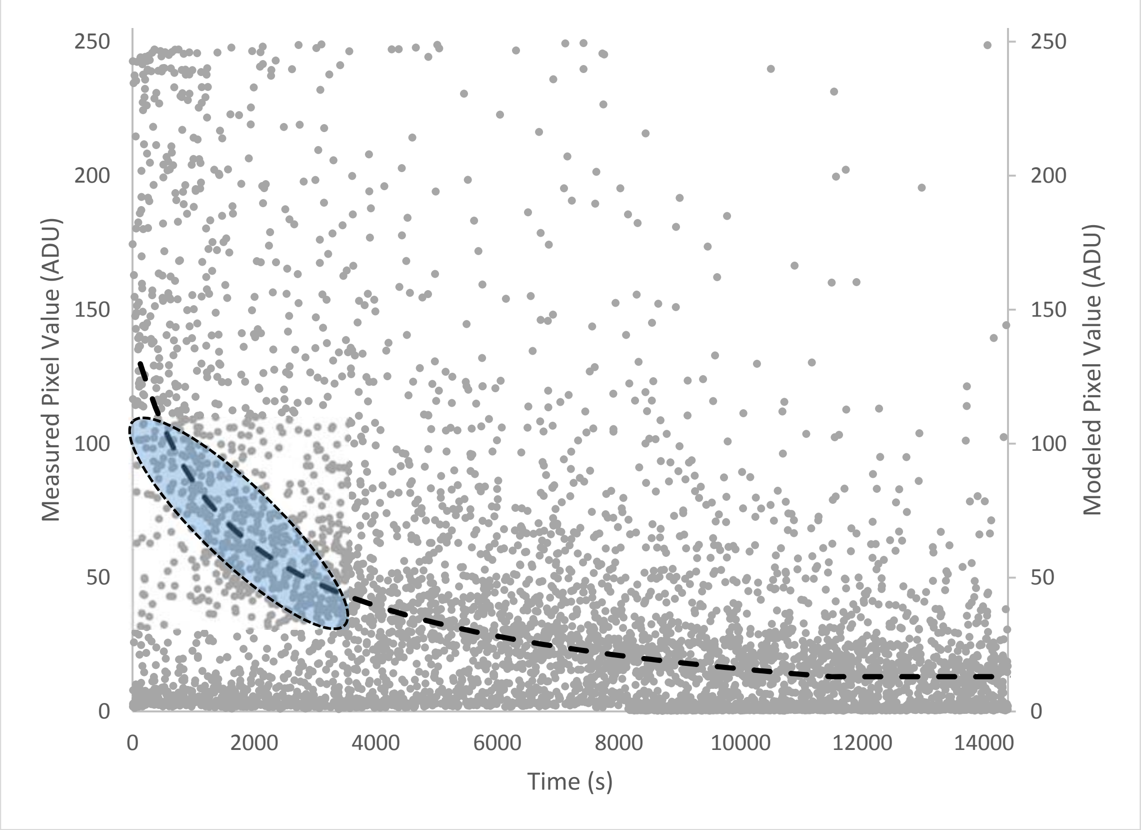

Figure 43 – Approximate stage of dye diffusion during cell counting – Plot repeated from Figure 36. The overlaid ellipse indicates the approximate stage of dye diffusion during the

7.2 Streak-mode imaging rare cell detection

The performance of the first generation wide-field imaging cytometer at sample concentrations as low as 10 cells/mL was acceptable, with counting accuracy comparable to that of other proposed low cost systems[213,214]. However, the counting accuracy at the level of 1 cell/mL (around 56% on average) left significant room for improvement. For this reason a second generation device was developed and optimized based on principles described in the following sections in order to improve detection at ultra-low concentrations. The most significant improvement was the development of a new image capture methodology based on the principle of particle streak photography developed in the early 20th century by the fluid dynamics community.

7.2.1 Materials and methods

Flow cell fabrication

Fabrication methods were identical to those described in section 7.1. A new flow cell was designed based on the equations outlined in the preceding section. In order to maximize residence time of cells in the interrogation window to maximize the number of fluorescent photons captured, the fluid volume of the interrogation window was maximized for the microscope-slide form factor. This was accomplished be widening the flow channel from 4 mm to 20 mm. Channel depth was kept constant in order to avoid significant velocity variations of a 3D flow field, and to keep the flow channel within the narrow depth of field of the lens being used (Pentax CCTV 12mm f/1.2, operated at approximately f/2.4 to reduce field curvature and improve depth of field). In order to provide approximately uniform excitation across the width of the channel, the laser source was injected into the side of the flow cell such that it formed a linear band of excitation across the center of the field of view, as seen in Figure 44.

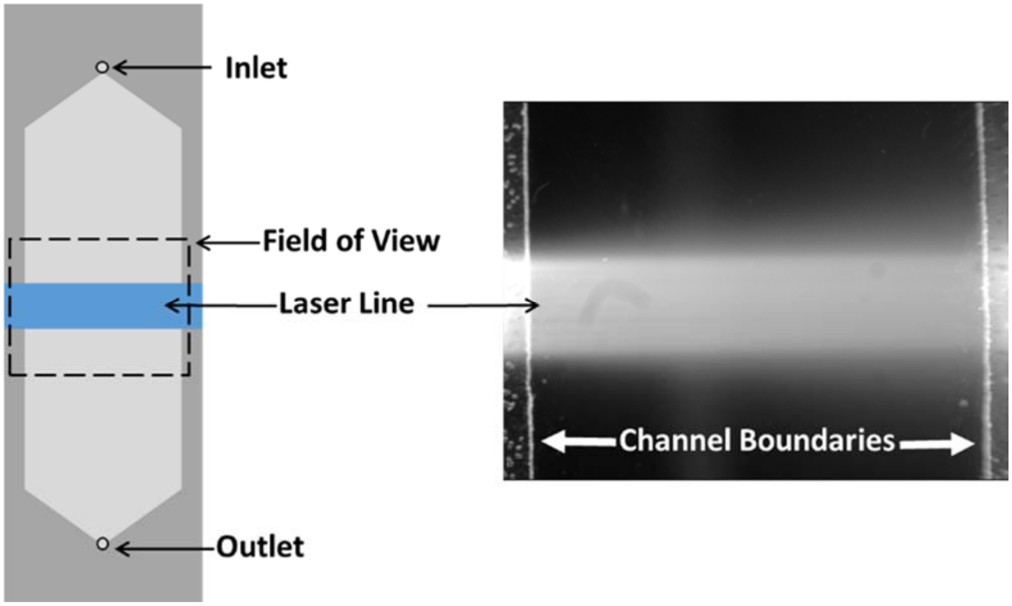

Figure 44 - Optimized wide field flow cell – This flow cell was designed to use the largest fluid volume possible while maintaining the microscope slide format. The excitation laser was injected into the edge of the flow cell in order to form a line of excitation along the width of the channel.

Streak Mode Imaging

One problem which was encountered with the previous method of imaging (conventional high speed imaging, designed to image cells as individual points), was the high frame rates required resulted in video files which were excessively large. A maximum flow rate of 500 μL/min could be used to prevent cell image streaking at 187 fps. At that rate, analysis of a 7.5 mL sample would generate a 50 GB video file comprised of 170,000 individual frames. Analysis and storage of files of that size is currently only a reasonable endeavor for high end desktop computers. As the intention of this endeavor is to develop a platform with application in resource limited settings, the data generated must be usable by hardware which is several generations old and readily available on a used market. By increasing the flow cell volume by a factor of 5, flow rates could be increased by a similar factor. However even at 2500 µL/min, file sizes would be approximately 10 GB each, which would still become unmanageable quickly when performing dozens of tests per day.

To solve this problem we adopted a technique from fluid velocimetry known as streak photography. Developed in the early 20th century, this technique allowed for the measurement of fluid velocities with the then-available low frame rate film cameras. Fluids were seeded with particles, illuminated, and then photographed while in motion. Exposure times and fluid velocities were set such that the illuminated particles formed short streaks in the final images. The direction and relative length of these streaks was used to measure localized fluid motion (i.e. velocity, vorticity, etc).

As described above, the initial purpose of adopting this technique was to reduce the size of data files collected while imaging rare cell samples. It was later found that counting accuracy improved substantially when using this technique. Subsequent analysis and modeling, presented in the following sections, revealed that image SNR is improved significantly in streak-mode images.

7.2.2 Results and discussion

Wide-field cytometer optimization and streak mode advantages

In order to optimize the performance of a wide-field flow cytometer, the following method for setting various device parameters can be used. This will result in maximized cell image SNR, maximized sample throughput, and accurate flow sampling.

First, the distance between the imaging lens and the flow cell should be set such that images of cells are projected onto at most a 3x3 array of pixels. Distance should not be so great that a cell image is less than one pixel in size. At those distances, photon flux per pixel begins to diminish and SNR drops quickly. When cells are imaged on more than one pixel, photon flux per pixel is a constant and independent of the distance between flow cell and lens. The largest possible distance should be chosen in order to maximize field of view (FOV).

Next, average cell velocity should be calculated over a range of flow rates in order to establish this relationship. Velocity can be calculated for a cell moving through the FOV as follows:

$$\dot{X} = \frac{dX}{dt} = \frac{X_n - X_0}{n t_{exp}}$$

Where X is the dimension of the field of view in the direction of motion (units of pixels), X_0 is the initial position of a cell, X_n is the final position after n frames, and t_{exp} is the exposure time. This relationship is shown in Figure 55.

Next, exposure time should be set such that cell image brightness is maximized. For a given average flow velocity and average cell brightness (i.e. photon emission rate), there will be a maximum cell image brightness that can be produced. This is based on the number of photons than can strike a pixel as the cell image passes over it. The minimum exposure time that will yield this maximum image intensity will be the time required for a cell image to traverse a number of pixels equal to its image length (L_{cell}) plus one pixel, or

$$t_{exp} = \frac{L_{cell} + 1}{\dot{X}}$$

Cell diameters will typically be 2-3 pixels based on previously stated recommendations, so total cell image lengths should be 5-7 pixels. This explanation is shown graphically in Figure 45, where a cell of length 3 pixels is seen to move a distance of 4 pixels, thereby producing an image streak with a single bright pixel in its center. An actual cell streak image is shown for a similar cell size and similar flow conditions, along with a plot of actual pixel brightness along the center of the cell streak.

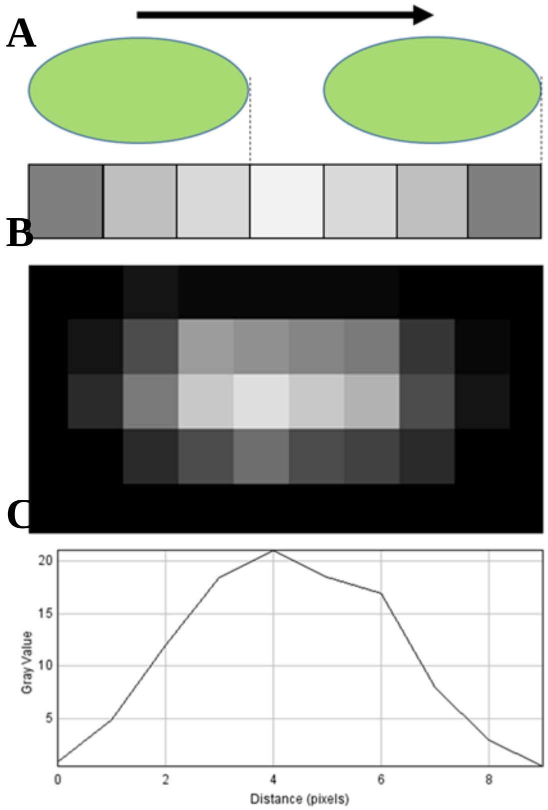

Figure 45 - Relationship between exposure time and maximum pixel brightness – A) Schematic of a cell traversing a number of pixels equal to its length plus one pixel, showing a maximum brightness achieved in the pixel at the image center. B) An actual cell image is shown under these approximate flow conditions, along with C) a plot of its brightness along the center line of pixels.

Exposure time now has a minimum bound. This places a maximum bound on the frame rate:

$$f = \frac{1}{t_{exp}}$$

The minimum bound for frame rate is set by the Nyquist sampling criteria as follows. The average time it takes a single cell to pass through the FOV, the residence time t_r, will be equal to

$$t_r = \frac{X}{\dot{X}}$$

Based on the Nyquist sampling criteria (i.e. sampling frequency must be at least twice the maximum frequency of what is being sampled) the flow must be sampled at a rate of at least

$$f = 2\frac{\dot{X}}{X}$$

If exposure time is set to its maximum (inverse of frame rate), this minimum frame rate does not apply because sampling is essentially continuous and all passing cells will be captured as streaked images. In this case, the lower bound to frame rate must be set empirically based on the frequency of cell arrivals to ensure no overlap of cell path lines. Because of the approximate Poiseuille flow field present in a flow cell such as this, there will inevitably be a distribution of measured cell velocities. Sampling frequency should be set such that the fastest moving cells are properly sampled.

Finally, volumetric flow rate should be set such that the entire distribution of cells is significantly above the noise background of the system (this typically corresponds to an SNR > 5). At higher flow rates image SNR will decrease (explained in greater detail in following sections). Above a certain flow rate, cells at the faint end of the distribution will be indistinguishable from background noise and the average cell count will decrease. In order to set flow rate, a stock solution of fluorescent cells should be prepared and counted beginning at a high flow rate and decreasing until the average cell count per sample reaches a constant value. This maximum flow rate will depend on several factors, including the inherent brightness of cell staining and the excitation photon flux. The parameters of exposure time and frame rate depend directly on flow rate, so these parameters will need to be updated as flow rate is varied.

The lack of performance at low cell concentrations in section 7.1 can now be understood based on these principles. Because exposure time was set arbitrarily to its maximum and flow rate was set such that cells did not produce streaked images (i.e. total cell movement was less than 1 pixel), it can be understood that cell streak brightness was effectively minimized.

Cytometric streak mode imaging concepts and modeling[2]

As in the original velocimetry application, in cytometric streak mode imaging camera exposure times and flow rates are set such that cells form streaked images. As depicted in Figure 46-A, for a given time t and flow rate, a cell will move a distance X. If exposure time is equal to t, the final image will be a streak with length X (Figure 46-ii). If the exposure time is $2t$, streak length will be $2X$, and will have the same average brightness (Figure 46-iii), assuming a constant rate of photon emission from the cell. If exposure time is kept constant and flow rate is doubled, streak length will still be $2X$, but the average streak brightness will be 1/2 (Figure 46-iv). A model for this behavior is fully developed in later sections. It should be noted at this point that streak mode imaging is only

---

[2] Data in this section was collected using a CCD camera (Point Grey Research CMLN 13S2M-CS). This was done because of the exceptionally linear response of the sensor, as well as the predictability of performance of a broad dynamic range. The webcam sensor was found to have a non-linear response, and noise characteristics that were indicative of the data being heavily processed at the hardware level, making development of models based on fundamental photon physics impossible.

appropriate in the case of rare cell detection. In a dense field of fluorescent cells, significant streaking would result in overlap, ambiguous cell images, and incorrect counts.

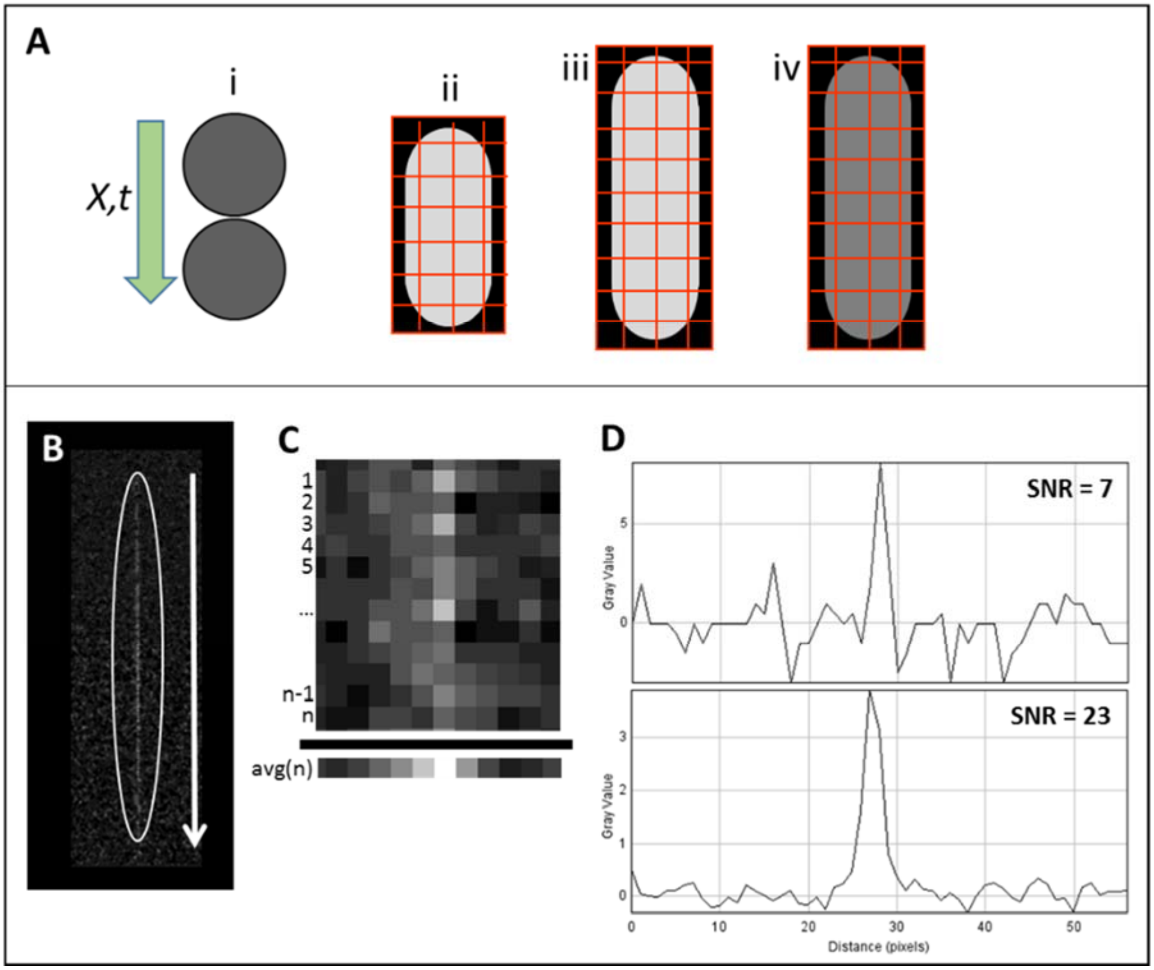

Figure 46 - Streak-mode imaging principles – A) At a given flow rate, cell i) moves a distance X in time t. A image with exposure time t will produce an image similar to ii), and exposure time >t will produce an image similar to iii), a longer streak with similar brightness. If exposure time is held constant and flow rate is increased, a streak similar to iv) will be produced: longer but darker. B) A cell streak image (circled) with flow direction indicated. C) Close-up of cell streak image showing individual pixels and background noise. In order to reduce noise, each column of pixels is averaged over the streak length n to produce a single averaged row of pixels, labeled avg(n). D) A plot of pixel values before and after averaging, showing a 3X improvement in SNR.

The first and most readily appreciated advantage of streak mode imaging for this application is the immediate reduction in data storage requirements. For the presented system, the highest useful throughput condition tested was 10 mL/min with a frame rate of 4 FPS, resulting in file sizes for 7.5 mL samples of approximately 150 MB (or 0.15 GB), a reduction of over 300X from the original high speed imaging case.

The second advantage of streak mode imaging is its potential to improve SNR and lower limit of detection to allow counting of fainter cells. To accomplish this, cell brightness and adjacent background noise values are averaged along the length of the streak as illustrated in Figure 46-B and C. This has the effect of reducing standard deviation in the background noise. This results in improvements in SNR, which is defined as

$$SNR = \frac{\bar{\mu}}{\sigma}$$

Where $\bar{\mu}$ is the average signal and σ is the standard deviation of the noise. In Figure 46-D, a comparison is shown between measuring the SNR of the cell streak shown in B in two ways: first, by measuring the brightest pixel and the standard deviation of the background pixels immediately around it (SNR=7), and second by vertically averaging the 60 columns of pixels around and including the cell streak into a single line image (labeled “avg(n)” in Figure 46-C), and then measuring the brightest pixel and the standard deviation of the averaged background noise (SNR=23).

Figure 47 depicts the relationship between averaging length *n* (i.e. the subset of pixels of a cell streak which are averaged together) and standard deviation based on the formula

$$\overline{\sigma} = \frac{\sigma}{\sqrt{n}}$$

Where $\overline{\sigma}$ is the standard deviation of the averaged pixels, σ is the standard deviation of the raw data, and n is the number of pixels averaged. For the same data set, Figure 48 shows the average measured brightness of a cell streak plotted versus number of averaged pixels, showing the expected asymptotic behavior as the sample mean approaches the population mean. Figure 49, depicting SNR, is the ratio of the two preceding figures. Typical cell streaks show this increasing trend in SNR as n approaches the length of the streak. The conclusion of this data is that the best results are obtained by averaging along the full length of a cell streak.

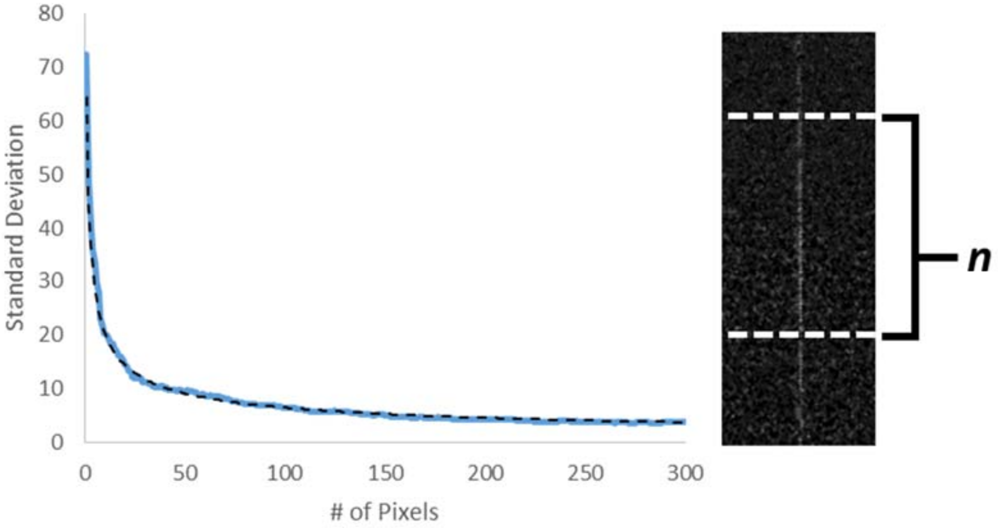

Figure 47 – Relationship between streak averaging length and noise standard deviation – As averaging length n increases, the standard deviation of background noise decreases by a factor of 1/sqrt(n). Sample data is plotted (solid line) with model overlaid (dotted line).

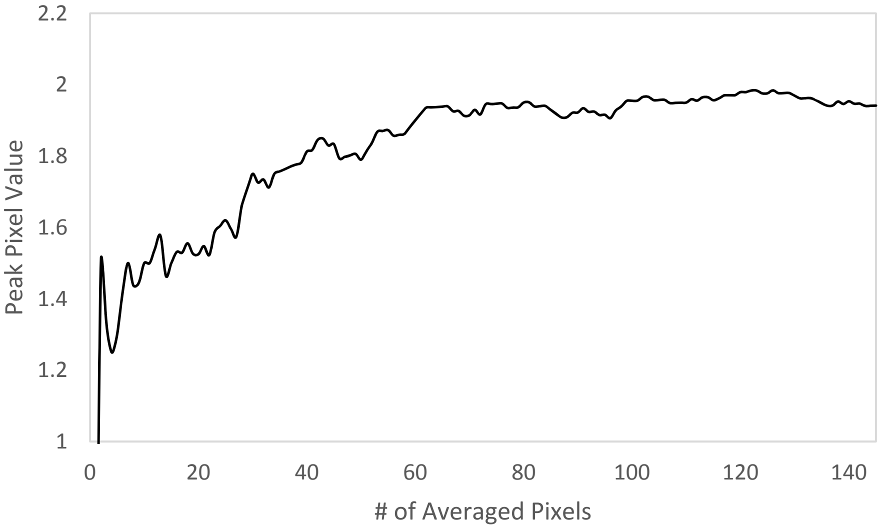

Figure 48 - Effect of averaging on peak pixel value – As averaging length is increased towards the full length of a cell streak, the average peak value approaches a steady state value.

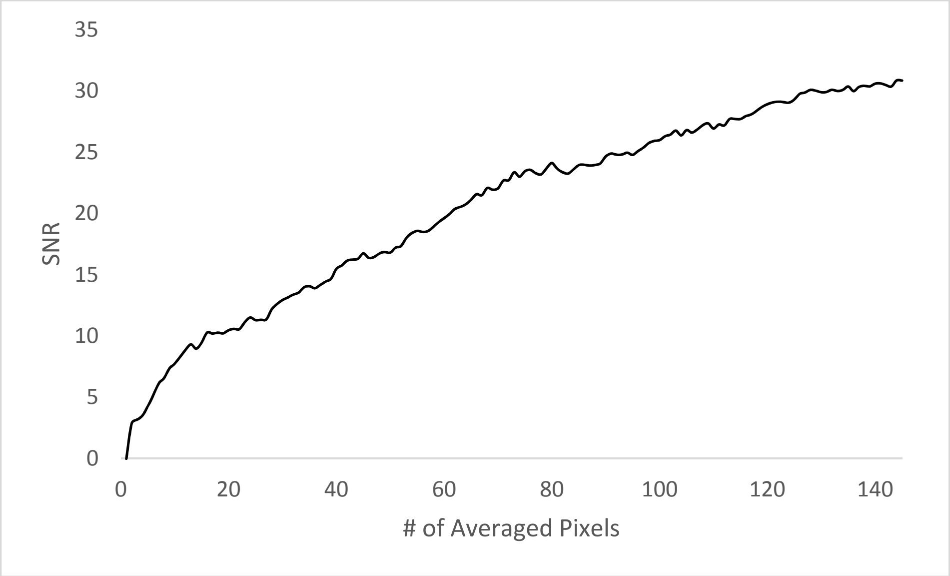

Figure 49 – Effect of averaging length on SNR – As averaging length is increased towards the full length of a cell streak, SNR steadily increases as a result of decreasing background standard deviation.

To aid in visualization of this concept which is fundamental to the proceeding analysis, Figure 50 shows a 3D representation of raw data from a single cell streak. The discrete pixel levels can be seen in the data. An inset image shows the original streak image. Figure

51 is a 3D representation of pixel averaging along the length of a cell streak. Averaging length begins at 1 pixel (i.e. no averaging), and increases in one pixel increments up to the full length of the cell streak (145 pixels in this case). The standard deviation of the background signal can be seen to diminish while the peak value quickly reaches a maximum. This is the fundamental mechanism behind the improvements seen with streak mode imaging.

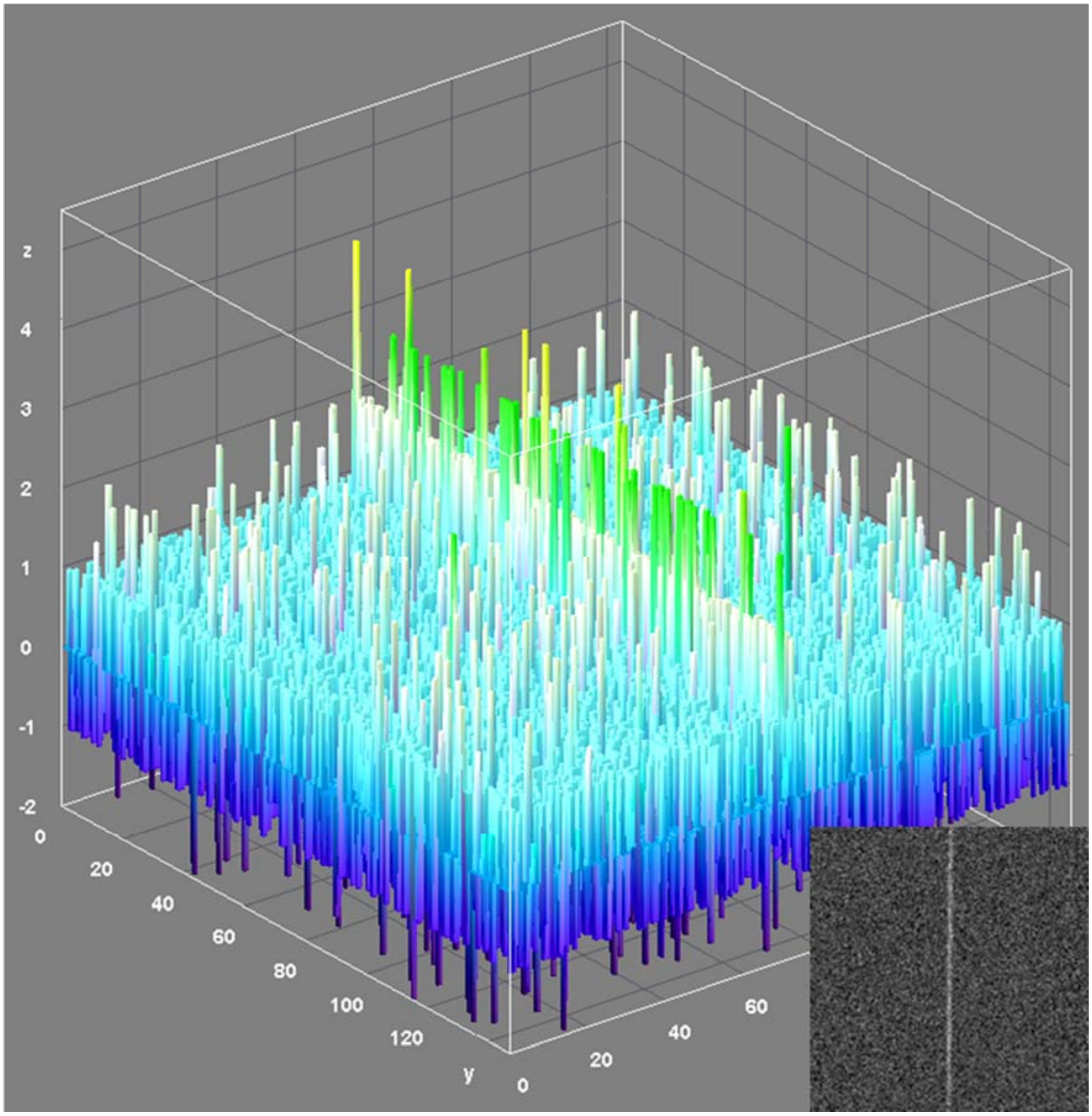

Figure 50 - 3D visualization of raw pixel data from a cell streak – Inset image shows original pixel data. Peak pixel values along the cell streak are between 1 and 2 ADU above peak background noise. Peak SNR = 1.8.

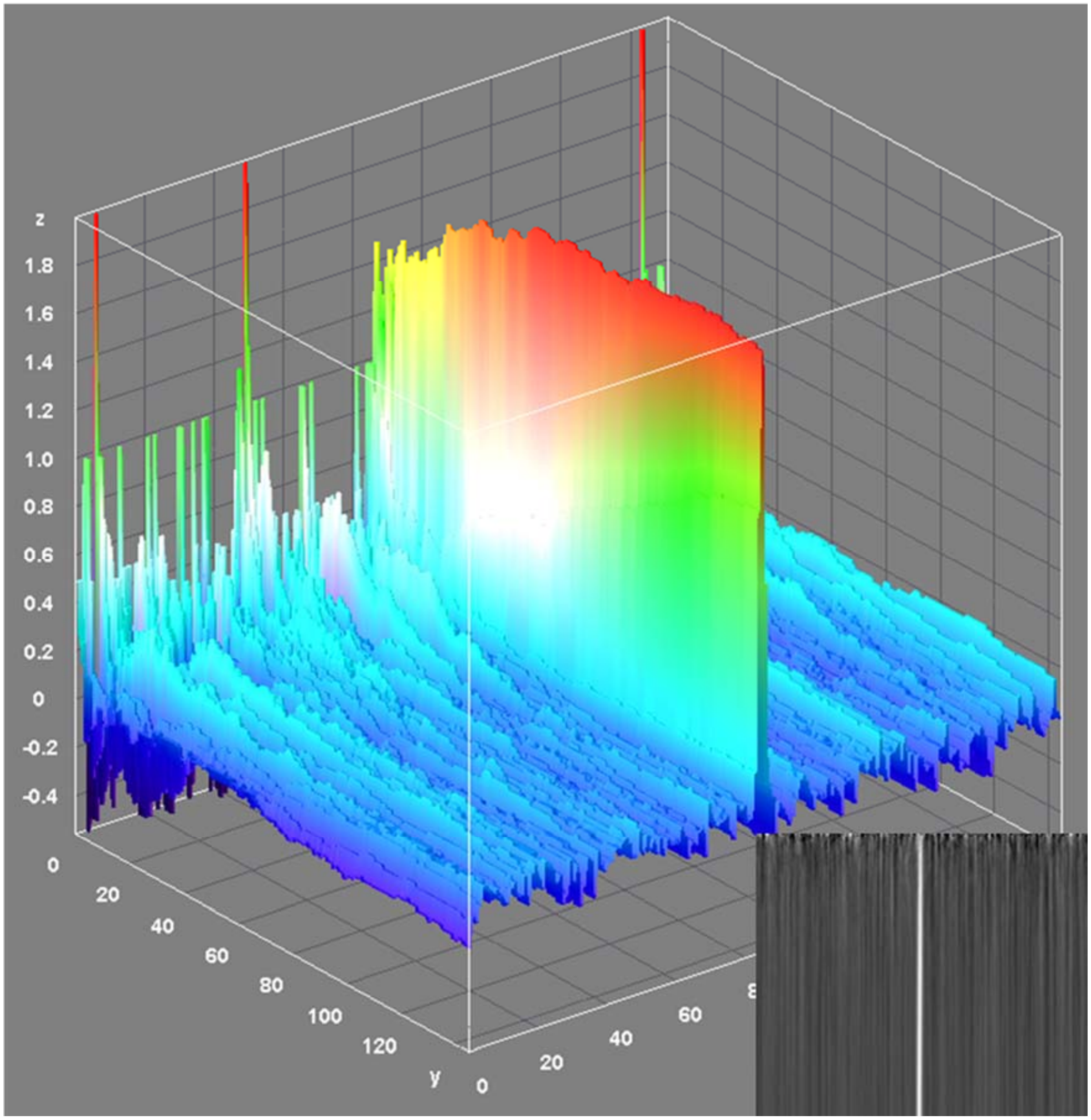

Figure 51 - 3D visualization of increasing SNR with increasing streak averaging length - As streak averaging length is increased, standard deviation of background noise decreases and peak pixel value reaches a steady state. This data was used to create Figure 47 and Figure 49.

It should be noted that there are several factors which influence σ, the standard deviation of the raw pixel data (i.e. the background noise). The largest contributor to background noise in actual flow cytometry experiments was found to be photon shot noise due to autofluorescence of the flow cell substrate material (borosilicate glass). This is similar to results reported elsewhere[202].

Video data processing

Background image subtraction was carried out in a similar manner as described previously, with one minor additional step. A typical background subtraction workflow is seen in Figure 52, where a stack of several hundred images is combined to produce an average background frame which is subtracted from each original image. In this example, two cell streaks which are initially difficult to see in image A become quite apparent in image C.

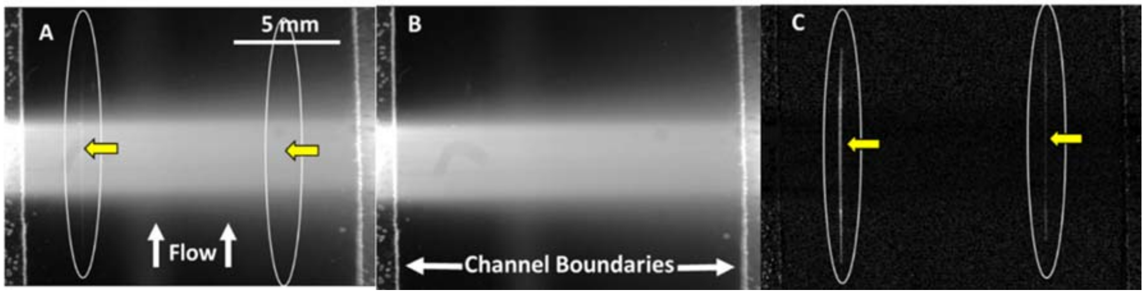

Figure 52 - Streak imaging background subtraction - Raw video frames were background-subtracted to improve cell visibility and allow for accurate SNR measurement. For color CMOS video data, the green channel was extracted to maximize SNR. A) Single raw webcam image of human THP-1 monocytes stained with SYTO-9 dye showing two faint fluorescent cell streaks (circled and marked with arrows) with the bright horizontal band of excitation laser line autofluorescence at the center. B) A frame containing only mean background signal, averaged from several hundred frames. C) The background B is subtracted from A to yield C. This serves to eliminate DC components of the background signal so only random noise remains for accurate SNR measurement.

With sample measurement times of several minutes, it was noted that the background autofluorescent level was noticeably drifting, as seen in Figure 53. This was attributed to a buildup of residue on the inside of the surfaces of the glass flow cell.

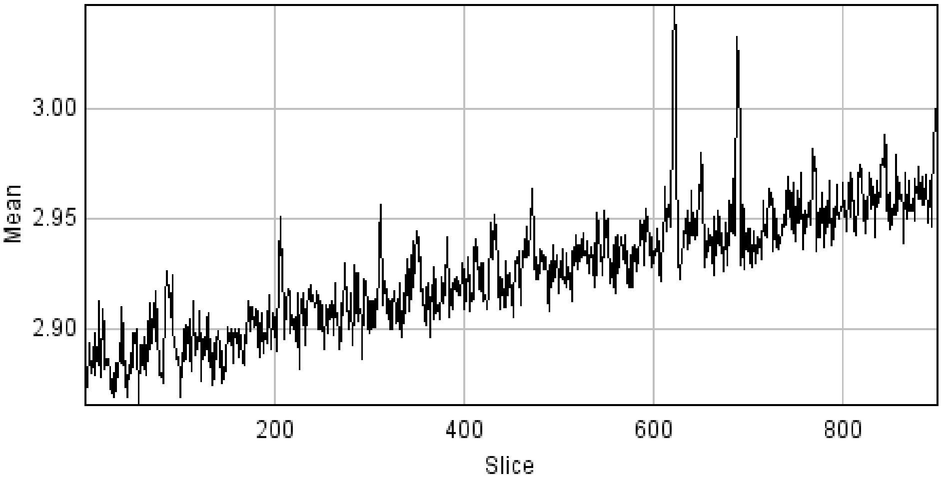

Figure 53 - Flowcell autofluorescence drift - Typical example of background brightness drift during a two minute experiment. Peaks in this data are the result of bright cells passing through the measurement volume.

The result of this drift on image analysis is shown in Figure 54. Image A shows a single raw frame with a faint cell streak embedded in a region of strong autofluorescence. Image B, the average background, is subtracted from A to form image C. The dark spot in the center of image C is caused by a mismatch between the average autofluorescent signal in B and the actual signal in A. Image A was captured very early in the image sequence (image 6 of 900). Because of the linear nature of this drift, image B is only a good match for those frames near the center of the image stack. To account for this, each video frame is calibrated using the 20 frames immediately following it. The result of this method is seen in image D. The averaged streak profiles for the streak shown in iamges C and D are shown in plots E and F, respectively, showing an SNR improvement of approximately 50%.

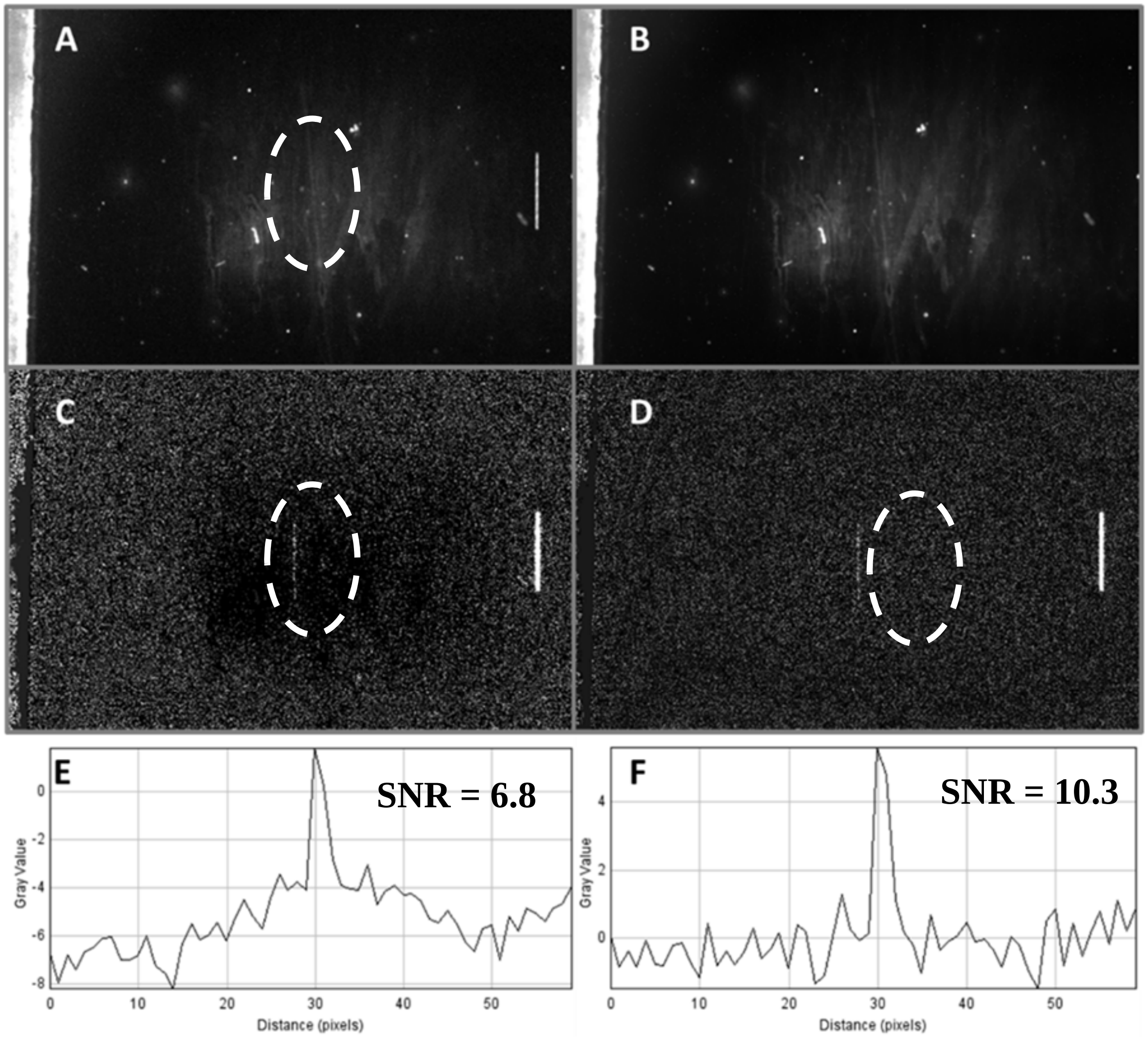

Figure 54 - Autofluorescent drift compensation – A) Single frame with a faint cell streak passing through a bright area of background autofluorescence (streak circled, not easily distinguishable in this image). B) Average background autofluorescent signal for the entire 3 minute experiment. C) Result of subtracting B from A. D) Result of subtracting local median-filtered images instead of a single globally averaged image. E) Averaged streak image from C, showing an SNR of approximately 7. F) Averaged streak image from D, showing an SNR of approximately 10.

Streak image modeling

The following models can be used to guide design of a wide field streak mode fluorescent cytometry experiment. First, the relationship between volumetric sample flow rate and linear particle velocity in the cytometer field of view must be established. Figure 55 demonstrates this measurement in our wide field flow cell. Samples of cells were injected at flow rates between 100 µL/min and 20,000 µL/min (20 mL/min). Streak lengths were measured and divided by exposure time to determine velocity, $\dot{V}$ in units of pixels/s. It was found that there were distinct linear and non-linear ranges of operation. Flow rate and cell velocity were linearly correlated below 1,000 µL/min. Above this speed the relationship became non-linear[3]. For the linear region, a least-squares fit with x-intercept set to zero yielded a relationship of $0.914\,\frac{pixels/_{s}}{\mu L/_{min}}$ (this value will be referred to as C_1).

---

[3] This was attributed to the method of flow cell construction. The two glass microscopes slides were held together by a thin layer of adhesive transfer tape. At elevated pressures, the viscoelastic nature of this tape allowed the depth of the flow cell to increase slowly, increasing the flow cell volume and decreasing the linear velocity.

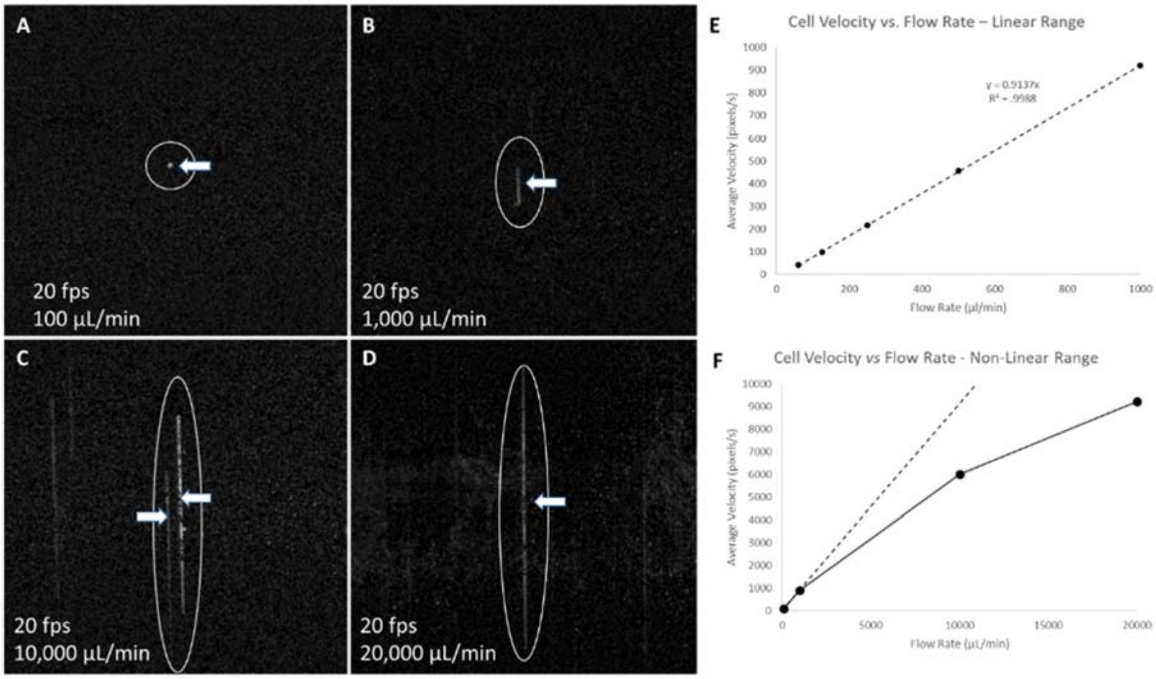

Figure 55 – Cell velocity measurement - A-D) Four images of THP-1 monocytes (marked with arrows) captured at 20 fps (exposure time 1/20 s) are shown with varying flow rates. E) The relationship between average THP-1 velocity and flow rate in the linear range of flow rates, and F) in the non-linear range of flow rates, with the linear trendline from E plotted for comparison. Non-linearity at high flow rates is attributed to viscoelastic creep of the flow cell at increased pressures.

From this same set of data, average pixel values, $\bar{\mu}$, for each cell streak were measured and plotted against flow rate, as seen in Figure 56. The units for the value of a single pixel are ADU (analog to digital units). The units for the average of a group of pixels are ADU/pixel. Multiplying average pixel value by cell velocity $\left(\frac{ADU}{pixel}\frac{pixel}{s}\right)$ yields ADU/s. This is essentially the inherent brightness of the cell being imaged, if the cell is thought of as emitting ADU instead of photons. From the collected measurements of cell streak brightness and cell velocity, values of ADU/s for each measured cell can be calculated (call this C_2; its average value was 3070 ADU/s in this data set). The result will be a distribution from which a median value can be calculated. The model to predict average streak brightness is then $\bar{\mu} = \frac{C_2}{C_1 \dot{V}}$ which is the dotted line plotted in Figure 56.

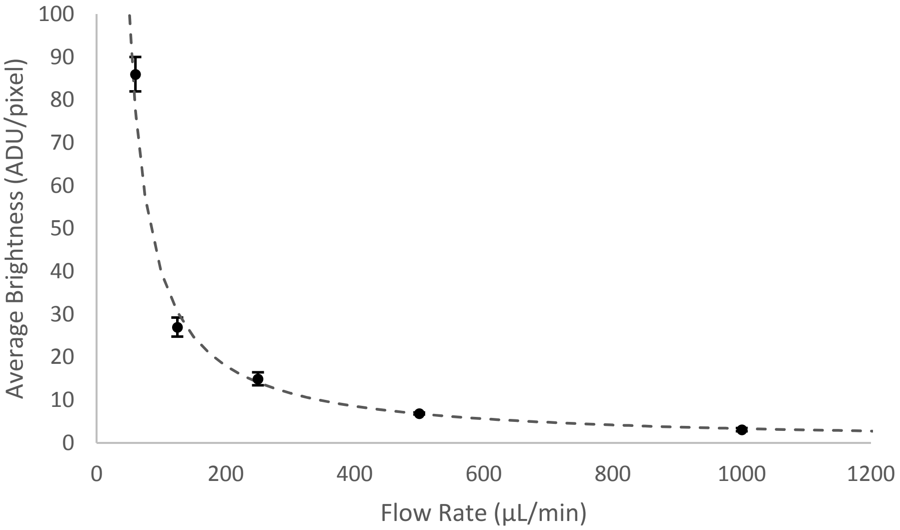

Figure 56 - Cell Streak Brightness Modeling – The relationship between flow rate and cell streak brightness is shown. Predicted brightness values, based on measured cell photon emission rates, is also plotted (dotted line).

While average streak brightness is strongly linked to flow rate and the rate of cell fluorescence, it is essentially uncorrelated to exposure time. Plots of the relationship between average streak brightness and exposure time are shown in Figure 57. This is the result of the approximately constant velocity of cells at each flow rate. Error bars show the standard error in each measurement. Measurements represent the median value of many (>100) cell streak measurements. Actual distributions are shown in Figure 61.

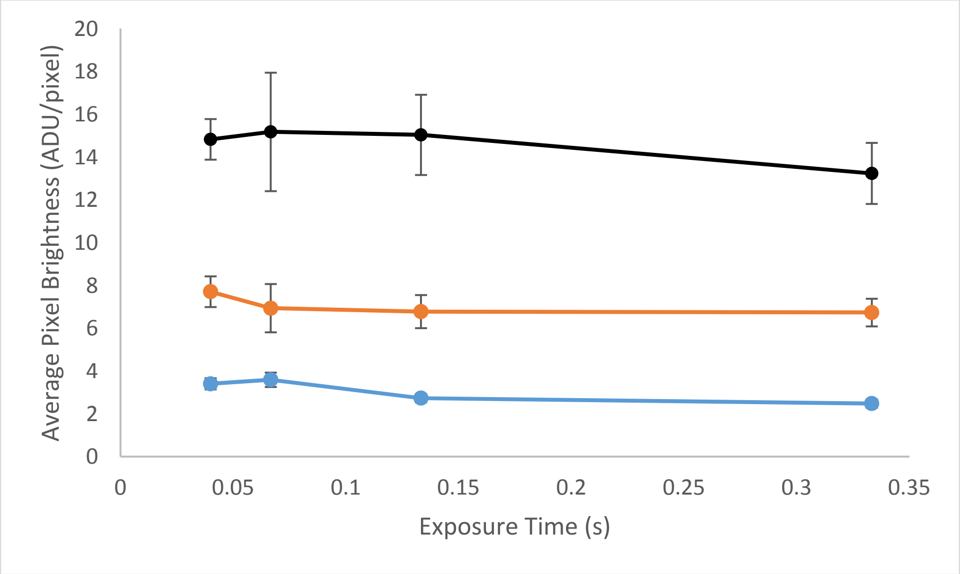

Figure 57 - Relationship between streak brightness and exposure time - Average pixel values for flow rates of 1000, 500, and 250 µL/min (solid, dashed and dotted lines, respectively) are shown for a range of exposure times.

Factors governing image SNR

Pixel standard deviation was found to be strongly correlated to exposure time. This is caused by the autofluroescence of the flow cell material (borosilicate glass). A duplicate of the flow cell pictured in Figure 44 was made using fused quartz microscope slides in order to experiment with ultra-low autofluorescence. The autofluorescence of the glass slide can be seen in Figure 52 (the path taken by the laser as it propagates through the glass can clearly be seen). The quartz flow cell was used for the experiments in Figure 54. The bright horizontal band is noticeably absent. The only noticeable autofluorescence in that image is due to the buildup of residue on the interior surfaces of the flow cell. The relationship between pixel standard deviation and exposure time is presented in Figure 58 for both materials.

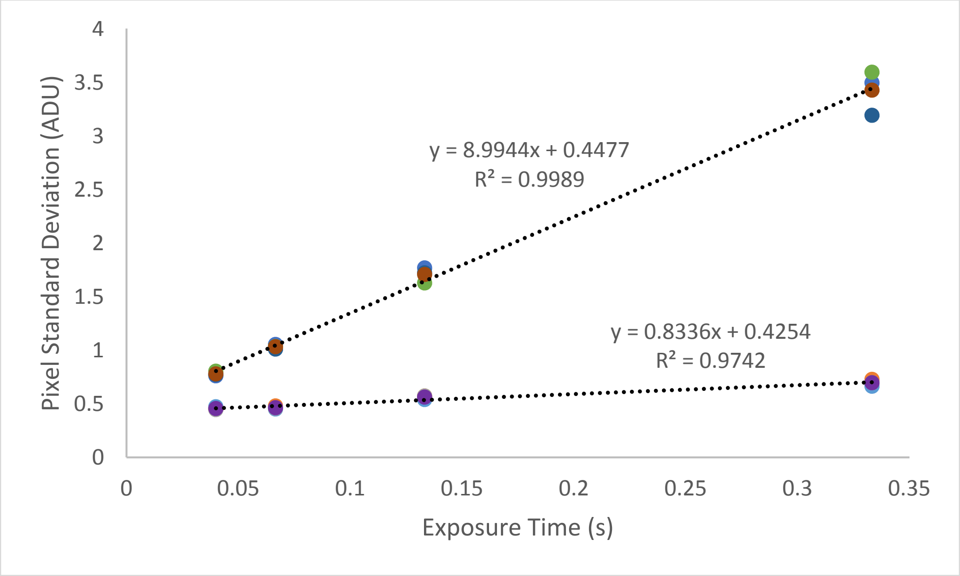

Figure 58 - Relationship between spatial pixel standard deviation and exposure time – Standard deviation of pixels in the interrogation region of a borosilicate glass flowcell (lower data set) and a fused quartz flowcell (upper data set). Data is shown for four flow rates (1000, 500, and 250 µL/min, data overlapped), along with an average linear trendline. The increasing trend in standard deviation with exposure time is due to the constant rate of arrival of autofluorescent photons.

The slope of each trendline shows the rate at which pixel standard deviation increases. It can be seen that for the glass flow cell (steeper curve), this rate is approximately ten times higher than for the quartz flow cell. This corresponds to an average arrival rate of autofluorescent photons which is approximately 100 times higher (due to the Poisson nature of photon arrival rates). The effect that this has on streak SNR is modeled in Figure 59 for both materials, including a plot of the ideal case for zero autofluorescence. Figure 60 shows data collected using the quartz flow cell at four different flow rates with models overlaid. Error bars represent the standard error in these brightness measurements, which is the result of sampling from a population. The equation for SNR in these models is given by

$$SNR = \frac{\bar{\mu}}{\sigma_{sensor} + t_{exp} R_{\sigma}}$$

where $\bar{\mu}$ is the average streak brightness based on the model presented in Figure 56, σ_{sensor} is the standard deviation resulting from the sensor read noise (for short exposure times this value is essentially fixed, and was equal to ~0.43-0.44 ADU for the PGR CCD camera, as seen in the y-intercepts of the linear regressions in Figure 58), and R_{σ} is the rate at which standard deviation increases (the slope of the linear regressions in Figure 58).

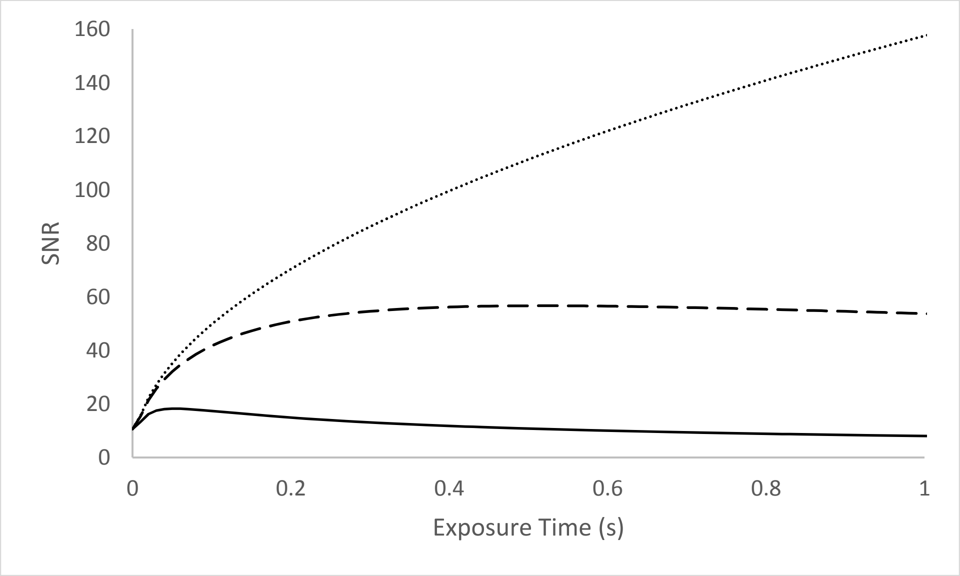

Figure 59 - Effect of flow cell autofluorescent intensity on streak SNR – Models for SNR are presented for an ideal case with zero autofluorescence (dotted line), the case of a quartz flow cell producing an autofluorescent signal of approximately 0.7 ADU/s (dashed line) and a borosilicate glass flow cell with ~80 ADU/s (solid line). These plots are for a given flow rate and cell photon emission rate.

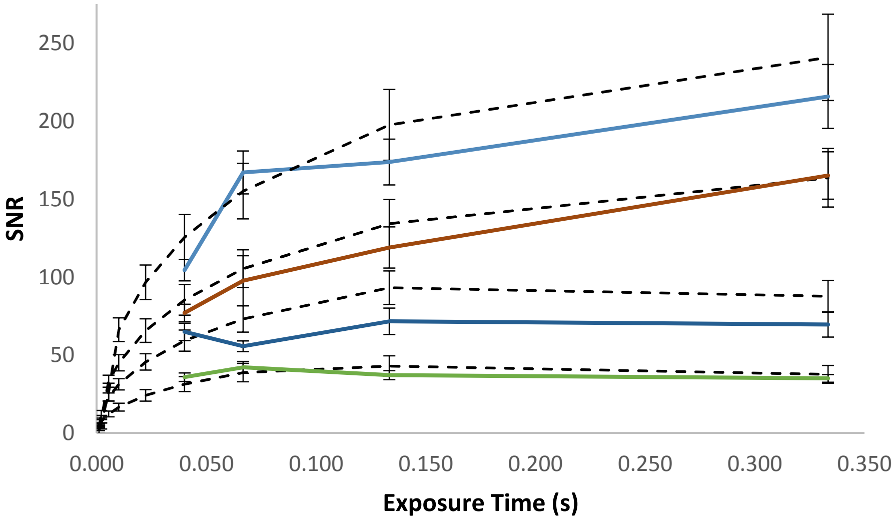

Figure 60 - Cell streak SNR modeling – The relationship between exposure time, flow rate and SNR is shown along with a predictive model (dotted lines). Four sets of data are shown for four different flow rates (1000, 500, 250, 125 µL/min). The data set with the fastest flow rate shows the lowest SNR, and that with the slowest flow rate shows the highest SNR. The SNR plateau effect seen most clearly in the lowest two data sets is due to increasing accumulation of autofluorescent noise photons at longer exposure times.

Improving cell distribution resolution in the presence of quantization error

Streak mode imaging can be used to extract more complete data about a distribution of cells that would be possible with conventional imaging. The mechanism behind this is performing streak averaging at bit depths above the native camera bit depth (native bit depth is 8 bits for both the CMOS webcam and CCD camera used). For operating conditions that yield cell images with average streak image brightness that is near the low end of the sensor (i.e. 1-10 ADU), fine resolution of the distribution is lost due to quantization error.

To illustrate the problem of quantization error, consider two stationary cells imaged by an 8-bit sensor (pixel value ranges from 0-255). Cell 1 emits an average of 3.9 photons per second, and cell 2 emits an average of 4.25. Assume for the moment that one photon striking a pixel produces an increase in pixel brightness by 1 ADU. If the two cells are imaged for one second, the expected value is equal to their average emission rate. However, because photon emission rates follow a Poisson process the actual recorded values will vary with a standard deviation equal to the square root of the average value (approximately 2 ADU for each cell). If many images are recorded and their average is measured in the native 8-bit format of the camera, both cells will show an average value of 3 ADU because 8 bit pixel values can only take on whole numbers, and will be rounded to the nearest value by the camera’s analog to digital converter. If averaging is instead carried out at a higher bit depth (using 32-bit float, for example), the average of each cell would be very close to its true average (arbitrarily close for a large number of samples).

Each cell streak image is a record of that cell’s photon emission rate over time. Therefore if the average pixel value of each streak is measured at a higher bit depth, a more accurate measurement of that cells intrinsic brightness can be obtained. Increasing bit depth from 8 to 16 allows for an improvement distribution resolution of 256X. This much resolution may not be necessary in most cases, but with modern computers the improvement comes at very little cost in additional computation time.

Distribution Normalization: Representing cell distributions based on photon emission rate

For streak data which has been processed at in increased bit depth as described in the previous section, an additional step is possible which will allow for sets of data collected under varying flow or exposure time parameters to be directly compared. Figure 61 shows nine sets of data for three flow rates and three exposure times. Data is presented as histograms, with average streak pixel value on the horizontal axis and the number of cell counts on the vertical axis. At the highest flow rates, a single peak is seen at the low end of the histogram (below 5 ADU in each case). As flow rate decreases in each data set (i.e. moving from chart 1 to 2 to 3, 4-5-6 or 7-8-9), the mean pixel value of this population of cells increases, peak height decreases and peak width increases. This moving up and spreading out behavior is the result of a population with an inherent distribution being quantized into an increasingly large number of bins. Slowing the flow rate down has the same effect as averaging several images together: more photons are sampled from the population, so a more accurate measurement of the true distribution of cells is seen. Because the data presented in Figure 61 has not been normalized with respect to flow rate, it is difficult to directly compare plots.

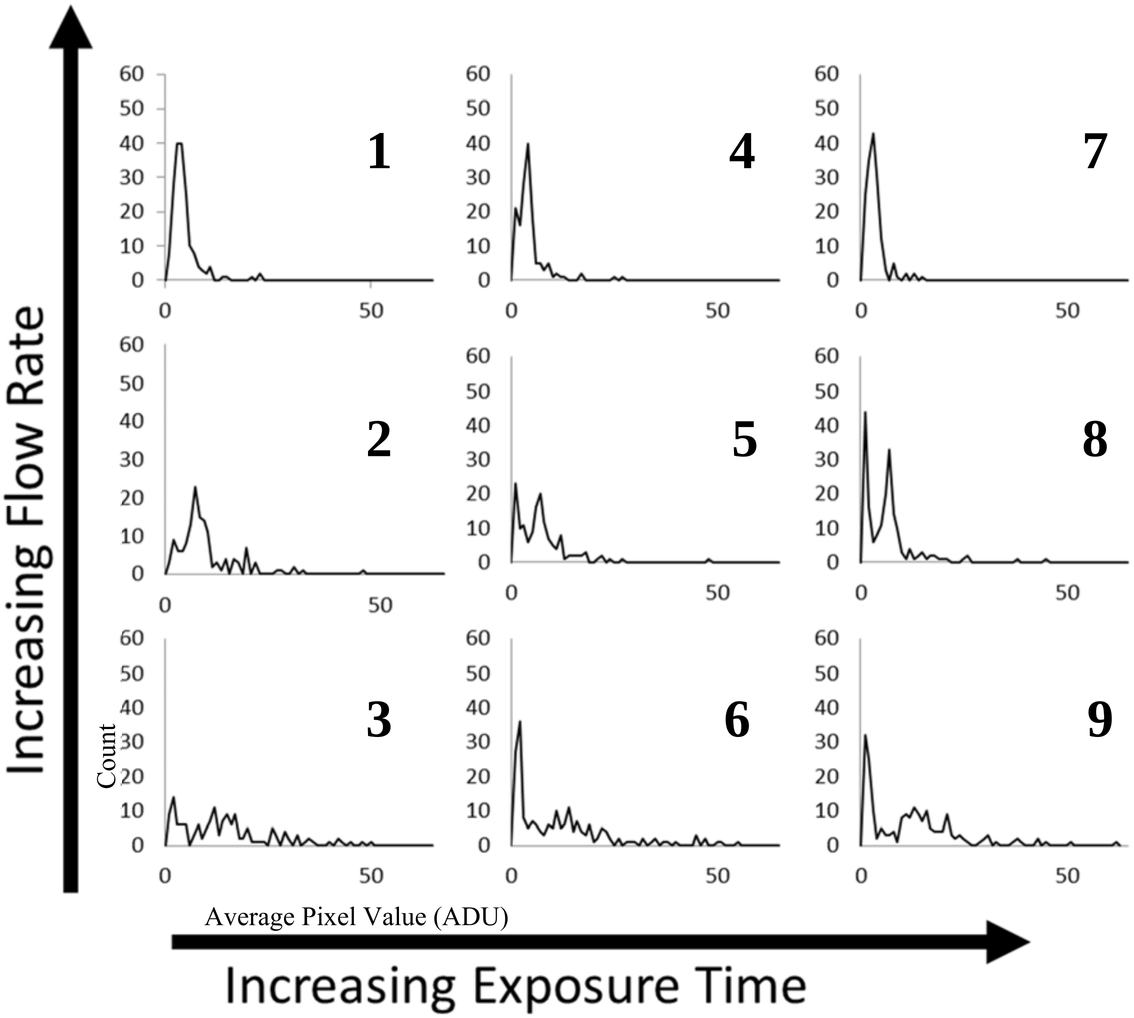

Figure 61 - Visualizing cell populations using pixel values – Two populations of cells, one bright and one faint, were counted using three flow rates (250, 500, 1000 μL/min) and three exposure times (0.04, 0.067, and 0.13 s). At the highest flow rates, only the brightest population (a single distinct peak) is visible). As flow rate decreases, the number of photons collected per pixel increases, and the faint cell population becomes visible as a peak at the left end of the X-axis. The bright cell population shifts up along the X-axis, its peak height drops and it spreads out.

In Figure 62, pixel values in units of ADU have been converted to relative photon emission rates in units of photons/second. This is essentially normalizing the data with respect to flow rate. When presented in this way, the center value of a given population of cells does not drift with changing flow rate as seen in Figure 61. Instead what changes are the relative heights of each population's peak as the system becomes more sensitive with decreasing flow rate and increasing exposure time.

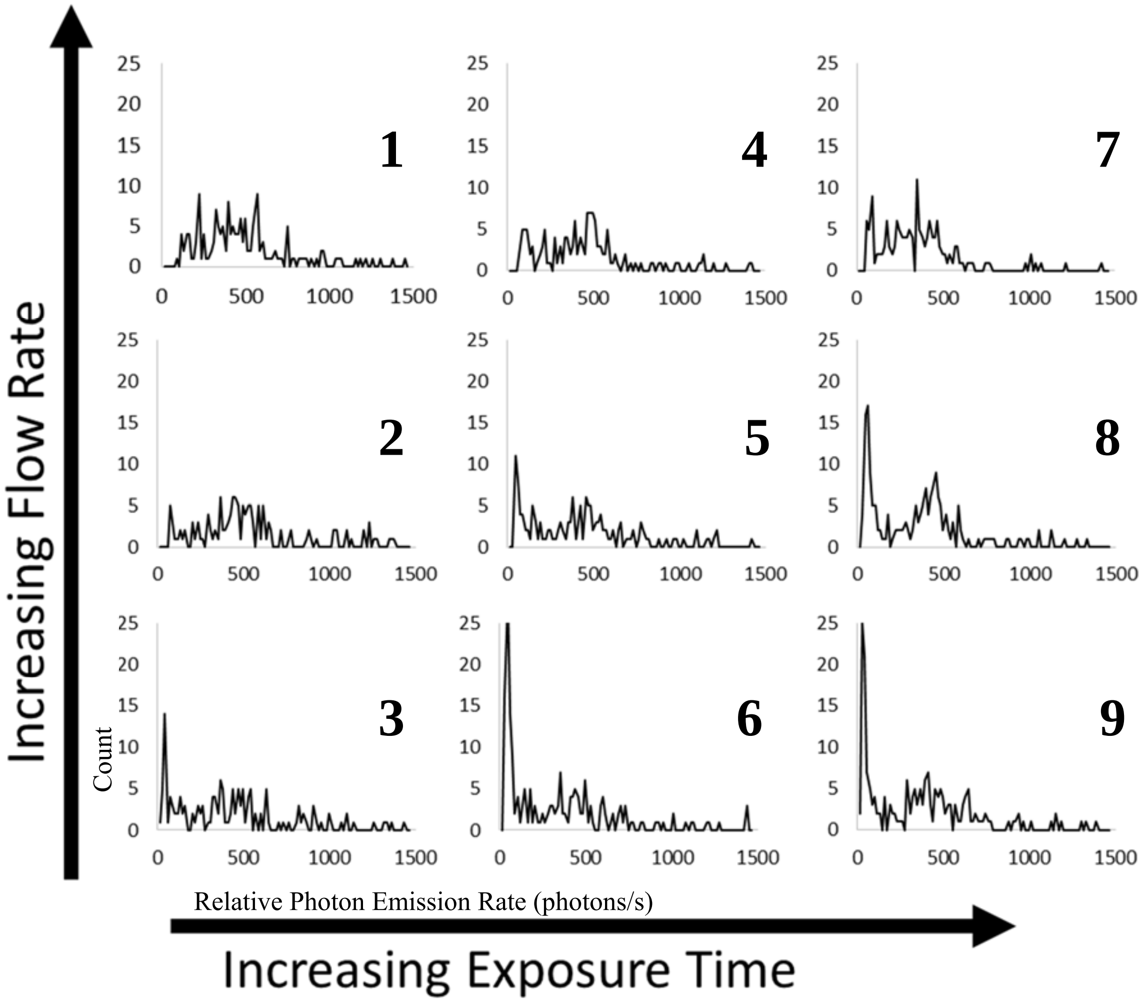

Figure 62 – Visualizing cell populations with photon emission rate – The same data set as presented in Figure 61, but with X-axis values converted from pixel value to photon emission rate. This set of histograms represents distributions of detected cell brightness independent flow parameters and camera settings: the locations of the two cell populations does not shift based on flow rate or exposure time. As flow rate decreases and/or exposure time increases, overall sensitivity increases as evidenced by the increasing peak of faint cells at the left end of the X-axis.

As previously noted, there was found to be a secondary population of cells which did not show nuclear staining and had correspondingly low brightness values. As system sensitivity was increased (by lowering flow rate and increasing exposure time), the limit of detection was lowered and this population of cells could be counted. In Figure 62 this is seen as the appearance and increase in height of a peak at the far left end of the horizontal axis, showing a relative photon emission rate of approximately 30-50 photons/s, compared to the average rate of the bright THP-1's with rates of ~400-450 photons/s.

The conversion between average pixel value and relative photon emission rate is accomplished in three steps: 1) conversion of average pixel value to rate of pixel value accumulation in units of ADU/s (described previously in *Streak image modeling*), 2) conversion of ADU/s to electrons/s via the camera photon transfer function method, and 3) converting electrons/s to photons/s with the estimated camera quantum efficiency.

The photon transfer function method was developed and popularized by James Janesick in the mid 1980's[215]. It is uniquely useful for characterizing the performance of image sensors in that no specialized equipment is required other than the camera itself. The technique relies on the Poisson nature of photon arrival rates to measure the relationship between the average pixel value recorded by a camera sensor and the average number of photons that were recorded by each pixel.

What follows is an abridged version of the method. Images of a uniformly illuminated surface are recorded in pairs at exposure settings covering the linear range of sensor operation. The mean pixel value of each pair is recorded. Then for each pair, one image is subtracted from the other and the variance of the resulting image is measured and divided by two[4]. A plot is made with mean pixel value on the vertical axis and variance/2 on the horizontal axis. The slope of the resulting line, m, is the conversion factor between ADU and electrons:

$$\#e^{-} = m \cdot ADU$$

A plot of three photon transfer curves measured for the Point Grey Chameleon camera are shown in Figure 63. Three different gain settings were used to illustrate the effect of gain on measured streak brightness. It should also be noted that the relationship between the camera gain settings and the measured electron conversion factor agree fairly well (within 0.5 dB).

---

[4] The two images are subtracted in order to remove any non-random sources of variance. Each image represents a sample from the same Poisson distributed variable (the photon arrival rate) which has mean and variance equal to λ. When the difference of two Poisson variables is taken, the resulting variable is described by a Skellam distribution, the variance of which is the sum of the variances of the two original Poisson variables (2λ). For the variance of the difference image to be properly correlated to the mean of the original images, it must be divided by 2.

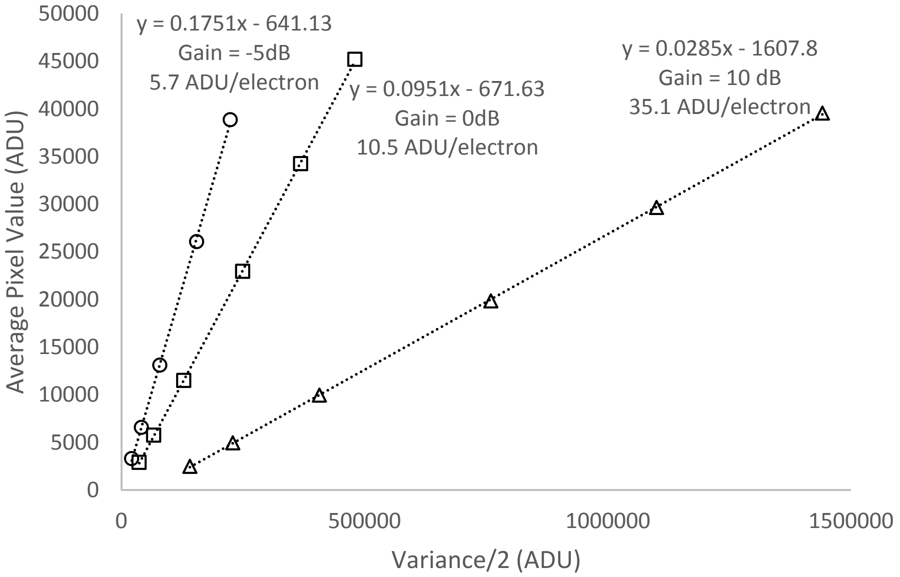

Figure 63 – Measured photon transfer functions for Point Grey Research CMLN 13S2M-CS CCD camera – Photon transfer functions measured at three gain settings (-5, 0, and +10 dB). The inverse of the slope of each linear fit is the number of ADU a pixel will increase by for each photo-electron generated.

To convert electrons per second to photons per second, published data on sensor or camera quantum efficiency can be used if available. Figure 64 shows an example plot for the Point Grey Camera used. The final rate of photons / second should not be considered a measurement of what a cell is actually yielding. It is only a tool to compare relative emission rates of different cell populations, or the relative sensitivities of different cameras which may be used. Various other system parameters will affect the number of photons that actually reach the sensor (such as the excitation source power, the design of the flow cell, the emission filter profile and the imaging lens being used).

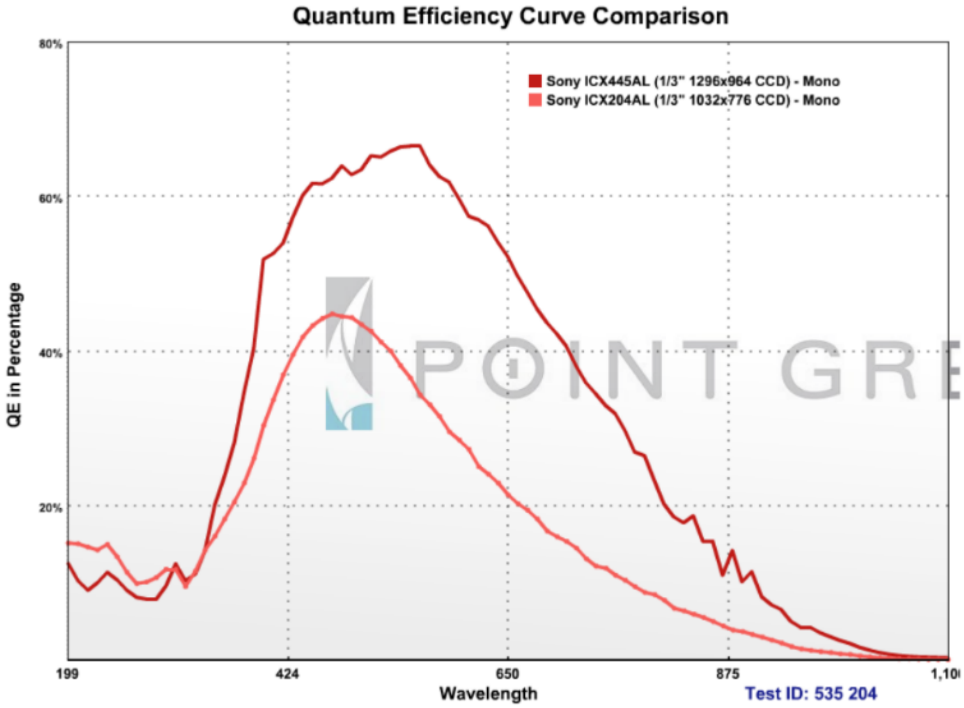

Figure 64 - Published quantum efficiency curve for PGR CMLN camera – Measured camera quantum efficiency curve for the PGR CMLN camera (upper curve, using Sony ICX445AL sensor). To convert between numbers of photo-electrons and approximate numbers of incident photons, divide number of photo-electrons by quantum efficiency (image source: http://ww2.ptgrey.com/USB2/chameleon).

Rare cell counting with optimized wide field cytometer

After optimization of flow cell geometry, the flow cytometer was equipped with the CMOS webcam and a borosilicate glass flow cell to test its rare cell counting capability with the lowest cost component configuration. Previous results at concentrations of 100 and 10 cells/mL yielded acceptable counting efficiencies, so only lower dilutions were repeated. Samples of cells at 1 cell/mL and 0.1 cell/mL concentrations were analyzed in batch sizes of 30 mL with flow rate set to 10 mL/min and frame rate 4 fps. Cells were prepared in a manner identical to those counted by the previous design of cytometer. Their location on the dye diffusion curve is similar to those presented in Figure 43 in order to allow for comparison between the two sets of data. Figure 65 shows the results of these experiments. Predicted stock concentrations (sparsely filled columns). Cytometer results are shown (densely filled columns) for the average concentration measured over all samples. For the stock solution of 1 cell/mL, a standard error of 0.082 was calculated (95% confidence interval: C_{95} = 0.84-1.16 cell/mL). For 0.1 cell/mL, the standard error of the stock solution was 0.003 (C_{95} = 0.094-0.106).

For the target of 1 cell/mL, an average concentration of 0.91 cell/mL was measured, with a standard error of .03 (C_{95} = 0.85-0.97). For the target of 0.1 cell/mL, an average concentration of 0.083 cell/mL was measured, with a standard error of 0.01 (C_{95} = 0.065 – 0.102).

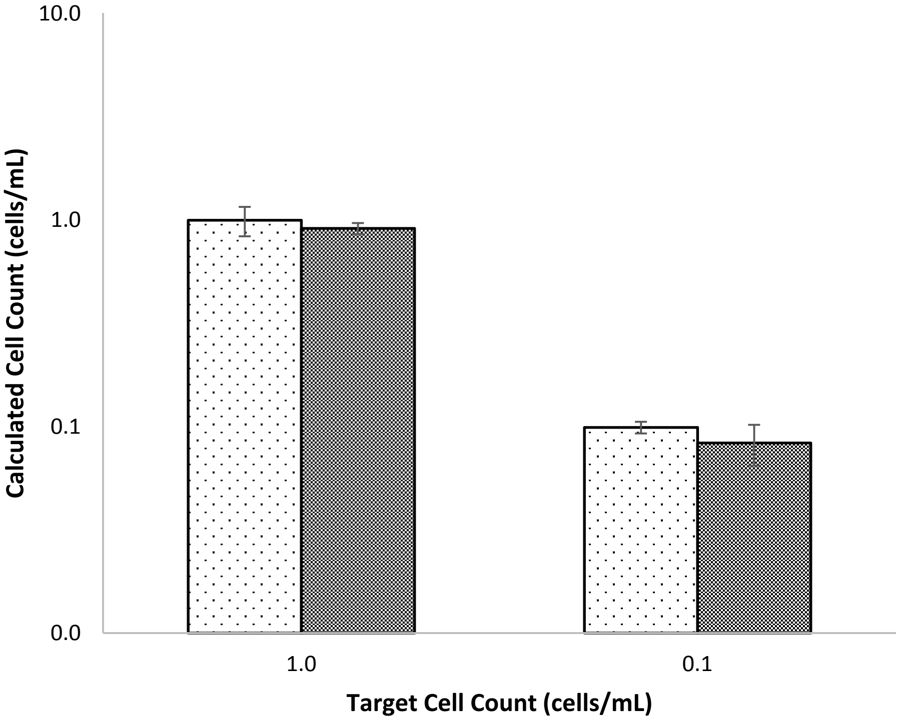

Figure 65 - Webcam-based wide-field flow cytometer counting efficiency - Results of two concentrations of human monocytes counted via microscopy (sparse fill) and using the optimized webcam-based flow cytometer operating in streak mode (dense fill). Error bars represent a 95% confidence interval for each data set. Manual counting was performed at a higher stock concentration (1000 cells/mL) and the results for each target concentration were calculated following serial dilution.

Figure 66 A and C show distributions of measured cell concentrations per sample for the both 1 and 0.1 cell/mL cases. For each data set a Poisson distribution is plotted with λ set equal to the target mean concentration. Both cases show reasonably good fits with theory. Plots B and D show the spacing in time between cell arrivals for each case, along with an exponential distribution with λ set equal to the expected average arrival frequency for each data set (1/6 and 1/60 Hz for the 1 and 0.1 cell/mL cases, respectively). Plot B, the case of 1 cell/mL, shows excellent agreement with this model. This is likely due to the 737 cell counts which comprise this data. The data behind plot D is composed of only fifty cell counts, resulting in greater noise.

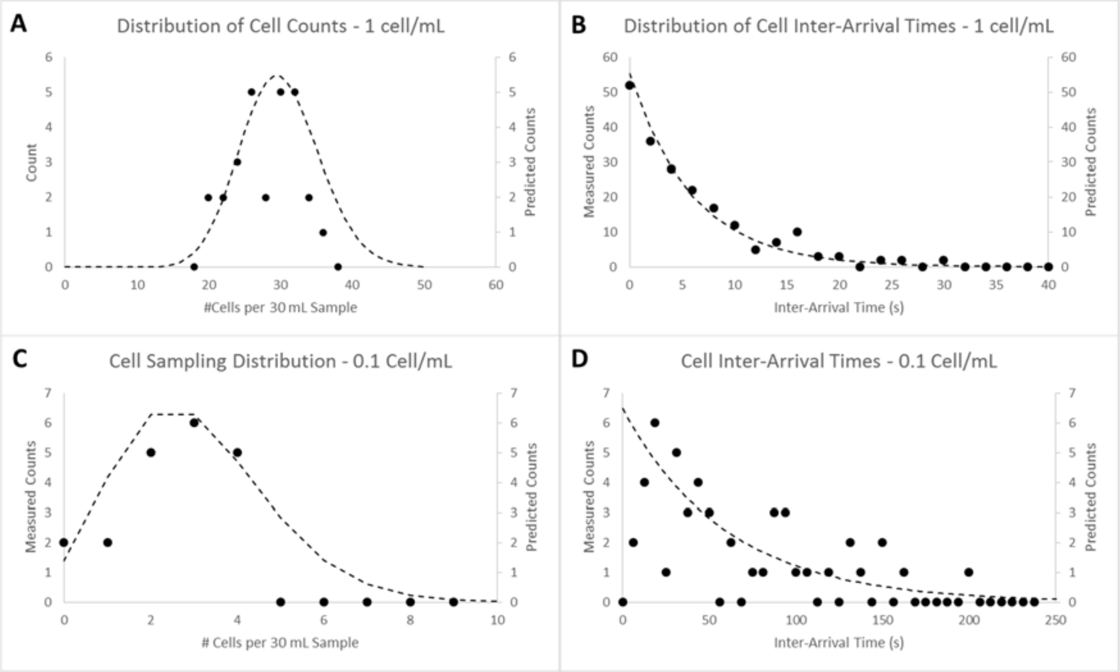

Figure 66 - Rare Cell Detection Modeling - A) Histogram (bin size = 2) of cell counts for a 1 cell/mL stock concentration of THP-1 monocytes measured using streak-mode imaging. A total of 27 samples were taken 30 mL at a time and yielded an average cell count of 27.3 cells/sample. A total of 737 cells was measured in this data set. The probability density function of a Poisson distribution with λ equal to the predicted population average of 30 cells per sample is shown (dotted line). B) Histogram of inter-arrival times for cells (same data set as Plot A). Average inter-arrival time was 6.89 s. An exponential distribution with parameter λ = 6 (the predicted population average) is overlaid (dotted line). C) Histogram of cell counts for a 0.1 cell/mL stock concentration with model Poisson distribution (λ=3). A total of 20 samples were taken 30 mL at a time and yielded an average cell count of 0.83 cells/sample. A total of fifty cells was measured in this data set. D) Histogram of inter-arrival times for cells (same data set as Plot C). Average inter-arrival time was 72 seconds. An exponential distribution with parameter λ = 60 is overlaid (dotted line).

These results indicate that a properly optimized wide field flow cytometer is capable of accurate high throughput counting of rare cells. For a given flow cell geometry, actual throughput rates are directly dependent on the achievable brightness of a fluorescently labeled cell. Inherently dimmer cells will require lower flow rates. Achievable cell brightness depends on many factors including labeling methodology and fluorophore quantum yield.

8. Scientific and technical contributions

8.1 Microscale collimation technique for microfluidic devices

A technique for designing and optimizing optical Söller collimation devices was described based on the requirements of a microfluidic fluorescence detection platform. Based on these design requirements, a low cost lens-free collimator was developed and demonstrated to be effective in LOC fluorescence measurements. The proof-of-principle device was benchmarked against a commercial plate reader using a FRET-based liquid phase assay for BoNT-A activity. Both platforms achieved a limit of detection of 1.25 nM.

Publications:

Balsam, J., Ossandon, M., Kostov, Y., Bruck, H. A., & Rasooly, A. (2011). Lensless CCD-based fluorometer using a micromachined optical Söller collimator. *Lab on a Chip*, *11*(5), 941-949.

Balsam, J., Ossandon, M., Bruck, H. A., & Rasooly, A. (2012). Modeling and design of micromachined optical Söller collimators for lensless CCD-based fluorometry. *Analyst*, *137*(21), 5011-5017.

8.2 mHealth application based model for low-cost fluorescence detection

A technique for using low cost consumer grade light sensors for high sensitivity biological measurements was developed based on time-domain signal averaging through image stacking. This technique enabled the detection of fluorescent signals at the same level as a conventional plate reader, with an equipment cost of nearly 1,000 times less. To determine the effect of this technique on the quantitative measurement of fluorescent signals from liquid-phase fluorescent assay products, serial dilutions of fluorescent dye were measured to determine LOD and the results were compared to an identical experiment conducted with a commercial plate reader. Both platforms achieved a limit of detection of 30 nM, indicating that the developed method is suitable for quantitative measurement of low intensity fluorescent assays.

Publications:

Balsam, J., Bruck, H. A., Kostov, Y., & Rasooly, A. (2012). Image stacking approach to increase sensitivity of fluorescence detection using a low cost complementary metal-oxide-semiconductor (CMOS) webcam. *Sensors and Actuators B: Chemical*, *171*, 141-147.

Balsam, J., Ossandon, M., Bruck, H. A., Lubensky, I., & Rasooly, A. (2013). Low-cost technologies for medical diagnostics in low-resource settings. *Expert opinion on medical diagnostics*, *7*(3), 243-255.

8.3 Technique for amplification of liquid-phase fluorescent assay products based on capillary waveguide excitation with mHealth applications

A technique was developed for improving LOD of liquid-phase fluorescent assays by improving efficiency of excitation and collection of emitted photons via use of capillary waveguides. Based on this technique, a proof-of-concept mHealth platform was developed based on a mobile phone camera as a detector. Benchmarking was conducted using unbound fluorescent dye (fluorescein), as well as with a fluorescent assay for adenovirus. Using a cell phone camera as the photo detector, sensitivity near that of conventional methods was demonstrated using 10X smaller sample volumes.

Publications:

Balsam, J., Bruck, H. A., & Rasooly, A. (2013). Capillary array waveguide amplified fluorescence detector for mHealth. *Sensors and Actuators B: Chemical*, *186*, 711-717.

Balsam, J., Rasooly, R., Bruck, H. A., & Rasooly, A. (2014). Thousand-fold fluorescent signal amplification for mHealth diagnostics. *Biosensors and Bioelectronics*, *51*, 1-7.

Balsam, J., Bruck, H. A., & Rasooly, A. (2013). Orthographic projection capillary array fluorescent sensor for mHealth. *Methods*, *63*(3), 276-281.

8.4 Technique for low-cost fluorescence detection and quantitative measurement of surface-patterned bio-assays in the presence of non-uniform excitation

A method for exciting, measuring and interpreting surface-patterned fluorescence assays on glass microscope slides was developed. This method relies on previously developed image stacking algorithms as well as a newly developed technique for local evanescent field strength estimation to accommodate varying excitation field strength. Based on this method a device was developed using consumer-grade electronic components which allowed for the measurement of a fluorescence based bioassay for the toxin SEB at a limit of detection equal to or better than that of a conventional plate reader.

8.5 Principles for modeling and optimization of wide field fluorescent imaging flow cytometers

The fundamental principles governing the performance of a wide field fluorescent imaging based flow cytometer for rare cell detection were developed and used to optimize the performance of a proof of concept model. These principles enable optimization of the physical design and operating parameters for a wide-field flow cytometer. Fundamental imaging principles were adopted from the machine vision, astronomical imaging, and fluid velocimetry communities. These methods were used to develop and refine a proof of concept flow cytometer capable of sample throughput of up to 10 mL/min, with accurate counting of rare cells at concentrations as low as 0.1 cell/mL.

9. References

1. Hay Burgess DC, Wasserman J, Dahl CA. Global health diagnostics. Nature 2006 Nov 23;444 Suppl 1:1-2.

2. Urdea M, Penny LA, Olmsted SS, Giovanni MY, Kaspar P, Shepherd A, et al. Requirements for high impact diagnostics in the developing world. Nature 2006 Nov 23;444 Suppl 1:73-9.

3. Yager P, Domingo GJ, Gerdes J. Point-of-care diagnostics for global health. Annual review of biomedical engineering 2008;10:107-44.

4. Herold KE, Rasooly A, eds. Lab on a chip technology. 2009/01/20 ed. Norfolk U.K.: Caister Academic press 2009.

5. Sun S, Ossandon M, Kostov Y, Rasooly A. Lab-on-a-chip for botulinum neurotoxin a (BoNT-A) activity analysis. Lab on a chip 2009 Nov 21;9(22):3275-81.

6. Sun S, Yang M, Kostov Y, Rasooly A. ELISA-LOC: lab-on-a-chip for enzyme-linked immunodetection. Lab on a chip 2010 Aug 21;10(16):2093-100.

7. Capitan-Vallvey LF, Asensio LJ, Lopez-Gonzalez J, Fernandez-Ramos MD, Palma AJ. Oxygen-sensing film coated photodetectors for portable instrumentation. Anal Chim Acta 2007 Jan 30;583(1):166-73.

8. Mac Sweeney MM, Bertolino C, Berney H, Sheehan M. Characterization and optimization of an optical DNA hybridization sensor for the detection of multi-drug resistant tuberculosis. Conf Proc IEEE Eng Med Biol Soc 2004;3:1960-3.

9. Claycomb RW, Delwiche MJ. Biosensor for on-line measurement of bovine progesterone during milking. Biosens Bioelectron 1998;13(11):1173-80.

10. Bruno AE, Barnard S, Rouilly M, Waldner A, Berger J, Ehrat M. All-solid-state miniaturized fluorescence sensor array for the determination of critical gases and electrolytes in blood. Anal Chem 1997 Feb 1;69(3):507-13.

11. Moehrs S, Del Guerra A, Herbert DJ, Mandelkern MA. A detector head design for small-animal PET with silicon photomultipliers (SiPM). Phys Med Biol 2006 Mar 7;51(5):1113-27.

12. Takei M, Kida T, Suzuki K. Sensitive measurement of positron emitters eluted from HPLC. Appl Radiat Isot 2001 Aug;55(2):229-34.

13. Ruiz-Martinez MC, Berka J, Belenkii A, Foret F, Miller AW, Karger BL. DNA sequencing by capillary electrophoresis with replaceable linear polyacrylamide and laser-induced fluorescence detection. Anal Chem 1993 Oct 15;65(20):2851-8.

14. Tibbe AG, de Grooth BG, Greve J, Liberti PA, Dolan GJ, Terstappen LW. Cell analysis system based on immunomagnetic cell selection and alignment followed by immunofluorescent analysis using compact disk technologies. Cytometry 2001 Jan 1;43(1):31-7.

15. Tsukagoshi K, Jinno N, Nakajima R. Development of a micro total analysis system incorporating chemiluminescence detection and application to detection of cancer markers. Anal Chem 2005 Mar 15;77(6):1684-8.

16. Roda A, Manetta AC, Portanti O, Mirasoli M, Guardigli M, Pasini P, et al. A rapid and sensitive 384-well microtitre format chemiluminescent enzyme immunoassay for 19-nortestosterone. Luminescence 2003 Mar-Apr;18(2):72-8.

17. Taitt CR, Anderson GP, Ligler FS. Evanescent wave fluorescence biosensors. Biosens Bioelectron 2005 Jun 15;20(12):2470-87.

18. Ngundi MM, Qadri SA, Wallace EV, Moore MH, Lassman ME, Shriver-Lake LC, et al. Detection of deoxynivalenol in foods and indoor air using an array biosensor. Environmental science & technology 2006 Apr 1;40(7):2352-6.

19. Moreno-Bondi MC, Taitt CR, Shriver-Lake LC, Ligler FS. Multiplexed measurement of serum antibodies using an array biosensor. Biosens Bioelectron 2006 Apr 15;21(10):1880-6.

20. Ligler FS, Sapsford KE, Golden JP, Shriver-Lake LC, Taitt CR, Dyer MA, et al. The array biosensor: portable, automated systems. Anal Sci 2007 Jan;23(1):5-10.

21. Kostov Y, Sergeev N, Wilson S, Herold KE, Rasooly A. A simple portable electroluminescence illumination-based CCD detector. Methods Mol Biol 2009;503:259-72.

22. Sapsford KE, Sun S, Francis J, Sharma S, Kostov Y, Rasooly A. A fluorescence detection platform using spatial electroluminescent excitation for measuring botulinum neurotoxin A activity. Biosens Bioelectron 2008 Dec 1;24(4):618-25.

23. Sun S, Francis J, Sapsford KE, Kostov Y, Rasooly A. Multi-wavelength Spatial LED illumination based detector for in vitro detection of Botulinum Neurotoxin A Activity. Sensors and actuators B, Chemical 2010 Apr 8;146(1-8):297-306.

24. Yang M, Kostov Y, Bruck HA, Rasooly A. Carbon nanotubes with enhanced chemiluminescence immunoassay for CCD-based detection of Staphylococcal enterotoxin B in food. Anal Chem 2008 Nov 15;80(22):8532-7.

25. Yang M, Kostov Y, Rasooly A. Carbon nanotubes based optical immunodetection of Staphylococcal Enterotoxin B (SEB) in food. Int J Food Microbiol 2008 Sep 30;127(1-2):78-83.

26. Sapsford KE, Francis J, Sun S, Kostov Y, Rasooly A. Miniaturized 96-well ELISA chips for staphylococcal enterotoxin B detection using portable colorimetric detector. Anal Bioanal Chem 2009 May;394(2):499-505.

27. Yang M, Kostov Y, Bruck HA, Rasooly A. Gold nanoparticle-based enhanced chemiluminescence immunosensor for detection of Staphylococcal Enterotoxin B (SEB) in food. Int J Food Microbiol 2009 Aug 15;133(3):265-71.

28. Coskun AF, Sencan I, Su TW, Ozcan A. Wide-field lensless fluorescent microscopy using a tapered fiber-optic faceplate on a chip. Analyst 2011 Jan 31.

29. Bishara W, Sikora U, Mudanyali O, Su TW, Yaglidere O, Luckhart S, et al. Holographic pixel super-resolution in portable lensless on-chip microscopy using a fiber-optic array. Lab Chip 2011 Apr 7;11(7):1276-9.

30. Su TW, Isikman SO, Bishara W, Tseng D, Erlinger A, Ozcan A. Multi-angle lensless digital holography for depth resolved imaging on a chip. Opt Express 2010 Apr 26;18(9):9690-711.

31. Oh C, Isikman SO, Khademhosseinieh B, Ozcan A. On-chip differential interference contrast microscopy using lensless digital holography. Opt Express 2010 Mar 1;18(5):4717-26.

32. Mudanyali O, Tseng D, Oh C, Isikman SO, Sencan I, Bishara W, et al. Compact, light-weight and cost-effective microscope based on lensless incoherent holography for telemedicine applications. Lab Chip 2010 Jun 7;10(11):1417-28.

33. Isikman SO, Sencan I, Mudanyali O, Bishara W, Oztoprak C, Ozcan A. Color and monochrome lensless on-chip imaging of Caenorhabditis elegans over a wide field-of-view. Lab Chip 2010 May 7;10(9):1109-12.

34. Coskun AF, Sencan I, Su TW, Ozcan A. Lensless wide-field fluorescent imaging on a chip using compressive decoding of sparse objects. Opt Express 2010 May 10;18(10):10510-23.

35. Mudanyali O, Erlinger A, Seo S, Su TW, Tseng D, Ozcan A. Lensless on-chip imaging of cells provides a new tool for high-throughput cell-biology and medical diagnostics. J Vis Exp 2009(34).

36. Moon S, Keles HO, Ozcan A, Khademhosseini A, Haeggstrom E, Kuritzkes D, et al. Integrating microfluidics and lensless imaging for point-of-care testing. Biosens Bioelectron 2009 Jul 15;24(11):3208-14.

37. Zhu H, Yaglidere O, Su TW, Tseng D, Ozcan A. Cost-effective and compact wide-field fluorescent imaging on a cell-phone. Lab Chip 2011 Jan 21;11(2):315-22.

38. Zhu H, Mavandadi S, Coskun AF, Yaglidere O, Ozcan A. Optofluidic Fluorescent Imaging Cytometry on a Cell Phone. Anal Chem 2011 Aug 2.

39. Breslauer DN, Maamari RN, Switz NA, Lam WA, Fletcher DA. Mobile phone based clinical microscopy for global health applications. PLoS One 2009;4(7):e6320.

40. Iqbal Z, Bjorklund RB. Colorimetric analysis of water and sand samples performed on a mobile phone. Talanta 2011 May 30;84(4):1118-23.

41. Tseng D, Mudanyali O, Oztoprak C, Isikman SO, Sencan I, Yaglidere O, et al. Lensfree microscopy on a cellphone. Lab Chip 2010 Jul 21;10(14):1787-92.

42. D. Brennan, J. Justice, B. Corbett, T. McCarthy and P. Galvin, Anal. Bioanal. Chem., 2009, 395, 621–636.

43. J.West, M. Becker, S. Tombrink and A. Manz, Anal. Chem., 2008, 80, 4403–4419.

44. M. M. Ngundi, S. A. Qadri, E. V. Wallace, M. H. Moore, M. E. Lassman, L. C. Shriver-Lake, F. S. Ligler and C. R. Taitt, Environ. Sci. Technol., 2006, 40, 2352–2356.

45. F. S. Ligler, K. E. Sapsford, J. P. Golden, L. C. Shriver-Lake, C. R. Taitt, M. A. Dyer, S. Barone and C. J. Myatt, Anal. Sci., 2007, 23, 5–10.

46. K. E. Sapsford, S. Sun, J. Francis, S. Sharma, Y. Kostov and A. Rasooly, Biosens. Bioelectron., 2008, 24, 618–625.

47. M. Yang, Y. Kostov, H. A. Bruck and A. Rasooly, Anal. Chem., 2008, 80, 8532–8537.

48. M. Yang, Y. Kostov and A. Rasooly, Int. J. Food Microbiol., 2008, 127, 78–83.

49. K. E. Sapsford, J. Francis, S. Sun, Y. Kostov and A. Rasooly, Anal. Bioanal. Chem., 2009, 394, 499–505.

50. S. Sun, M. Ossandon, Y. Kostov and A. Rasooly, Lab Chip, 2009, 9, 3275–3281.

51. M. Yang, Y. Kostov, H. A. Bruck and A. Rasooly, Int. J. Food Microbiol., 2009, 133, 265–271.

52. S. Sun, M. Yang, Y. Kostov and A. Rasooly, Lab Chip, 2010, 10, 2093–2100.

53. C. R. Taitt, G. P. Anderson and F. S. Ligler, Biosens. Bioelectron., 2005, 20, 2470–2487.

54. D. M. Vykoukal, G. P. Stone, P. R. Gascoyne, E. U. Alt and J. Vykoukal, Angew. Chem., Int. Ed., 2009, 48, 7649–7654.

55. T. W. Su, S. Seo, A. Erlinger and A. Ozcan, Biotechnol. Bioeng., 2009, 102, 856–868.

56. S. Seo, T. W. Su, D. K. Tseng, A. Erlinger and A. Ozcan, Lab Chip, 2009, 9, 777–787.

57. O. Mudanyali, A. Erlinger, S. Seo, T. W. Su, D. Tseng and A. Ozcan, J. Visualized Exp., 2009, (34), DOI: 10.3791/1650.

58. S. Moon, H. O. Keles, A. Ozcan, A. Khademhosseini, E. Haeggstrom, D. Kuritzkes and U. Demirci, Biosens. Bioelectron., 2009, 24, 3208–3214.

59. S. Moon, H. O. Keles, Y. G. Kim, D. Kuritzkes and U. Demirci, Conf. Proc. IEEE Eng. Med. Biol. Soc., 2009, 2009, 6376–6379.

60. L. M. Lee, X. Cui and C. Yang, Biomed. Microdevices, 2009, 11, 951– 958.

61. J. Wu, X. Cui, L. M. Lee and C. Yang, Opt. Express, 2008, 16, 15595– 15602.

62. X. Cui, L. M. Lee, X. Heng, W. Zhong, P. W. Sternberg, D. Psaltis and C. Yang, Proc. Natl. Acad. Sci. U. S. A., 2008, 105, 10670–10675.

63. X. Heng, D. Erickson, L. R. Baugh, Z. Yaqoob, P. W. Sternberg, D. Psaltis and C. Yang, Lab Chip, 2006, 6, 1274–1276.

64. D. Lange, C. W. Storment, C. A. Conley and G. T. A. Kovacs, Sens. Actuators, B, 2005, 107, 904–914.

65. W. Bishara, T. W. Su, A. F. Coskun and A. Ozcan, Opt. Express, 2010, 18, 11181–11191.

66. G. Stybayeva, O. Mudanyali, S. Seo, J. Silangcruz, M. Macal, E. Ramanculov, S. Dandekar, A. Erlinger, A. Ozcan and A. Revzin, Anal. Chem., 2010, 82, 3736–3744.

67. S. O. Isikman, I. Sencan, O. Mudanyali, W. Bishara, C. Oztoprak and A. Ozcan, Lab Chip, 2010, 10, 1109–1112.

68. T. W. Su, S. O. Isikman, W. Bishara, D. Tseng, A. Erlinger and A. Ozcan, Opt. Express, 2010, 18, 9690–9711.

69. B. Khademhosseinieh, I. Sencan, G. Biener, T. W. Su, A. F. Coskun, D. Tseng and A. Ozcan, Appl. Phys. Lett., 2010, 96, 171106.

70. D. Tseng, O. Mudanyali, C. Oztoprak, S. O. Isikman, I. Sencan, O. Yaglidere and A. Ozcan, Lab Chip, 2010, 10, 1787–1792.

71. O. Mudanyali, C. Oztoprak, D. Tseng, A. Erlinger and A. Ozcan, Lab Chip, 2010, 10, 2419–2423.

72. T. W. Su, A. Erlinger, D. Tseng and A. Ozcan, Anal. Chem., 2010, 82, 8307–8312.

73. A. F. Coskun, T. W. Su and A. Ozcan, Lab Chip, 2010, 10, 824–827.

74. A. F. Coskun, I. Sencan, T. W. Su and A. Ozcan, Opt. Express, 2010, 18, 10510–10523.

75. F. M. Piegsa, Nucl. Instrum. Methods Phys. Res., Sect. A, 2009, 603, 401–405.

76. G. Caglioti and F. Farfalet, Rev. Sci. Instrum., 1962, 33, 1103.

77. W. Söller, Phys. Rev., 1924, 24, 158.

78. CDC., Botulism in the United States 1899–1996: Handbook for Epidemiologists, Clinicians, and Laboratory Workers., Centers for Disease Control and Prevention, Atlanta, Ga, 1998.

79. A. Nowakowski, C. Wang, D. B. Powers, P. Amersdorfer, T. J. Smith, V. A. Montgomery, R. Sheridan, R. Blake, L. A. Smith and J. D. Marks, Proc. Natl. Acad. Sci. U. S. A., 2002, 99, 11346–11350.

80. J. E. Keller, Neuroscience, 2006, 139, 629–637.

81. C. C. Shone, C. P. Quinn, R. Wait, B. Hallis, S. G. Fooks and P. Hambleton, Eur. J. Biochem., 1993, 217, 965–971.

82. G. Schiavo, F. Benfenati, B. Poulain, O. Rossetto, P. Polverino de Laureto, B. R. DasGupta and C. Montecucco, Nature, 1992, 359, 832–835.

83. G. Schiavo, B. Poulain, O. Rossetto, F. Benfenati, L. Tauc and C. Montecucco, EMBO J., 1992, 11, 3577–3583.

84. T. C. Sudhof, P. De Camilli, H. Niemann and R. Jahn, Cell, 1993, 75, 1–4.

85. J. Blasi, E. R. Chapman, E. Link, T. Binz, S. Yamasaki, P. De Camilli, T. C. Sudhof, H. Niemann and R. Jahn, Nature, 1993, 365, 160–163.

86. G. Schiavo, O. Rossetto, S. Catsicas, P. Polverino de Laureto, B. R. DasGupta, F. Benfenati and C. Montecucco, J. Biol. Chem., 1993, 268, 23784–23787.

87. W. S. Trimble, J. Physiol., 1993, 87, 107–115.

88. J. E. Keller, J. L. Nowakowski, M. G. Filbert and M. Adler, J. Appl. Toxicol., 1999, 19(S1), S13–17.

89. M. Dong, W. H. Tepp, E. A. Johnson and E. R. Chapman, Proc. Natl. Acad. Sci. U. S. A., 2004, 101, 14701–14706.

90. S. Sun, J. Francis, K. E. Sapsford, Y. Kostov and A. Rasooly, Sens. Actuators, B, 2010, 146, 297–306.

91. Y. Kostov, N. Sergeev, S. Wilson, K. E. Herold and A. Rasooly, Methods Mol. Biol., 2009, 503, 259–272.

92. R. Rasooly, L. H. Stanker, J. M. Carter, P. M. Do, L. W. Cheng, X. He and D. L. Brandon, Int. J. Food Microbiol., 2008, 126, 135–139.

93. R. Rasooly and P. M. Do, Appl. Environ. Microbiol., 2008, 74, 4309– 4313.

94. L.F. Capitan-Vallvey, L.J. Asensio, J. Lopez-Gonzalez, M.D. Fernandez-Ramos, A.J. Palma, Oxygen-sensing film coated photodetectors for portable instrumentation, Analytica Chimica Acta 583 (2007) 166–173.

95. M.M. Mac Sweeney, C. Bertolino, H. Berney, M. Sheehan, Characterization and optimization of an optical DNA hybridization sensor for the detection of multidrug resistant tuberculosis, in: Conference Proceedings – IEEE Engineering in Medicine and Biology Society, vol. 3, 2004, pp. 1960–1963.

96. R.W. Claycomb, M.J. Delwiche, Biosensor for on-line measurement of bovine progesterone during milking, Biosensors and Bioelectronics 13 (1998) 1173–1180.

97. A.E. Bruno, S. Barnard, M. Rouilly, A. Waldner, J. Berger, M. Ehrat, All-solid-state miniaturized fluorescence sensor array for the determination of critical gases and electrolytes in blood, Analytical Chemistry 69 (1997) 507–513.

98. S. Moehrs, A. Del Guerra, D.J. Herbert, M.A. Mandelkern, A detector head design for small-animal PET with silicon photomultipliers (SiPM), Physics in Medicine & Biology 51 (2006) 1113–1127.

99. M. Takei, T. Kida, K. Suzuki, Sensitive measurement of positron emitters eluted from HPLC, Applied Radiation and Isotopes 55 (2001) 229–234.

100. M.C. Ruiz-Martinez, J. Berka, A. Belenkii, F. Foret, A.W. Miller, B.L. Karger, DNA sequencing by capillary electrophoresis with replaceable linear polyacrylamide and laser-induced fluorescence detection, Analytical Chemistry 65 (1993) 2851–2858.

101. A.G. Tibbe, B.G. de Grooth, J. Greve, P.A. Liberti, G.J. Dolan, L.W. Terstappen, Cell analysis system based on immunomagnetic cell selection and alignment followed by immunofluorescent analysis using compact disk technologies, Cytometry 43 (2001) 31–37.

102. K. Tsukagoshi, N. Jinno, R. Nakajima, Development of a micro total analysis system incorporating chemiluminescence detection and application to detection of cancer markers, Analytical Chemistry 77 (2005) 1684–1688.

103. A. Roda, A.C. Manetta, O. Portanti, M. Mirasoli, M. Guardigli, P. Pasini, R. Lelli, A rapid and sensitive 384-well microtitre format chemiluminescent enzyme immunoassay for 19-nortestosterone, Luminescence 18 (2003) 72–78.

104. F.S. Ligler, C.R. Taitt, L.C. Shriver-Lake, K.E. Sapsford, Y. Shubin, J.P. Golden, Array biosensor for detection of toxins, Analytical and Bioanalytical Chemistry 377 (2003) 469–477.

105. J. Svitel, I. Surugiu, A. Dzgoev, K. Ramanathan, B. Danielsson, Functionalized surfaces for optical biosensors: applications to in vitro pesticide residual analysis, Journal of Materials Science Materials in Medicine 12 (2001) 1075–1078.

106. Y. Liu, B. Danielsson, Rapid high throughput assay for fluorimetric detection of doxorubicin—application of nucleic acid-dye bioprobe, Analytica Chimica Acta 587 (2007) 47–51.

107. K. Burkert, T. Neumann, J. Wang, U. Jonas, W. Knoll, H. Ottleben, Automated preparation method for colloidal crystal arrays of monodisperse and binary colloid mixtures by contact printing with a pintool plotter, Langmuir 23 (2007) 3478–3484.

108. K. Tohda, M. Gratzl, Micro-miniature autonomous optical sensor array for monitoring ions and metabolites 2: color responses to pH, K+ and glucose, Analytical Sciences 22 (2006) 937–941.

109. M.J. Feldstein, J.P. Golden, C.A. Rowe, B.D. Maccraith, F.S. Ligler, Array biosensor: optical and fluidics systems, Biomedical Microdevices 1 (1999) 139–153.

110. Y.S. Sohn, A. Goodey, E.V. Anslyn, J.T. McDevitt, J.B. Shear, D.P. Neikirk, A microbead array chemical sensor using capillary-based sample introduction: toward the development of an electronic tongue, Biosensors and Bioelectronics 21 (2005) 303–312.

111. B.G. Knecht, A. Strasser, R. Dietrich, E. Martlbauer, R. Niessner, M.G. Weller, Automated microarray system for the simultaneous detection of antibiotics in milk, Analytical Chemistry 76 (2004) 646–654.

112. M.M. Ngundi, S.A. Qadri, E.V. Wallace, M.H. Moore, M.E. Lassman, L.C. Shriver- Lake, F.S. Ligler, C.R. Taitt, Detection of deoxynivalenol in foods and indoor air using an array biosensor, Environmental Science and Technology 40 (2006) 2352–2356.

113. F.S. Ligler, K.E. Sapsford, J.P. Golden, L.C. Shriver-Lake, C.R. Taitt, M.A. Dyer, S. Barone, C.J. Myatt, The array biosensor: portable, automated systems, Analytical Sciences 23 (2007) 5–10.

114. K.E. Sapsford, S. Sun, J. Francis, S. Sharma, Y. Kostov, A. Rasooly, A fluorescence detection platform using spatial electroluminescent excitation for measuring Botulinum neurotoxin A activity, Biosensors and Bioelectronics 24 (2008) 618–625.

115. M. Yang, Y. Kostov, H.A. Bruck, A. Rasooly, Carbon nanotubes with enhanced chemiluminescence immunoassay for CCD-based detection of Staphylococcal enterotoxin B in food, Analytical Chemistry 80 (2008) 8532–8537.

116. M. Yang, Y. Kostov, A. Rasooly, Carbon nanotubes based optical immunodetection of Staphylococcal enterotoxin B (SEB) in food, International Journal of Food Microbiology 127 (2008) 78–83.

117. K.E. Sapsford, J. Francis, S. Sun, Y. Kostov, A. Rasooly, Miniaturized 96-well ELISA chips for Staphylococcal enterotoxin B detection using portable colorimetric detector, Analytical and Bioanalytical Chemistry 394 (2009) 499–505.

118. S. Sun, M. Ossandon, Y. Kostov, A. Rasooly, Lab-on-a-chip for Botulinum neurotoxin A (BoNT-A) activity analysis, Lab on a Chip 9 (2009) 3275–3281.

119. M. Yang, Y. Kostov, H.A. Bruck, A. Rasooly, Gold nanoparticle-based enhanced chemiluminescence immunosensor for detection of Staphylococcal enterotoxin B (SEB) in food, International Journal of Food Microbiology 133 (2009) 265–271.

120. C.R. Taitt, G.P. Anderson, F.S. Ligler, Evanescent wave fluorescence biosensors, Biosensors and Bioelectronics 20 (2005) 2470–2487.

121. A.F. Coskun, I. Sencan, T.W. Su, A. Ozcan, Wide-field lensless fluorescent microscopy using a tapered fiber-optic faceplate on a chip, Analyst 136 (2011) 3512–3518.

122. W. Bishara, U. Sikora, O. Mudanyali, T.W. Su, O. Yaglidere, S. Luckhart, A. Ozcan, Holographic pixel super-resolution in portable lensless on-chip microscopy using a fiber-optic array, Lab on a Chip 11 (2011) 1276–1279.

123. T.W. Su, S.O. Isikman, W. Bishara, D. Tseng, A. Erlinger, A. Ozcan, Multi-angle lensless digital holography for depth resolved imaging on a chip, Optics Express 18 (2010) 9690–9711.

124. C. Oh, S.O. Isikman, B. Khademhosseinieh, A. Ozcan, On-chip differential interference contrast microscopy using lensless digital holography, Optics Express 18 (2010) 4717–4726.

125. O. Mudanyali, D. Tseng, C. Oh, S.O. Isikman, I. Sencan, W. Bishara, C. Oztoprak S. Seo, B. Khademhosseini, A. Ozcan, Compact, light-weight and cost-effective microscope based on lensless incoherent holography for telemedicine applications, Lab on a Chip 10 (2010) 1417–1428.

126. S.O. Isikman, I. Sencan, O. Mudanyali, W. Bishara, C. Oztoprak, A. Ozcan, Color and monochrome lensless on-chip imaging of Caenorhabditis elegans over a wide field-of-view, Lab on a Chip 10 (2010) 1109–1112.

127. A.F. Coskun, I. Sencan, T.W. Su, A. Ozcan, Lensless wide-field fluorescent imaging on a chip using compressive decoding of sparse objects, Optics Express 18 (2010) 10510–10523.

128. O. Mudanyali, A. Erlinger, S. Seo, T.W. Su, D. Tseng, A. Ozcan, Lensless onchip imaging of cells provides a new tool for high-throughput cell-biology and medical diagnostics, Journal of Visualized Experiments (2009).

129. S. Moon, H.O. Keles, A. Ozcan, A. Khademhosseini, E. Haeggstrom, D. Kuritzkes, U. Demirci, Integrating microfluidics and lensless imaging for point-of-care testing, Biosensors and Bioelectronics 24 (2009) 3208–3214.

130. H. Zhu, O. Yaglidere, T.W. Su, D. Tseng, A. Ozcan, Cost-effective and compact wide-field fluorescent imaging on a cell-phone, Lab on a Chip 11 (2011) 315–322.

131. H. Zhu, S. Mavandadi, A.F. Coskun, O. Yaglidere, A. Ozcan, Optofluidic fluorescent imaging cytometry on a cell phone, Analytical Chemistry (2011).

132. D.N. Breslauer, R.N. Maamari, N.A. Switz, W.A. Lam, D.A. Fletcher, Mobile phone based clinical microscopy for global health applications, PLoS One 4 (2009) e6320.

133. Z. Iqbal, R.B. Bjorklund, Colorimetric analysis of water and sand samples performed on a mobile phone, Talanta 84 (2011) 1118–1123.

134. D. Tseng, O. Mudanyali, C. Oztoprak, S.O. Isikman, I. Sencan, O. Yaglidere, A. Ozcan, Lensfree microscopy on a cellphone, Lab on a Chip 10 (2010) 1787–1792.

135. S. Sun, J. Francis, K.E. Sapsford, Y. Kostov, A. Rasooly, Multi-wavelength spatial LED illumination based detector for in vitro detection of Botulinum neurotoxin A activity, Sensors and Actuators B: Chemical 146 (2010) 297–306.

136. M. Yang, S. Sun, Y. Kostov, A. Rasooly, A simple 96 well microfluidic chip combined with visual and densitometry detection for resource-poor point of care testing, Sensors and Actuators B: Chemical 153 (1) (2011) 176–181.

137. M. Yang, S. Sun, H.A. Bruck, Y. Kostov, A. Rasooly, Lab-on-a-chip for label free biological semiconductor analysis

138. R. Istepanian, E. Jovanov, Y.T. Zhang, Introduction to the special section on MHealth: beyond seamless mobility and global wireless health-care connectivity, IEEE

Transactions on Information Technology in Biomedicine: A Publication of the IEEE Engineering in Medicine and Biology Society 8 (2004) 405–414.

139. S. Karanja, L. Mbuagbaw, P. Ritvo, J. Law, C. Kyobutungi, G. Reid, et al., A workshop report on HIV mHealth synergy and strategy meeting to review emerging evidence-based mHealth interventions and develop a framework for scale-up of these interventions, The Pan African Medical Journal 10 (2011) 37.

140. S.A. Stoner, C.S. Hendershot, A randomized trial evaluating an mHealth system to monitor and enhance adherence to pharmacotherapy for alcohol use disorders, Addiction Science & Clinical Practice 7 (2012) 9.

141. R.C. Bollinger, J. McKenzie-White, A. Gupta, Building a global health education network for clinical care and research. The benefits and challenges of distance learning tools. Lessons learned from the Hopkins Center for Clinical Global Health Education, Infectious Disease Clinics of North America 25 (2011) 385–398.

142. R. Maddison, R. Whittaker, R. Stewart, A. Kerr, Y. Jiang, G. Kira, et al., HEART: heart exercise and remote technologies: a randomized controlled trial study protocol, BMC Cardiovascular Disorders 11 (2011) 26.

143. G. Kayingo, Transforming global health with mobile technologies and social enterprises: global health and innovation conference, The Yale Journal of Biology and Medicine 85 (2012) 425–427.

144. D.C. Hay Burgess, J. Wasserman, C.A. Dahl, Global health diagnostics, Nature 444 (Suppl. 1) (2006) 1–2.

145. M. Urdea, L.A. Penny, S.S. Olmsted, M.Y. Giovanni, P. Kaspar, A. Shepherd, et al., Requirements for high impact diagnostics in the developing world, Nature 444 (Suppl. 1) (2006) 73–79.

146. P. Yager, G.J. Domingo, J. Gerdes, Point-of-care diagnostics for global health, Annual Review of Biomedical Engineering 10 (2008) 107–144.

147. O. Mudanyali, S. Dimitrov, U. Sikora, S. Padmanabhan, I. Navruz, A. Ozcan, Integrated rapid-diagnostic-test reader platform on a cellphone, Lab on a Chip 12 (2012) 2678–2686.

148. H. Zhu, U. Sikora, A. Ozcan, Quantum dot enabled detection of Escherichia coli using a cell-phone, Analyst 137 (2012) 2541–2544.

149. H. Zhu, O. Yaglidere, T.W. Su, D. Tseng, A. Ozcan, Wide-field fluorescent microscopy on a cell-phone, in: Conference Proceedings: Annual International Conference of the IEEE Engineering in Medicine and Biology Society. IEEE Engineering in Medicine and Biology Society Conference, 2011, 2011, pp. 6801–6804.

150. H. Zhu, S. Mavandadi, A.F. Coskun, O. Yaglidere, A. Ozcan, Optofluidic fluorescent imaging cytometry on a cell phone, Analytical Chemistry 83 (2011) 6641–6647.

151. D. Tseng, O. Mudanyali, C. Oztoprak, S.O. Isikman, I. Sencan, O. Yaglidere, et al., Lensfree microscopy on a cellphone, Lab on a Chip 10 (2010) 1787–1792.

152. L. Rosado, R. Castro, L. Ferreira, M. Ferreira, Extraction of ABCD rule features from skin lesions images with smartphone, Studies in Health Technology and Informatics 177 (2012) 242–247.

153. T. Wadhawan, N. Situ, H. Rui, K. Lancaster, X. Yuan, G. Zouridakis, Implementation of the 7-point checklist for melanoma detection on smart handheld devices, in: Conference Proceedings: Annual International Conference of the IEEE Engineering in Medicine and Biology Society. IEEE Engineering in Medicine and Biology Society Conference, 2011, 2011, pp. 3180–3183.

154. Z. Boyce, S. Gilmore, C. Xu, H.P. Soyer, The remote assessment of melanocytic skin lesions: a viable alternative to face-to-face consultation, Dermatology 223 (2011) 244–250.

155. R.D. Stedtfeld, D.M. Tourlousse, G. Seyrig, T.M. Stedtfeld, M. Kronlein, S. Price, et al., Gene-Z: a device for point of care genetic testing using a smartphone, Lab on a Chip 12 (2012) 1454–1462.

156. S. Wang, X. Zhao, I. Khimji, R. Akbas, W. Qiu, D. Edwards, et al., Integration of cell phone imaging with microchip ELISA to detect ovarian cancer HE4 biomarker in urine at the point-of-care, Lab on a Chip 11 (2011) 3411–3418.

157. Y. Bourquin, J. Reboud, R. Wilson, Y. Zhang, J.M. Cooper, Integrated immunoassay using tuneable surface acoustic waves and lensfree detection, Lab on a Chip 11 (2011) 2725–2730.

158. D.S. Lee, B.G. Jeon, C. Ihm, J.K. Park, M.Y. Jung, A simple and smart telemedicine device for developing regions: a pocket-sized colorimetric reader, Lab on a Chip 11 (2011) 120–126.

159. G. Zhang, C. Li, Y. Lu, H. Hu, G. Xiang, Z. Liang, et al., Validation of a mobile phone-assisted microarray decoding platform for signal-enhanced mutation detection, Biosensors and Bioelectronics 26 (2011) 4708–4714.

160. D. Lee, W.P. Chou, S.H. Yeh, P.J. Chen, P.H. Chen, DNA detection using commercial mobile phones, Biosensors and Bioelectronics 26 (2011) 4349–4354.

161. J. Balsam, H.A. Bruck, Y. Kostov, A. Rasooly, Image stacking approach to increase sensitivity of fluorescence detection using a low cost complementary metaloxide- semiconductor (CMOS) webcam, Sensors and Actuators B: Chemical 171/172 (2012) 141–147.

162. B.H. Weigl, A. Holobar, W. Trettnak, I. Klimant, H. Kraus, P. O'Leary, et al., Optical triple sensor for measuring pH, oxygen and carbon dioxide, Journal of Biotechnology 32 (1994) 127–138.

163. F.S. Ligler, M. Breimer, J.P. Golden, D.A. Nivens, J.P. Dodson, T.M. Green, et al., Integrating waveguide biosensor, Analytical Chemistry 74 (2002) 713–719. [27] R.J. Cosford, W.G. Kuhr, Capillary biosensor for glutamate, Analytical Chemistry 68 (1996) 2164–2169.

164. K. Misiakos, S.E. Kakabakos, A multi-band capillary immunosensor, Biosensors and Bioelectronics 13 (1998) 825–830.

165. M.T. Flanagan, A.N. Sloper, in: USPTO (Ed.), Waveguide Sensor with Input and Reflecting Grating and its use in Immunoassay, USPTO, U.S., 1992.

166. G.P. Anderson, K.D. King, K.L. Gaffney, L.H. Johnson, Multi-analyte interrogation using the fiber optic biosensor, Biosensors and Bioelectronics 14 (2000) 771–777.

167. R.M. Wadkins, J.P. Golden, L.M. Pritsiolas, F.S. Ligler, Detection of multiple toxic agents using a planar array immunosensor, Biosensors and Bioelectronics 13 (1998) 407–415.

168. C.A. Rowe, L.M. Tender, M.J. Feldstein, J.P. Golden, S.B. Scruggs, B.D. MacCraith, et al., Array biosensor for simultaneous identification of bacterial, viral, and protein analytes, Analytical Chemistry 71 (1999) 3846–3852.

169. T.E. Plowman, J.D. Durstchi, H.K. Wang, D.A. Christensen, J.N. Herron, W.M. Reichert, Multiple-analyte fluoroimmunoassay using an integrated optical waveguide sensor, Analytical Chemistry 71 (1999) 4344–4352.

170. J.W. Silzel, B. Cercek, C. Dodson, T. Tsay, R.J. Obremski, Mass-sensing, multianalyte microarray immunoassay with imaging detection, Clinical Chemistry 44 (1998) 2036–2043.

171. M. Yang, S. Sun, Y. Kostov, A. Rasooly, A simple 96 well microfluidic chip combined with visual and densitometry detection for resource-poor point of care testing, Sensors and Actuators B: Chemical 153 (2011) 176–181.

172. J. Balsam, M. Ossandon, Y. Kostov, H.A. Bruck, A. Rasooly, Lensless CCD-based fluorometer using a micromachined optical Söller collimator, Lab on a Chip 11 (2011) 941–949.

173. S. Sun, M. Yang, Y. Kostov, A. Rasooly, ELISA-LOC: lab-on-a-chip for enzymelinked immunodetection, Lab on a Chip 10 (2010) 2093–2100.

174. S. Sun, J. Francis, K.E. Sapsford, Y. Kostov, A. Rasooly, Multi-wavelength Spatial LED illumination based detector for in vitro detection of botulinum neurotoxin A activity, Sensors and Actuators B: Chemical 146 (2010) 297–306.

175. S. Sun, M. Ossandon, Y. Kostov, A. Rasooly, Lab-on-a-chip for botulinum neurotoxin a (BoNT-A) activity analysis, Lab on a Chip 9 (2009) 3275–3281.

176. K.E. Sapsford, J. Francis, S. Sun, Y. Kostov, A. Rasooly, Miniaturized 96-well ELISA chips for staphylococcal enterotoxin B detection using portable colorimetric detector, Analytical and Bioanalytical Chemistry 394 (2009) 499–505.

177. Y. Kostov, N. Sergeev, S. Wilson, K.E. Herold, A. Rasooly, A simple portable electroluminescence illumination-based CCD detector, Methods in Molecular Biology 503 (2009) 259–272.

178. K.E. Sapsford, S. Sun, J. Francis, S. Sharma, Y. Kostov, A. Rasooly, A fluorescence detection platform using spatial electroluminescent excitation for measuring botulinum neurotoxin A activity, Biosensors and Bioelectronics 24 (2008) 618–625.

179. D.B. Holt, A.W. Kusterbeck, F.S. Ligler, Continuous flow displacement immunosensors: a computational study, Analytical Biochemistry 287 (2000) 234–242.

180. C.R. Taitt, G.P. Anderson, F.S. Ligler, Evanescent wave fluorescence biosensors, Biosensors and Bioelectronics 20 (2005) 2470–2487.

181. C.R. Taitt, Y.S. Shubin, R. Angel, F.S. Ligler, Detection of Salmonella enterica serovar typhimurium by using a rapid, array-based immunosensor, Applied and Environmental Microbiology 70 (2004) 152–158.

182. C.R. Taitt, J.P. Golden, Y.S. Shubin, L.C. Shriver-Lake, K.E. Sapsford, A. Rasooly, et al., A portable array biosensor for detecting multiple analytes in complex samples, Microbial Ecology 47 (2004) 175–185.

183. K.E. Sapsford, Y.S. Shubin, J.B. Delehanty, J.P. Golden, C.R. Taitt, L.C. Shriver-Lake, et al., Fluorescence-based array biosensors for detection of biohazards, Journal of Applied Microbiology 96 (2004) 47–58.

184. K.E. Sapsford, A. Rasooly, C.R. Taitt, F.S. Ligler, Detection of campylobacter and Shigella species in food samples using an array biosensor, Analytical Chemistry 76 (2004) 433–440.

185. L.C. Shriver-Lake, Y.S. Shubin, F.S. Ligler, Detection of staphylococcal enterotoxin B in spiked food samples, Journal of Food Protection 66 (2003) 1851–1856.

186. F.S. Ligler, C.R. Taitt, L.C. Shriver-Lake, K.E. Sapsford, Y. Shubin, J.P. Golden, Array biosensor for detection of toxins, Analytical and Bioanalytical Chemistry 377 (2003) 469–477.

187. D.B. Holt, P.R. Gauger, A.W. Kusterbeck, F.S. Ligler, Fabrication of a capillary immunosensor in polymethyl methacrylate, Biosensors and Bioelectronics 17 (2002) 95–103.

188. K.E. Sapsford, Z. Liron, Y.S. Shubin, F.S. Ligler, Kinetics of antigen binding to arrays of antibodies in different sized spots, Analytical Chemistry 73 (2001) 5518–5524.

189. J. Balsam, M. Ossandon, H.A. Bruck, A. Rasooly, Modeling and design of micromachined optical Söller collimators for lensless CCD-based fluorometry, Analyst 137 (2012) 5011–5017.

190. Axelrod, D., Burghardt, T. P., & Thompson, N. L. (1984). Total internal reflection fluorescence. *Annual review of biophysics and bioengineering*, *13*(1), 247-268.

191. Harrick, N. J., & Loeb, G. I. (1973). Multiple internal reflection fluorescence spectrometry. *Analytical Chemistry*, *45*(4), 687-691.

192. Burghardt, T. P., & Axelrod, D. (1981). Total internal reflection/fluorescence photobleaching recovery study of serum albumin adsorption dynamics.*Biophysical journal*, *33*(3), 455-467.

193. Jennings, T. L., Becker-Catania, S. G., Triulzi, R. C., Tao, G., Scott, B., Sapsford, K. E., Spindel, S., … & Medintz, I. L. (2011). Reactive semiconductor nanocrystals for chemoselective biolabeling and multiplexed analysis. *ACS nano*, *5*(7), 5579-5593.

194. Sapsford, K. E., Spindel, S., Jennings, T., Tao, G., Triulzi, R. C., Algar, W. R., & Medintz, I. L. (2011). Optimizing two-color semiconductor nanocrystal immunoassays in single well microtiter plate formats. *Sensors*, *11*(8), 7879-7891.

195. Spindel, S., Balsam, J., Sapsford, K.E. *Unpublished Data*

196. Pantel, K., & Alix-Panabières, C. (2010). Circulating tumour cells in cancer patients: challenges and perspectives. *Trends in molecular medicine*, *16*(9), 398-406.

197. Jemal, A., Bray, F., Center, M. M., Ferlay, J., Ward, E., & Forman, D. (2011). Global cancer statistics. CA: a cancer journal for clinicians, 61(2), 69-90.

198. Steeg, P. S. (2006). Tumor metastasis: mechanistic insights and clinical challenges. *Nature medicine*, *12*(8), 895-904.

199. Fidler, I. J. (2003). The pathogenesis of cancer metastasis: the 'seed and soil' hypothesis revisited. *Nature Reviews Cancer*, *3*(6), 453-458.

200. Kamentsky, L. A., Melamed, M. R., & Derman, H. (1965). Spectrophotometer: new instrument for ultrarapid cell analysis. *Science*, *150*(3696), 630-631.

201. Shapiro, H. M. (2005). *Practical flow cytometry*. John Wiley & Sons.

202. Wittrup, K. D., Westerman, R. J., & Desai, R. (1994). Fluorescence array detector for large-field quantitative fluorescence cytometry. *Cytometry*, *16*(3), 206-213.

203. Varga, V. S., Bocsi, J., Sipos, F., Csendes, G., Tulassay, Z., & Molnár, B. (2004). Scanning fluorescent microscopy is an alternative for quantitative fluorescent cell analysis. *Cytometry Part A*, *60*(1), 53-62.

204. Shapiro, H. M., & Perlmutter, N. G. (2006). Personal cytometers: slow flow or no flow?. *Cytometry part A*, *69*(7), 620-630.

205. Zhu, H., Mavandadi, S., Coskun, A. F., Yaglidere, O., & Ozcan, A. (2011). Optofluidic fluorescent imaging cytometry on a cell phone. *Analytical chemistry*,*83*(17), 6641-6647.

206. Zhu, H., Sencan, I., Wong, J., Dimitrov, S., Tseng, D., Nagashima, K., & Ozcan, A. (2013). Cost-effective and rapid blood analysis on a cell-phone. *Lab on a Chip*, *13*(7), 1282-1288.

207. Shapiro, H. M. (2004). "Cellular astronomy"—A foreseeable future in cytometry.*Cytometry Part A*, *60*(2), 115-124.

208. Zhu, H., Mavandadi, S., Coskun, A. F., Yaglidere, O., & Ozcan, A. (2011). Optofluidic fluorescent imaging cytometry on a cell phone. *Analytical chemistry*,*83*(17), 6641-6647.

209. Zhu, H., Sencan, I., Wong, J., Dimitrov, S., Tseng, D., Nagashima, K., & Ozcan, A. (2013). Cost-effective and rapid blood analysis on a cell-phone. *Lab on a Chip*, *13*(7), 1282-1288.

210. Beck, N. (2009). *Diagnostic Hematology*. Springer.

211. Adrian, R. J., & Westerweel, J. (2010). *Particle image velocimetry* (Vol. 30). Cambridge University Press.

212. Nagrath, S., Sequist, L. V., Maheswaran, S., Bell, D. W., Irimia, D., Ulkus, L., ... & Toner, M. (2007). Isolation of rare circulating tumour cells in cancer patients by microchip technology. Nature, 450(7173), 1235-1239.

213. Stott, S. L., Hsu, C. H., Tsukrov, D. I., Yu, M., Miyamoto, D. T., Waltman, B. A., ... & Toner, M. (2010). Isolation of circulating tumor cells using a microvortex-generating herringbone-chip. Proceedings of the National Academy of Sciences, 107(43), 18392-18397.

214. Cristofanilli, M., Budd, G. T., Ellis, M. J., Stopeck, A., Matera, J., Miller, M. C., ... & Hayes, D. F. (2004). Circulating tumor cells, disease progression, and survival in metastatic breast cancer. *New England Journal of Medicine*, *351*(8), 781-791.

215. Janesick, J. R., Klaasen, K. P., & Elliott, T. (1987). Charge-coupled-device charge-collection efficiency and the photon-transfer technique. *Optical engineering*, *26*(10), 260972-260972.